

QC852
.C6
no. 422
ATSL

LIBRARIES
FEB 29 1988
COLORADO STATE UNIVERSITY

Observational Analysis of Cumulus and Stratocumulus Entrainment Using Ozone

by

Clark Jay Weaver
Richard Pearson, Jr.



Atmospheric Science

PAPER NO.
422

**DEPARTMENT OF ATMOSPHERIC SCIENCE
COLORADO STATE UNIVERSITY
FORT COLLINS, COLORADO**

OBSERVATIONAL ANALYSIS OF CUMULUS AND STRATOCUMULUS
ENTRAINMENT USING OZONE

by
Clark Jay Weaver

Richard Pearson, Jr.
Principal Investigator

Research supported by the
National Science Foundation
under Grants ATM-8114575,
ATM-8312615, ATM-8311405,
and ATM-8614956.

Department of Atmospheric Science
Colorado State University
Fort Collins, Colorado

October 1987

Atmospheric Science Paper No. 422

PC852
- C6
no. 422
ATSL

ABSTRACT

This study demonstrates that ozone mixing ratio (O_3) is conserved during moist convection and can be used as a tracer for cloud entrainment studies. The approach in Part I is to apply mixing line analysis to pairs of θ_e , θ_l , total water mixing ratio and O_3 derived from aircraft penetrations of growing cumulus congestus. Conclusions about entrainment from the mixing diagrams employing O_3 agree with those using thermodynamic quantities. Any disagreement uncovered deficiencies in the water substance measurement technique. Ozone is conserved and recommended for future entrainment studies. Other conclusions were that strong updrafts, thought to be a diluted adiabatic core, entrained laterally from the environment at the observation level. In contrast, the downshear region of the cloud entrained air from above the observation level as well as laterally.

Entrainment instability is thought to be a cause of stratocumulus break up. At the cloud-overlying air interface, mixtures may form which are negatively buoyant due to cloud droplet evaporation. In Part II, quantities devised to predict breakup, Δ_2 , X and Δ_m , are obtained from aircraft observations and are tested against cloud observations from satellite. Often, the parameters indicate that breakup should occur but the clouds remain, sometimes for several days. One possible explanation for break up is vertical motion from passing synoptic cyclones. Several cases suggest that break up is associated with the downward vertical motion from the cold air advection behind a eastward moving cyclone.

ACKNOWLEDGEMENTS

I wish to thank my adviser Dr. Richard Pearson Jr. for guidance and support during this work and throughout my tenure as a graduate student. Many thanks also go to the other members of my advisory committee, Dr. Donald Lenschow and Professors Wayne Schubert, Richard Johnson and Anthony Rappe, for their careful review of this research.

This material is based upon work supported by the National Science Foundation under Grants No. ATM-8114575, ATM-8312615, ATM-8311405 and ATM-8614956. Aircraft time and computer support were provided, respectively, by the Research Aviation Facility and the Scientific Computing Division of the National Center for Atmospheric Research. The National Center for Atmospheric Research is sponsored by the National Science Foundation.

Table of Contents

I OZONE AS A TRACER FOR CUMULUS CLOUD ENTRAINMENT STUDIES	1
1 INTRODUCTION	2
1.1 Theory	3
1.2 Equipment	6
2 RESULTS	8
2.1 Case 1	9
2.2 Case 2	13
2.3 Case 3	15
2.4 Case 4	15
3 DISCUSSION	36
3.1 Mixing Line Analysis	36
3.2 In-cloud Points Subject to Icing	37
3.3.1 Mathematical Dependence of θ_e and Q on q	39
3.3.2 Limitations on Moisture Measurements	41
3.4 Ozone as a Conserved Quantity	41
REFERENCES	47
II ENTRAINMENT INSTABILITY AND VERTICAL MOTION AS CAUSES OF STRATOCUMULUS BREAK UP	50
1 INTRODUCTION	51
1.1 Problem	51
1.2 Objective	51
2 BACKGROUND	52
2.1 Physics of Entrainment Instability	52
2.2 Definition of Stratocumulus Stability Parameters	53

2.3	Evaluation of Parameters from Real Data	55
3	EVALUATION OF ENTRAINMENT INSTABILITY	60
3.1	Description of DYCOMS	60
3.2	Determination of Cloud Thermodynamic Stability	60
3.2.1	Soundings	61
3.2.2	Horizontal Legs	64
3.3	Comparison of Δ_2 with Photographs	65
3.4	Evaluation of Parameters	68
4	VERTICAL MOTION	86
4.1	Background	86
4.2	Observations	86
4.2.1	Description of Data	86
4.2.2	Case 1	87
4.2.3	Case 2	88
4.2.4	Case 3	89
4.3	Discussion	89
	REFERENCES	110
	APPENDIX	112

Part I

OZONE AS A TRACER FOR CUMULUS
CLOUD ENTRAINMENT STUDIES

Chapter 1: INTRODUCTION

Entrainment plays an important role in the cloud life cycle and for this reason it has been the subject of numerous experimental studies (see for example, LaMontagne and Telford, 1983; Boatman and Auer, 1983 and Paluch, 1979). Because clouds are composed partially of boundary layer air, this mixing facilitates the exchange of boundary layer air with the air aloft. To study this process, clouds are sampled *in situ* with the intent of determining an observed parcel's history in the subsequent data analysis. Conserved quantities derived from the collected data are useful here because the value for a parcel will not change with altitude. Also, the analysis is simplified if the conserved quantities mix linearly.

Previous cloud entrainment studies have used various thermodynamic conserved quantities derived from moisture and temperature variables. Examples of quantities conserving entropy are pseudo-equivalent potential temperature (θ_e) (Bolton, 1980), wet equivalent potential temperature (θ_q) (Paluch, 1979) and liquid water potential temperature (θ_l) (Betts, 1982). For moisture conservation total water mixing ratio (Q) is used. The temperature and pressure of a parcel's saturation point can also be used (Betts, 1982).

Although all of these quantities closely fit the requirements for a conserved quantity, they must be used with caution. In-cloud thermodynamic properties are difficult to measure. Temperature measurements are needed for θ and are sometime used for Q , but the sensors used are subject to errors from both icing and wetting. Under ideal conditions, the widely used Johnson-Williams (JW) hot-wire liquid water probe can have errors of up to 20% (Baumgardner, 1983) but it may record negative values under icing conditions. Finally, Q is not conserved

during precipitation and θ is not conserved due to radiation. Because of these problems it would be helpful to measure a third, independent conserved quantity.

This study investigates the possibility of using ozone mixing ratio (O_3) as an additional conserved quantity for studies in entrainment. The remainder of this chapter discusses the theoretical reasons why ozone ought to be conserved during moist convection. Chapter 2 presents observations of four growing cumulus congestus sampled by aircraft in rural Montana. The goal is to see if O_3 behaved similarly to the conserved thermodynamic quantities; if this can be demonstrated, it provides evidence that O_3 is also conserved. The final chapter shows the drawbacks of using only thermodynamic quantities in the mixing line analysis as well as a discussion of whether the clouds were entraining laterally or from the cloud top.

1.1 Theory

The use of ozone as a tracer is possible because it generally has a gradient with height. For this study in a relatively clean rural environment the gradient is positive. This gradient occurs because ozone is transported from the stratosphere to the tropopause in the vicinity of a jet maximum; thereafter the ozone is diluted to smaller tropospheric values (Danielsen and Mohnen 1977). At the surface ozone is destroyed. Usually the mixing is slow but the presence of clouds enhances this process. We are able to observe this mixing because the time scale for local ozone production/destruction in clean air is slow compared with the typical cumulus cloud lifetime of 15 to 30 minutes. For the cumulus clouds of this study, the potential causes for local change in ozone concentration are: 1) Cloud droplets acting as an ozone sink either simply by solution of ozone and/or chemical destruction within the droplet and 2) In-situ photochemical production or destruction.

Cloud droplets should be a negligible sink for ozone considering its solubility in liquid water and its chemical destruction rate in the aqueous phase. The solubility obeys Henry's law which means that it is proportional to partial pressure at low concentrations. The constant used is $1.5 \times 10^{-2} \text{ M atm}^{-1}$ (M is molarity, moles per liter of solvent) taken from Rawson (1953) and results in 1.5×10^{-10} moles of ozone dissolved in 10 g of water at a partial pressure of 10^{-7} atm (100 ppbv). Large cumulus congestus can have up to 10 g of liquid water per m^3 and O_3 concentrations of 4.5×10^{-12} moles cm^{-3} . Thus, 3×10^{-4} percent of the ozone will be dissolved.

Once in aqueous phase, reactions can rapidly destroy ozone. Wesely et al. (1981) observe surface resistances over lake water which are 50 times larger than a resistance calculated only considering dissolving and diffusing un-ionized ozone through a laminar film of water. The difference is attributed to surface chemical reactions. Garland et al. (1980) report deposition velocities to seawater which are 10-30 times greater than those calculated without considering chemical reactions. Ozone destruction by iodine accounts for a fraction of the difference and reactions with surfactant organic matter is thought to account for the remainder. Perhaps these organic surfactants also explain the discrepancy with lake water. Although one cannot say whether the unknown organic surfactants exist on the cloud droplet, the droplets will not have the as high a concentration of iodine as found in seawater.

A more conclusive approach is to consider simulations of the free radical chemistries of the gas and aqueous phase within a cloud not influenced by anthropogenic emissions (Chameides and Davis, 1982). They consider a number of reactions leading to ozone destruction. The fastest is oxidation of S_{IV} (in the form of SO_2) by ozone and is represented by the overall equation



Maahs (1983) determined the rate constant for this second order reaction and found it to be a function of pH as well as temperature. Let us use a pH of 5.1 and an SO_2 concentration of 7×10^{-11} M, which are both from the model, and assume that aqueous ozone remains in thermodynamic equilibrium with the gas phase (i.e. the time scale for phase equilibrium is much faster than for chemical equilibrium, so the ozone destroyed is immediately replenished from the gas phase). This yields a destruction rate of $260 \% \text{ hr}^{-1}$ inside the drop and a destruction time scale of about 23 min. Also considered is destruction by O_2^- ; this is also second order and has destruction rate of $180 \% \text{ hr}^{-1}$. Other sinks include photolysis and reactions with OH^- and H_2O_2 but these appear to be a magnitude slower. Using a chemical destruction rate of $500 \% \text{ hr}^{-1}$ in the drop and the $3 \times 10^{-4} \%$ solubility value from above, about $2 \times 10^{-3} \%$ of the gas phase ozone will be destroyed per hour. Therefore, the reactions will rapidly destroy ozone but the low solubility prohibits this from influencing gaseous phase concentrations.

The rate of local ozone production for rural Montana is probably negligible over one hour. Observations from nearby eastern Colorado are $2.6 \text{ ng m}^{-3} \text{ s}^{-1}$ (5.4 ppbv hr^{-1}) for photochemical production rates over short grass prairie (Lenschow et al., 1981 and Pearson et al. 1982). However, both studies were conducted at sites downwind of polluted areas where advection of ozone precursors was probable. Perhaps it is more suitable to consider the production rate of $1.4 \text{ ng m}^{-3} \text{ s}^{-1}$ (3.0 ppbv hr^{-1}) reported by Kawa (1986) from the Big Thicket National Preserve. This low rate is probably due to the lack of ozone precursors from nearby Houston. For this value the change in ozone mixing ratio would be negligible over the lifetime of the cumulus cloud. Presence of anthropogenic ozone precursors in a nonpristine boundary layer may cause a negative vertical profile. Greenhut (1986) and Kawa (1986) both report a number of cases near urban areas where the boundary layer ozone is the same or greater than the air aloft. This

negative gradient will not preclude using ozone as a tracer unless the photochemical production causing the gradient is too high or the air mass is too inhomogeneous chemically.

1.2 Equipment

We tested the hypothesis that smaller cumuli could transport ozone passively by penetrating non-precipitating cumulus congestus with an instrumented research aircraft from the Research Aviation Facility of the National Center for Atmospheric Research. A description of the instrumentation on board the research platform, a Beechcraft Queen Air, follows. Cloud liquid water was measured by a JW sensor with a 1 Hz bandwidth. These data were analyzed with caution because baselining (the baseline value is measured in the absence of liquid water) the data to zero was often necessary. This is due to icing of the instrument at higher altitudes and because the baseline value shifts with a change in aircraft altitude. The King probe is more accurate, especially for greater liquid water contents but was not available for this experiment. Temperature was measured by a reverse flow thermometer (Rodi and Spyers-Duran, 1972). Heymsfield et al. (1978) have shown that this type of device minimizes errors due to wetting of the probe so that temperatures should be accurate during brief times in-cloud. However, Lawson (1987) demonstrates that for conditions where the ambient temperature is warmer than 0°C cloud liquid water reaches the platinum resistance element and may underestimate the temperature. Since only the lowest penetration levels are above 0°C, this is not expected to be a major problem. The response time for this sensor is also slow (1 Hz bandwidth). In clear air, humidity was measured with a cooled mirror dew point hygrometer (slower than 1 Hz bandwidth). Dew point measurements were unsatisfactory in cloud due to rapid maneuvers and the presence of supercooled water, so saturation was assumed. The faster response Lyman- α hygrometer could have been used out of cloud but the presence of

cloud droplets in cloud scatters the light from the sensing path and moisture is overestimated. Air motion, radiometric surface temperature (Barnes PRT-5), position (inertial navigation) and static pressure were also measured.

The O_3 sensor has been described by Pearson and Stedman (1980), and measures chemiluminescence from the reaction of O_3 with NO. A systematic correction for quenching by water vapor is made to the data (Matthews et al., 1977; Lenschow et al., 1981). Because this instrument has a bandwidth of 11 Hz, it can be used to detect inhomogeneities on the order of 10 m in the clouds sampled. Shot noise adds a random variance proportional to the mean O_3 level. To reduce this noise, and to make the bandwidth comparable to the cloud liquid water measurements, the turbulent rate data were filtered to a bandwidth of 0.5 Hz at 50 ppbv. The shot noise contributed a standard deviation of 0.3 ppbv to the measurement.

Chapter 2: RESULTS

A total of nine clouds were observed during June 1981 in SE Montana (106° W, 46° N) during the Cooperative Convective Precipitation Experiment. Four of these cases are described below. Cases 1 to 3 (June 20) are of interest because the highest liquid water contents and cloud depths were observed. Case 4 (June 18) with lower liquid water content is representative of the remaining cases.

Environmental conditions of June 20 are shown in Figure 1.1 by two aircraft soundings sampled en route to the research area. Shown with O_3 are thermodynamic quantities θ_1 and Q . The later two are chosen because they are conserved for adiabatic processes and facilitate the analysis. The lower sounding (up to 1900 m) includes the mixed layer and is labeled F. Although variability exists in the mixed layer, especially in Q , it is probably due to horizontal inhomogeneities encountered by the aircraft. The upper portion of the sounding is divided into five other layers labeled A-E. Here the positive vertical gradient of O_3 is consistent with transport from the stratosphere coupled with surface destruction. Portions of the profile are convectively unstable where there is a rapid decrease in moisture with height, e.g. at 2300 m. The upward vertical motion caused by the upper air divergence from the jet stream maximum region near the research area may provide the dynamics to release this instability. The convection was also driven at the surface by heating (temperatures by 1100 MDT were 18-24 °C) and high moisture contents (dew points were 11 - 15 °C).

Mixing line analysis, described in Figure 1.2, is a helpful tool for investigating cloud-environment mixing. In this study the two independent conserved quantities are derived from in-cloud and environmental data. Figure 1.3 shows (θ_1, O_3) ,

(θ_l, Q) and (Q, O_3) mixing diagrams for the environmental profiles from Figure 1.1. To reduce confusion only a sample of the points from each of the five layers is shown. Those points causing the numbered labels to overlap are omitted. For Figure 1.3b, the additional data points shown are taken from the portion of the 1310 MDT Colestrip MT sounding above 4300 m. These points are influenced by lower stratospheric air, characterized by increasing θ_l values and decreasing Q values with height. Although ozone measurements above 4300 m are not available, climatological midlatitude summer ozone mixing ratios typically increase between 4300 m and the tropopause (McClatchey et al., 1972). Thus, the climatological points, not shown, would lie farther toward the upper right hand corner of Figure 1.3a and 1.3c with increasing height and would behave in a manner consistent with the Colestrip data shown in Figure 1.3b.

2.1 Case 1

The aircraft made four level penetrations of a growing cumulus cloud and the sub-cloud air between 1241 and 1257 MDT 20 June. Figure 1.4 is a time series of O_3 , θ_l , Q , cloud liquid water l , and vertical velocity perturbation w' from the highest penetration at 4300 m. Here the cloud temperature was -7°C as measured by the reverse flow thermometer. All five variables change abruptly at the upshear (growing) edge of the cloud, encountered at 1241.2 MDT. The downshear (dissipating) edge is not as clearly defined as the upshear edge, but all variables gradually return to their environmental values. In this region the unfiltered raw data (not shown) have inhomogeneities in the cloud indicated by the fluctuations in O_3 and w' on the order of several seconds (about 200 m). In addition, the plane encountered unsaturated regions inside the cloud which complicate measurements of moisture. These inhomogeneities in the downshear regions are due to mixing between the adiabatic core and the environment. Also note that the updraft region often corresponds to low ozone mixing ratios characteristic of cloud base air while downdraft air is closer to environmental values. Inhomogeneities inside the

cloud and the abrupt transitions at the upshear boundary were observed to some degree in all the clouds sampled.

These brief encounters of unsaturated air inside the cloud demonstrate the need to determine when to use the saturation assumption in the calculation of Q and θ_e . The value of l is used as a criterion even though it was subject to the baselining procedure. Throughout this study, in-cloud data points have measurable liquid water and saturation is assumed at a slightly higher liquid water threshold. For Cases 1 and 2 sampled on 20 June, any point with liquid water greater than 0.10 g m^{-3} was classified as in-cloud and the saturation threshold was 0.30 g m^{-3} . For the smaller clouds of Cases 3 and 4, the in-cloud criteria was 0.05 g m^{-3} and the saturation threshold was 0.15 g m^{-3} .

Figure 1.5 shows mixing line diagrams using cloud and environmental data. Each data point is a 1 s average of the quantity shown. The in-cloud data are labeled by numbers according to the penetration level. All in-cloud data are used; however, overlapping labels are not shown to reduce clutter. The enclosed areas show the ranges of the environmental air sampled just moments before or after the cloud was encountered at the two highest penetrations.

The purpose of these plots is to test if ozone behaves like a conserved quantity by comparing it with accepted thermodynamic tracers θ_l and Q . The method of evaluation is to see if the mixing diagrams employing ozone (θ_l, O_3) and (Q, O_3) yield the same conclusions as the (θ_l, Q) diagram. However, the accepted conserved quantities θ_l and Q , have potential errors in measurement making analysis difficult. When there is a disagreement between two mixing diagrams it is easy to attribute the problem to uncertainties in θ_l and Q , thus increasing the difficulty of testing the hypothesis for ozone conservation. The approach then will be to analyze the diagrams and explain any disagreement.

Let us analyze the first three diagrams of Figure 1.5 (Figure 1.5d is discussed later) starting at the lowest level. The in-cloud points from the lowest penetration level (2452 m labeled by 4's) are important for the evaluation of cloud base values

used throughout the mixing line analysis. A high concentration of points from this level are found at the two circled 4's. They are very similar to the values measured in the sub-cloud region and occur simultaneously with the strongest updraft of this level ($+3 \text{ m s}^{-1}$). Measurements of sub-cloud air could be used for cloud base values but as can be seen from the points labeled 1 in Figure 1.3 they are highly variable. Using such large ranges for cloud base values would lead to ambiguous conclusions for the mixing line analysis. Therefore, here and for the other cases, the adiabatic core from the lowest penetration level will be used as cloud base.

Most of the other 4's are from the downshear region of the cloud where unsaturated pockets are encountered. This creates problems for the dew point hygrometer because the cloud droplets on the cooled mirror take time to evaporate and the instrument cannot quickly adjust to dry conditions. For these points, Q is probably overestimated. This explains why on diagrams using Q these points have more moisture than the cloud base value and at the same time are unsaturated. The (θ_1, O_3) diagram is not affected by this problem and the points have a component of environmental air as expected.

The next level (3070 m labeled by 3's) shows a variety of points either characterized by cloud base air, the environment or a mixture of the two. The circled 3's with $O_3 = 40 \text{ ppbv}$ coincide with the strongest observed updrafts of this penetration ($+7 \text{ m s}^{-1}$). This is probably air from the adiabatic core observed at the circled 4's which has experienced negligible entrainment. Now let us consider the circled 3 with $O_3 = 44 \text{ ppbv}$ where there is a high concentration of points from this level. A 4:1 mixture of cloud base air and environmental from point C (3100-3440 m) of the sounding (Figure 1.3) can account for this in-cloud air. However, those diagrams employing θ_1 have the cloud point to the right of the line connecting cloud base to point C meaning that air at point B or A must also be part of the mixture. Thus, the mixing is not completely lateral as entrainment of environmental air above the cloud point is observed. It is harder to reach this

conclusion from the (Q, O_3) diagram because all points from the sounding fall along a line. Finally there are the 3's with $O_3 > 52$ ppbv which are from the downshear region of the cloud. Again Q is probably overestimated so the (θ_l, O_3) diagram is the one to consider. There is a series of points from the center of the cloud points, e.g. the circled 3 $O_3 = 44$ ppbv, leading to point C. This series of points bends toward point B which indicates that there may also be entrainment from this higher level.

The next higher penetration level (3670 m labeled by 2's) has the same mixing scenario as the one at 3070 m. Again the adiabatic core was sampled, although only for about 1 second, as evidenced by the 2 close to the cloud base. Here the updraft was almost $+10 \text{ m s}^{-1}$. The high concentration of cloud points from this penetration at the circled 2 at $O_3 = 46$ ppbv appears to be a 1:1 mixture of cloud base and environmental air between points B and C (Figure 1.3) according to all three diagrams. In the downshear region the (θ_l, O_3) diagram shows another series of points from the center of the cloud points, e.g. the circled 2, to the environment at this level (enclosed area labeled 2). Again this series of points bends toward environmental air from a higher level (enclosed region labeled 1), indicating that some 2's are not mixing solely with the environmental at this level, but may also have a component from the environment at a higher level.

The uppermost penetration (4300 m labeled by 1's) demonstrates why it is particularly useful to have O_3 as a tracer. Consider the line connecting the environmental air measured just prior to the penetration (the enclosed area labeled 1) with the cloud base. The two diagrams using O_3 have most of the cloud points along this line but there are a significant number to the right of the line. This may indicate mixing with environmental air above this penetration level; however, this cannot be confirmed from these two diagrams alone because the O_3 values above 4300 m are unavailable. The (θ_l, Q) diagram does not yield much information. Although data points above 4300 m are shown, the cloud points, the environmental air at 4300 m, at 5040 m and at 6090 m are colinear. This arises from the strong

anticorrelation between O_3 and Q found in the sounding, and makes it difficult to tell the origin of the entrained air.

It is more likely that the origin of entrained air is at 4300 m and not above this level. Those cloud points closest to the lower right hand corner of the diagrams employing O_3 (labeled X) are from the strongest updraft region observed at this level ($+7 \text{ m s}^{-1}$). Although it is remotely possible that the air from the updraft region may have been far above the 4300 m level at some earlier instance, all other maximum updraft regions observed during this case have been adiabatic cores largely composed of cloud base air. I suspect instead that the liquid water probe experienced icing during this penetration at $-7.5 \text{ }^\circ\text{C}$ and sometimes underestimated l . A 1 g kg^{-1} error in l would decrease θ_l by $2.5 \text{ }^\circ\text{C}$ and increase Q by 1 g kg^{-1} . This would move the point (at the tip of the arrow) labeled X to X'. All three diagrams would then show lateral entrainment and the updraft region would be more consistent with its character at lower altitudes. Notice that for the (θ_l, Q) diagram a change in liquid water content affects both quantities because both θ_l and Q are dependent on l . Further evidence that l was underestimated is seen in the (θ_e, O_3) diagram because neither θ_e or O_3 are functions of l . Here the circled 1's in question are found to the left of their location on the (θ_l, O_3) diagram. The θ_e diagram shows them to be more characteristic of the adiabatic core and to have mixed with environmental air between the highest two penetration levels. Fortunately, the lower penetrations are immune from this problem because the cloud temperature is warm enough to prevent icing. The discussion treats the icing problem in more detail.

2.2 Case 2

This case, sampled between 1201 and 1214 MDT consists of three level penetrations and sub-cloud measurements. Estimated cloud top at the start of the penetration (5000 m), updraft velocities and liquid water contents were all similar to those of Case 1. Figure 1.6 shows mixing line diagrams using cloud

and environmental data. Only selected in-cloud points are shown and are labeled by numbers according to a particular region of the cloud. There is no set criteria distinguishing a given region of the cloud, although they can sometimes be described qualitatively by vertical motion. The other features are analogous to Figure 1.5.

The two groups of in-cloud points observed at 3070 m (labeled by 5's and 6's) are from two different updraft regions. The 6's are within the ranges of the cloud base values sampled below the cloud and the circled one will be taken as the cloud base value. According to all three diagrams the weaker updraft (5's) appears to be a 2:3 mixture of the environment sampled at the same level and cloud base. There is no evidence that this updraft has mixed with air above the observation level.

The 3660 m penetration level shows a downshear region (labeled by 3's) and an updraft (4's). The later seems to have a higher fraction of cloud base air and mixes with point C air at 3100 - 3400 m. The downshear region, on the other hand, is more diluted and apparently contains air from a higher level (point B, 3600 - 3800 m) or the environment at this penetration level (the enclosed area labeled 2).

At the highest penetration level (4320 m) a moderate updraft (labeled by 1's) and a strong downdraft region (labeled by 2's) are shown. All diagrams show the downdraft to be a 2:3 mixture of cloud base air and environmental air sampled just before the penetration at 4300m (the enclosed area labeled 1). I suspect that, as in Case 1, the liquid water probe experienced icing during the updraft region (1's). A 2 g kg^{-1} underestimation of l would move the center for the 1's labeled X to X'. Furthermore the θ_e values for the 1's are within 1.5 K of those at cloud base. All of this suggests that a slightly diluted adiabatic core was sampled.

2.3 Case 3

This cloud, sampled between 1314 and 1327 MDT on June 20 was not as deep as the previous two cases. The highest cloud penetration level was only 3540 m and cloud liquid water contents were never greater than 0.7 g kg^{-1} . Figure 1.7 shows all the in-cloud data for each penetration level (overlapping points are not shown) along with the environmental air sampled just prior to and after each penetration. The cloud base point is difficult to determine but it is believed to lie within the area CB. This is the range of points sampled below cloud base at 2000 m. All three mixing diagrams show that the cloud points have entrained air sampled at 4000 m (enclosed area labeled 0) but it is not known if this environmental air is above or below cloud top. The entrainment appears to be lateral, though not entirely so. The diagrams employing Q show a component from above the observation level. Because this cloud was not as deep as the first two cases, the temperatures were probably warm enough to prevent icing episodes and all in-cloud points can be analyzed without a correction.

2.4 Case 4

Clouds observed on June 11 had less vigorous updrafts and lower liquid water contents compared to clouds sampled on June 20. Case 4, sampled between 1510 and 1530 MDT, is shown in Figure 1.8. It is the most interesting cloud from this day because the liquid water sensor experienced icing during most of the entire top penetration level at 4000 m. There were five other cloud penetrations at lower levels. The mixing scenarios for all diagrams were the same indicating that O_3 behaved like θ_l and Q . Only the area outlining the points from the lowest penetration level, believed to best represent cloud base, is shown so as to concentrate on the highest one. The aircraft first encountered an updraft region (labeled by 1's) followed by a downshear region composed of weaker vertical motion (labeled by 2's). All three diagrams indicate that the downshear region

is a mixture of cloud base and the environmental air sampled at this penetration level (enclosed area labeled 2). The points from the updraft region, on the other hand are subject to icing episodes. Assuming l was underestimated, by 1 g kg^{-1} , will shift point X to X'. Then the 1's will fall within the triangle formed by the cloud base, and the two areas of environmental air (labeled by 1 and 2) at the penetration level. Without this correction the 1's are difficult to analyze except on the (θ_e, O_3) diagram.

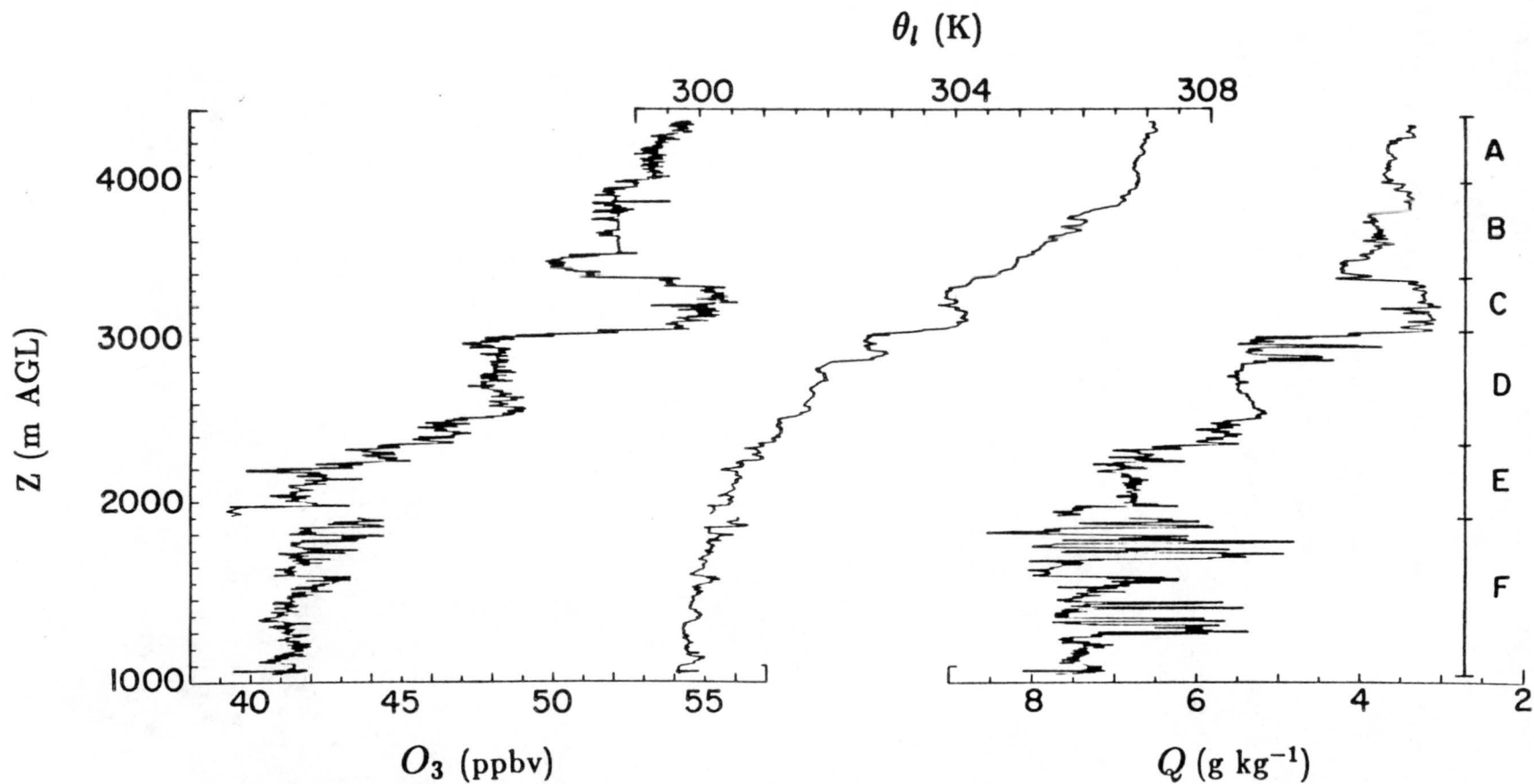


Figure 1.1. Vertical profiles of O_3 , θ_l and Q from two different soundings in clear air on 20 June. The portion below 1900 m is just after take-off from Miles City and approximately 1 hr prior to the first cloud penetration (Case 2). For later reference it is labeled layer F. The upper portion is 20 min prior to this penetration and is divided into five layers (labeled A-E). Note the orientation of the Q -axis which is consistent with subsequent figures.

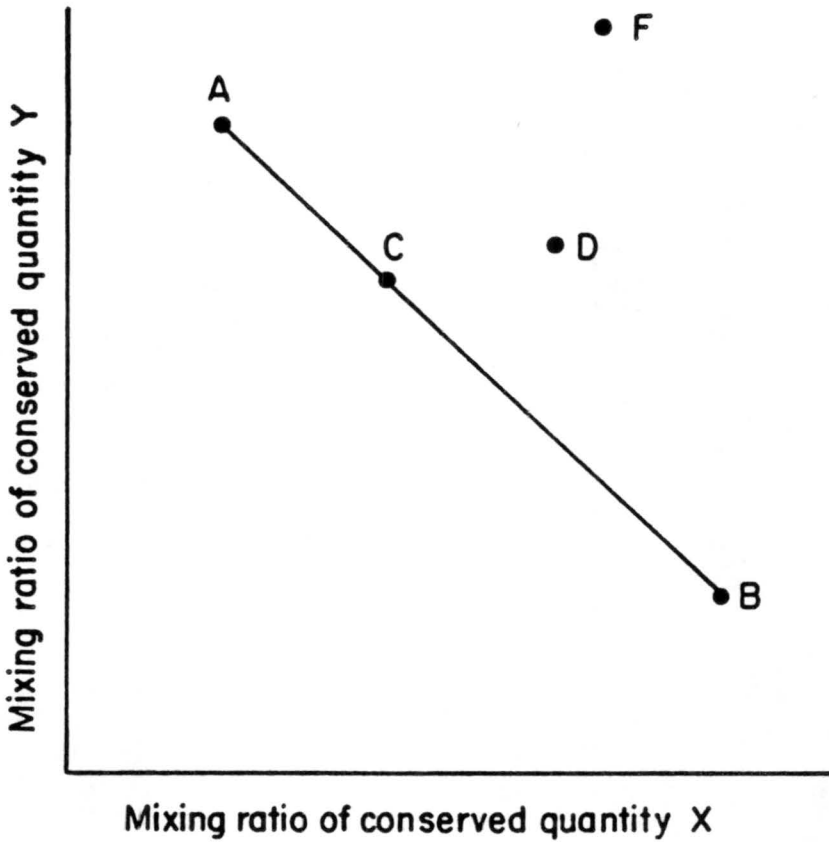


Figure 1.2. A hypothetical mixing line diagram which graphically illustrates information about the possible mixtures of two different parcels of air A and B. Both parcels are plotted in terms of two independent conserved quantities X and Y. If we form a parcel C by mixing A and B in a 2:1 ratio it will fall on the line connecting A and B such that the ratio of the length of line \overline{BC} to \overline{CA} is the ratio of A to B in the mixture. If a parcel D is sampled and plotted it is clear that it is not solely a mixture of A and B because it does not lie on \overline{AB} . Parcel D might be a mixture of A, B and another parcel, possibly F.

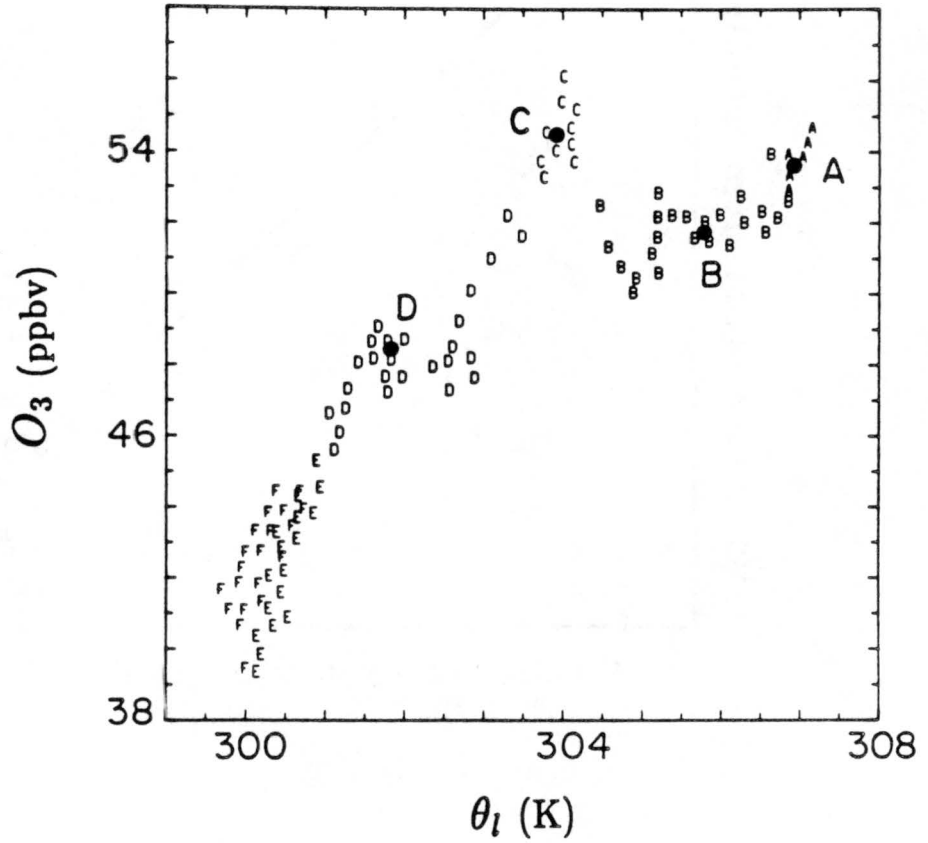


Figure 1.3a. Mixing line diagram of (θ_l, O_3) . Data are from the profiles of Figure 1.1 and points are labeled according to their layer. Overlapping points from the same layer are not shown and the solid circles are the locations of the highest concentration of points for a given layer.

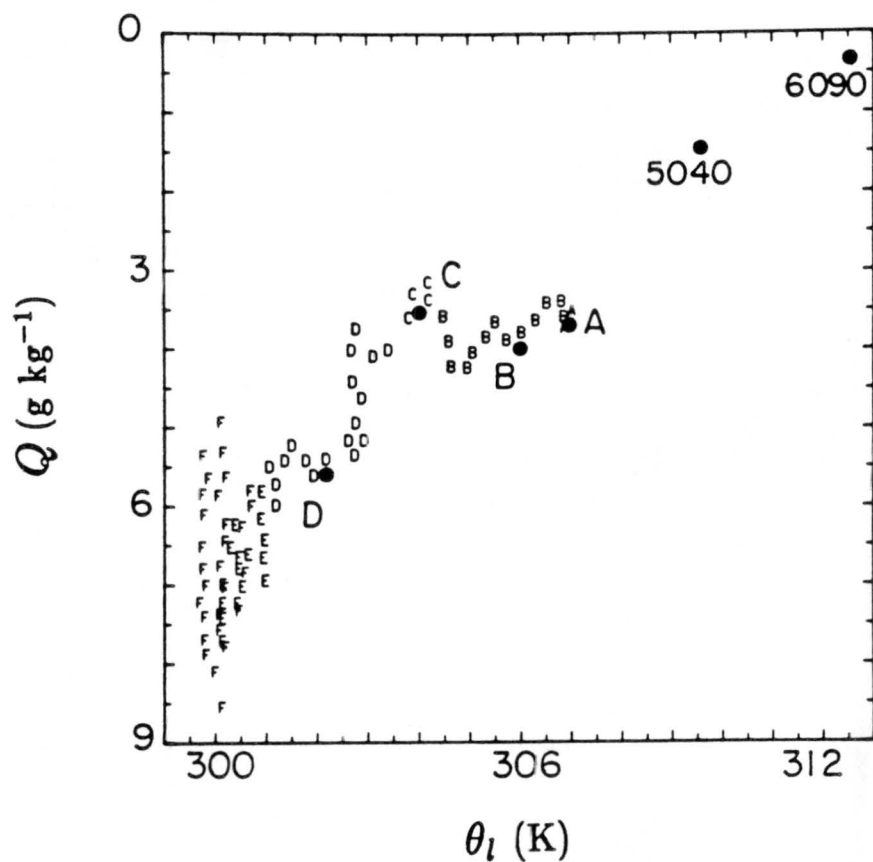


Figure 1.3b. Mixing line diagram of (θ_l, Q) for the data in Figure 1.1. Two points from the Colstrip, MT sounding at 1310 MDT are labeled by altitude in m AGL.

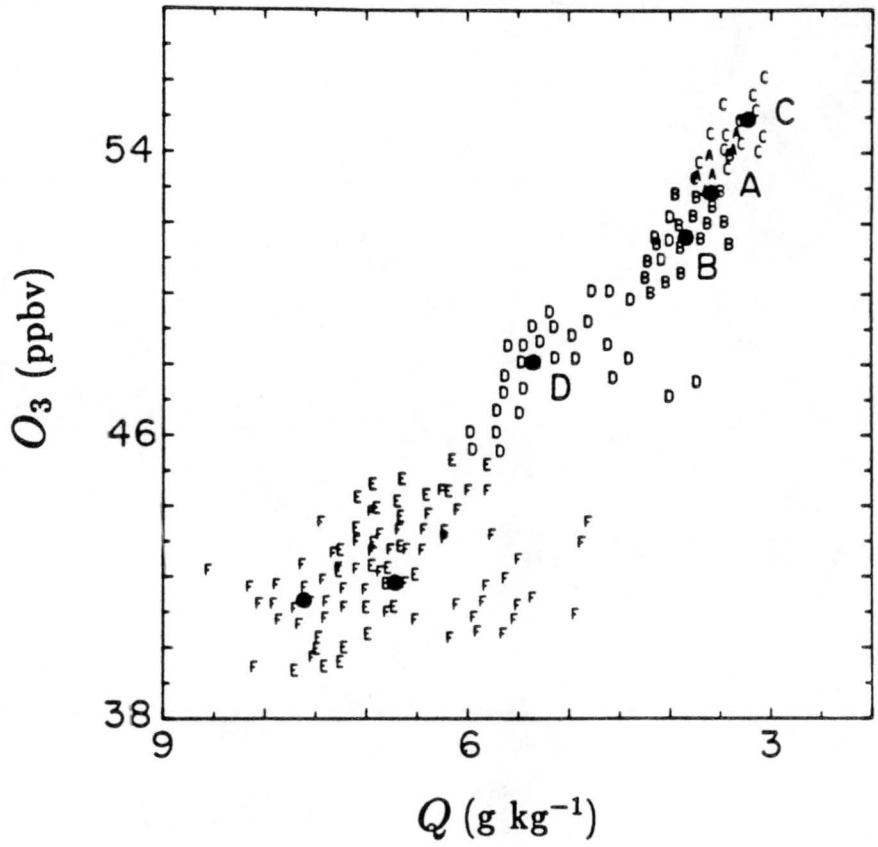


Figure 1.3c. Mixing line diagram of (Q, O_3) for the data in Figure 1.1.

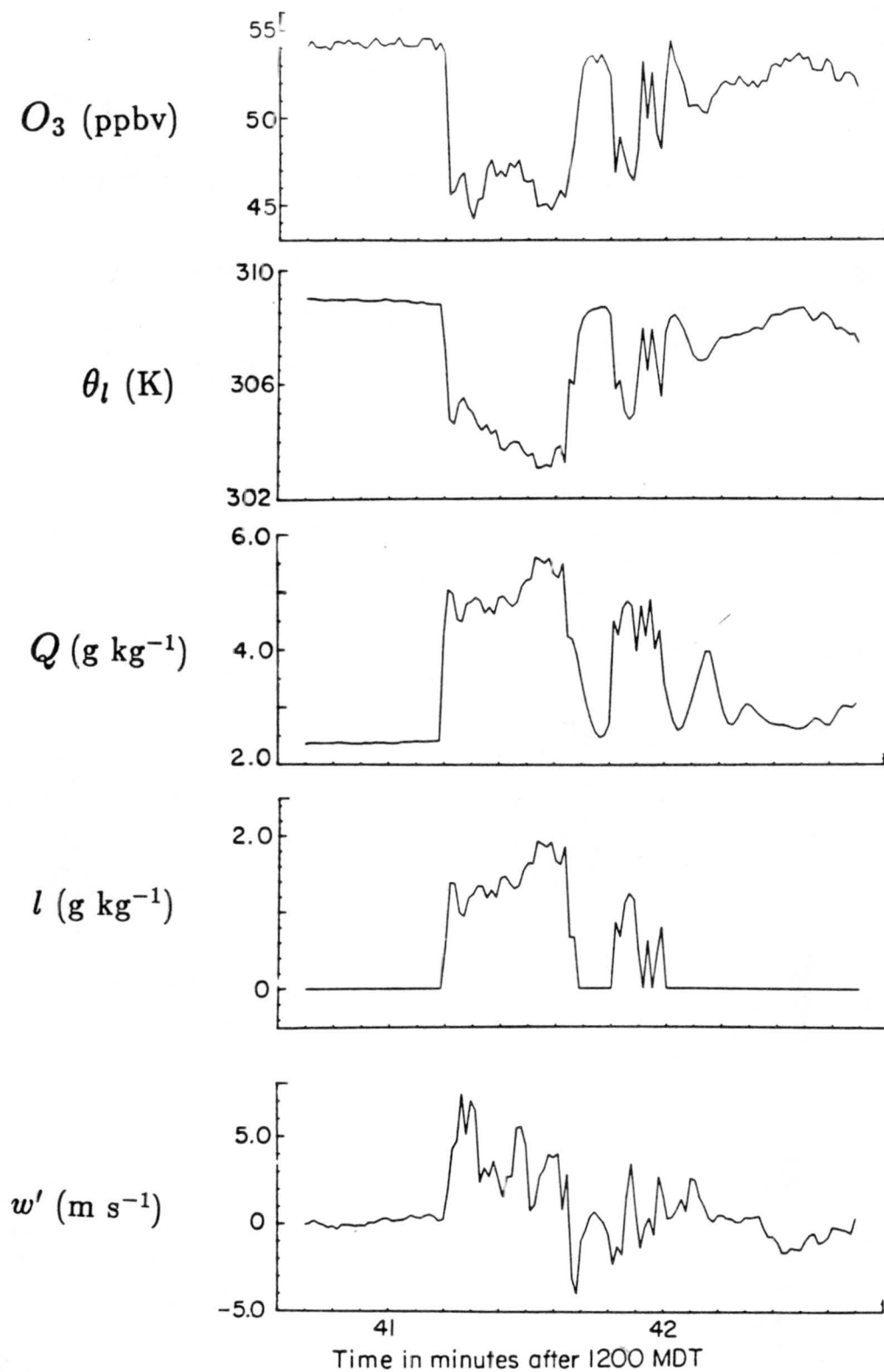


Figure 1.4. Time series of O_3 , θ_l , Q , l and w' during the highest cloud penetration of Case 1 at 4300 m.

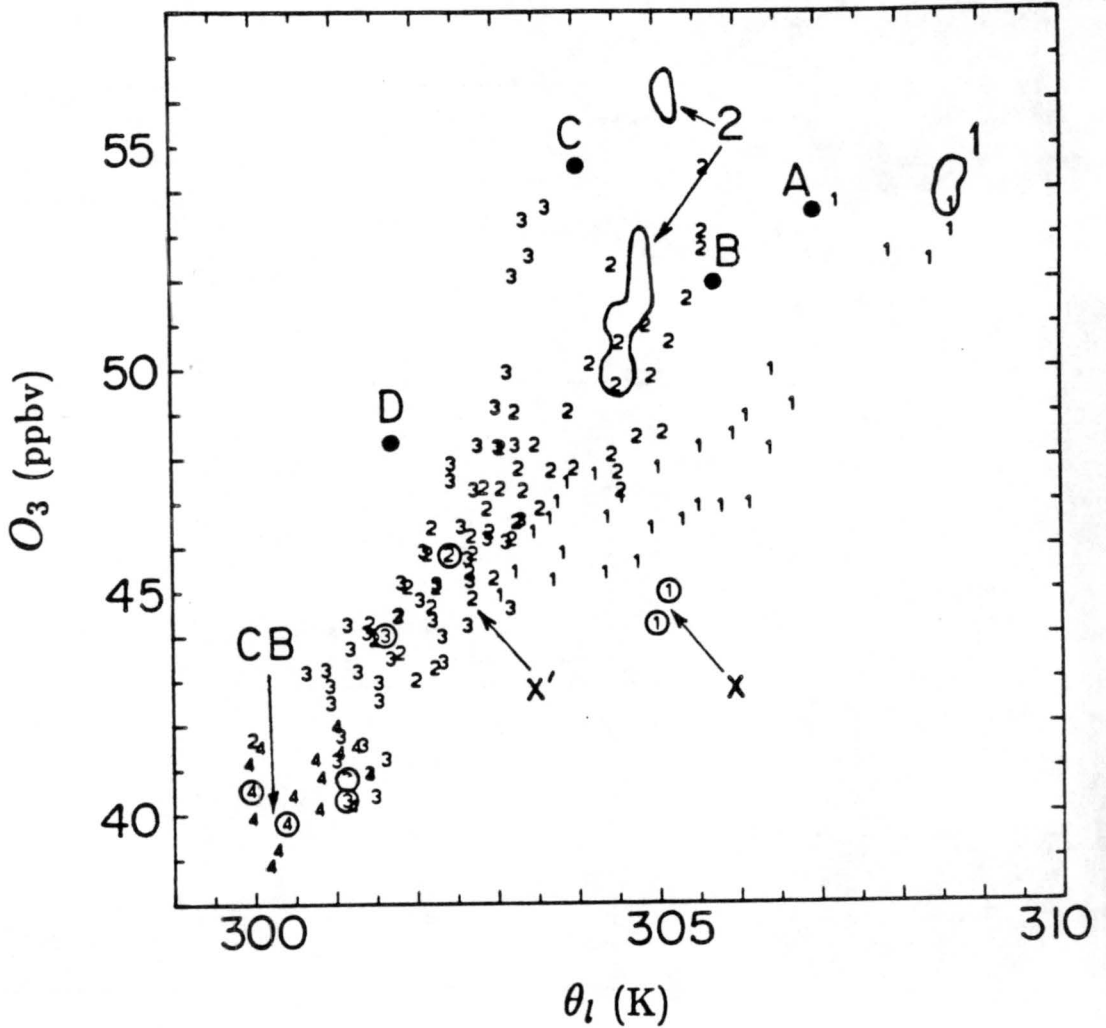


Figure 1.5a. Mixing line diagram of (θ_l, O_3) , using in cloud and environmental data from Case 1. One second averaged in cloud points from each penetration level are labeled as follows: 1 - 4300 m level, 2 - 3670 m level, 3 - 3070 m level and 4 - 2452 m level. A high fraction of the environmental points sampled moments before or after the cloud was encountered at the two highest penetration levels are within the enclosed areas labeled as follows: 1 - 4300 m level and 2 - 3670 m level. The solid circles are from Figure 1.3. The cloud base is labeled by CB. See text for definition of X and X'.

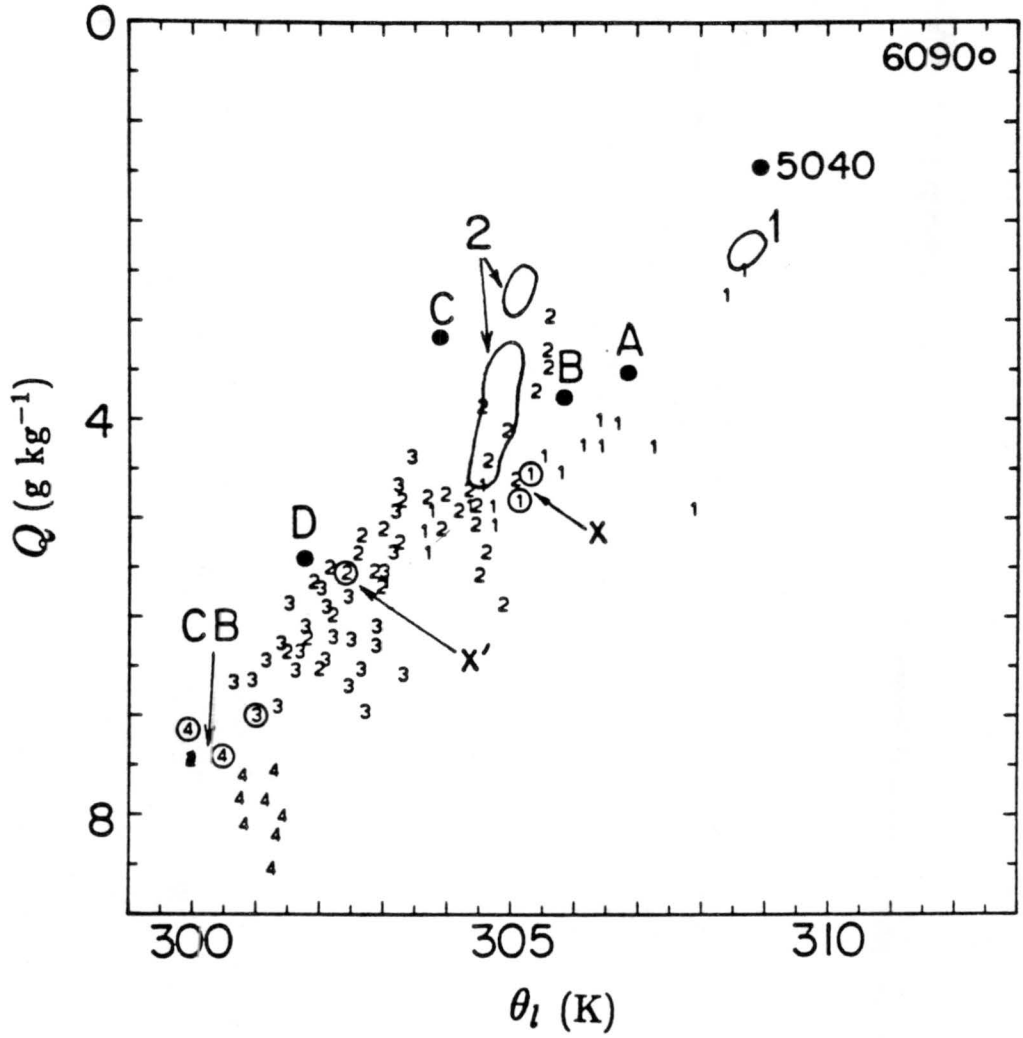


Figure 1.5b. Mixing line diagram of (θ_l, Q) for Case 1. See Figure 1.5a for details.

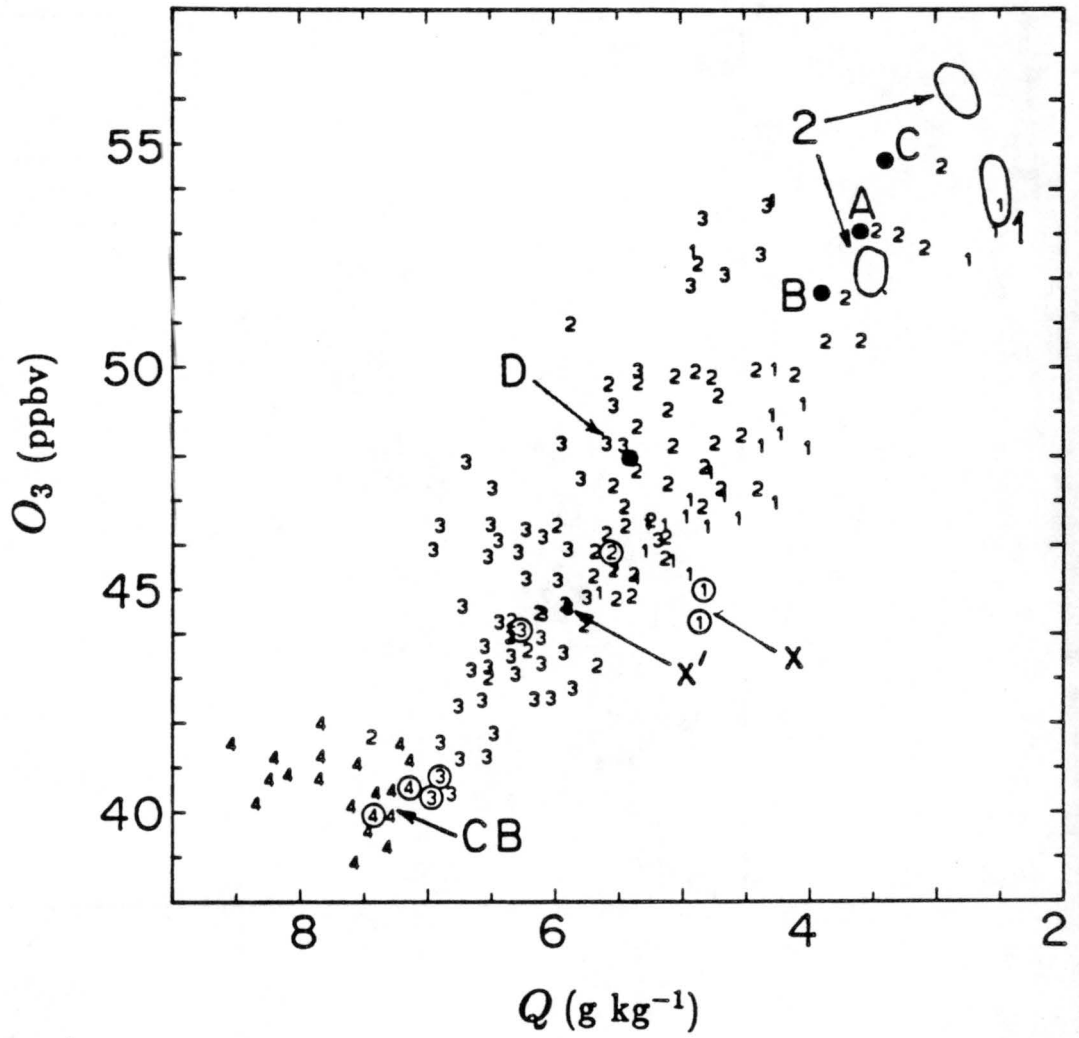


Figure 1.5c. Mixing line diagram of (Q, O_3) for Case 1. See Figure 1.5a for details.

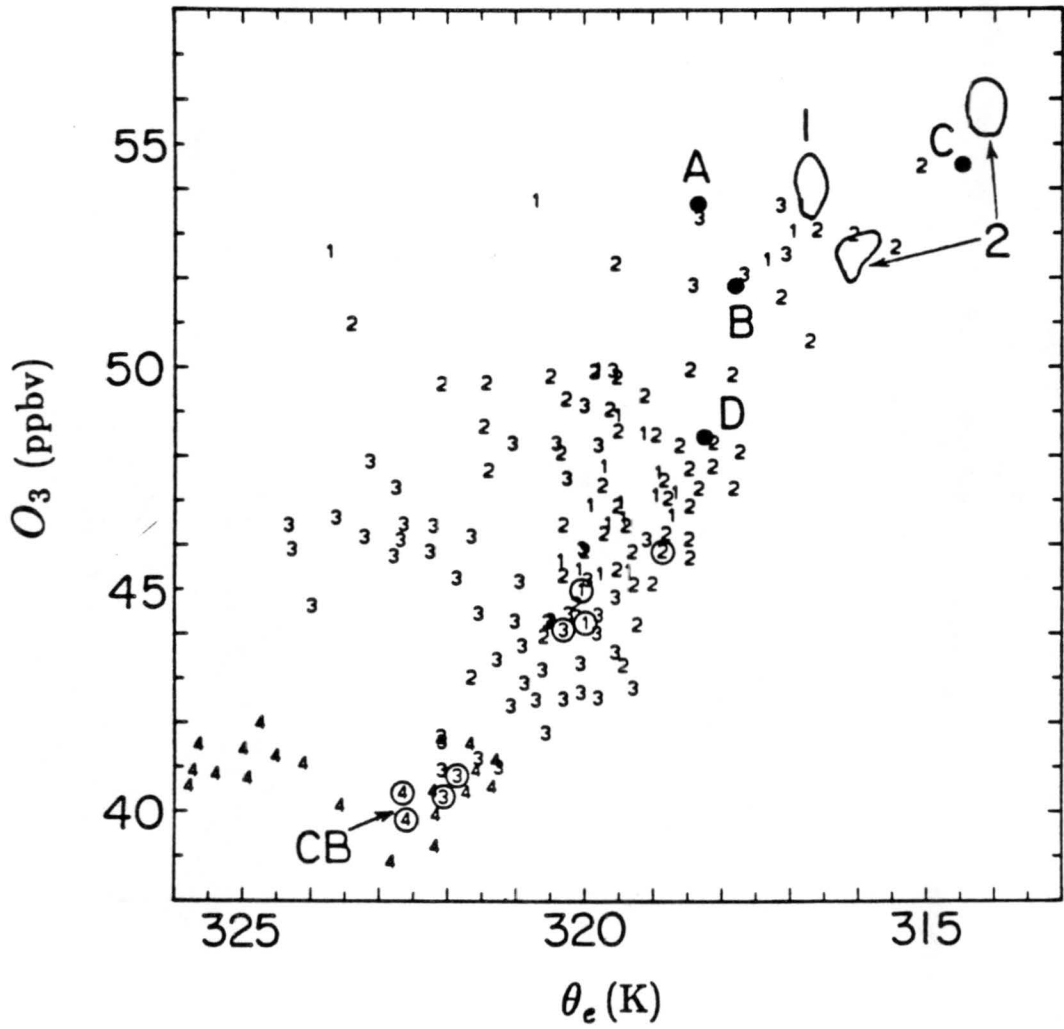


Figure 1.5d. Mixing line diagram of (θ_e, O_3) for Case 1. See Figure 1.5a for details.

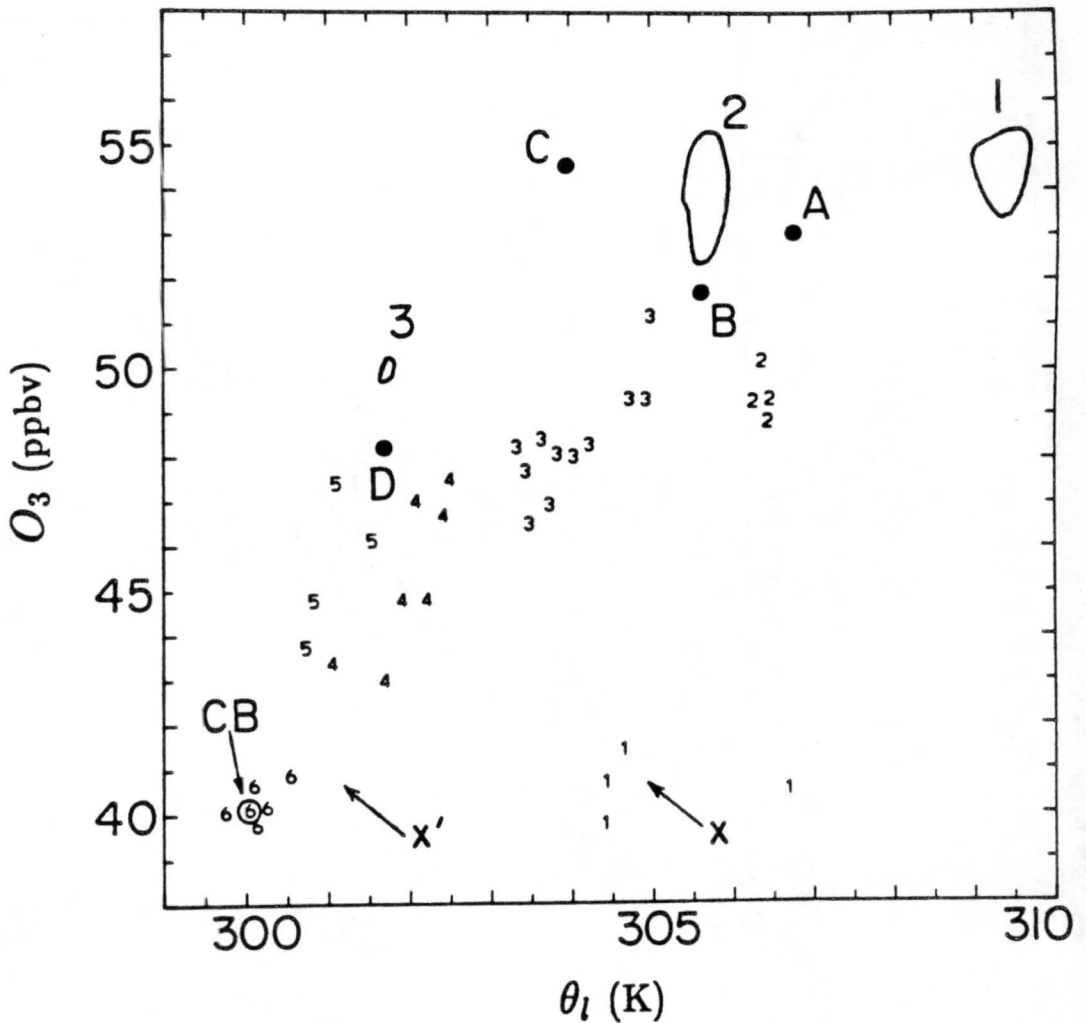


Figure 1.6a. Mixing line diagram of (θ_l, O_3) , for Case 2. One second averaged in cloud points from a specific region of the cloud are labeled as follows:

- | | |
|-----------------------------|----------------------|
| 1 - 4320 m updraft | 2 - 4320 m downdraft |
| 3 - 3660 m downshear region | 4 - 3660 m updraft |
| 5 - 3070 m updraft | 6 - 3070 m updraft |

As in Figure 1.5 the enclosed areas show the environmental air sampled outside the cloud for the three penetrations (1 - 4320 m level, 2 - 3660 m level and 3 - 3070 m level). Points labeled 5 and 6 are from different updraft regions. The solid circles are from Figure 1.3. The cloud base is labeled by CB. See text for definition of X and X'.

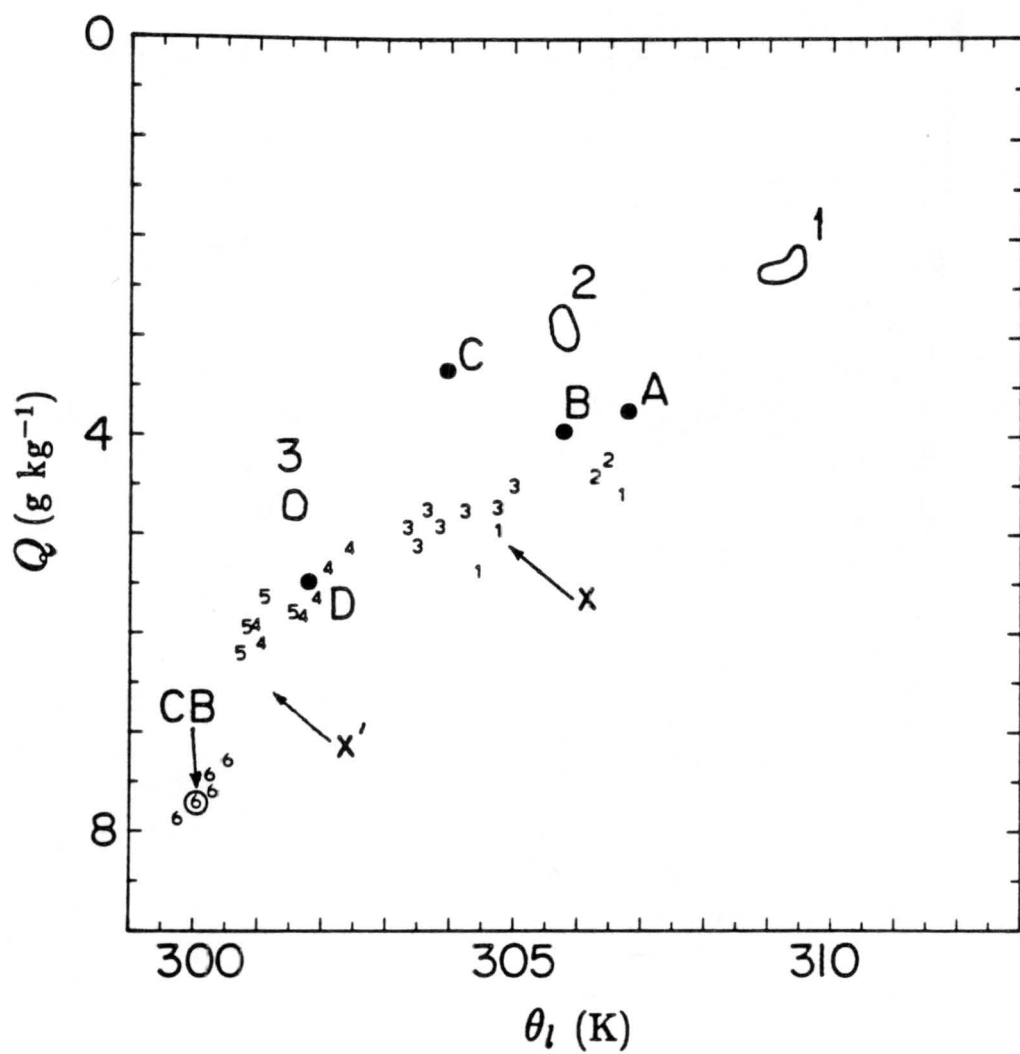


Figure 1.6b. Mixing line diagram of (θ_l, Q) for Case 2. See Figure 1.6a for details.

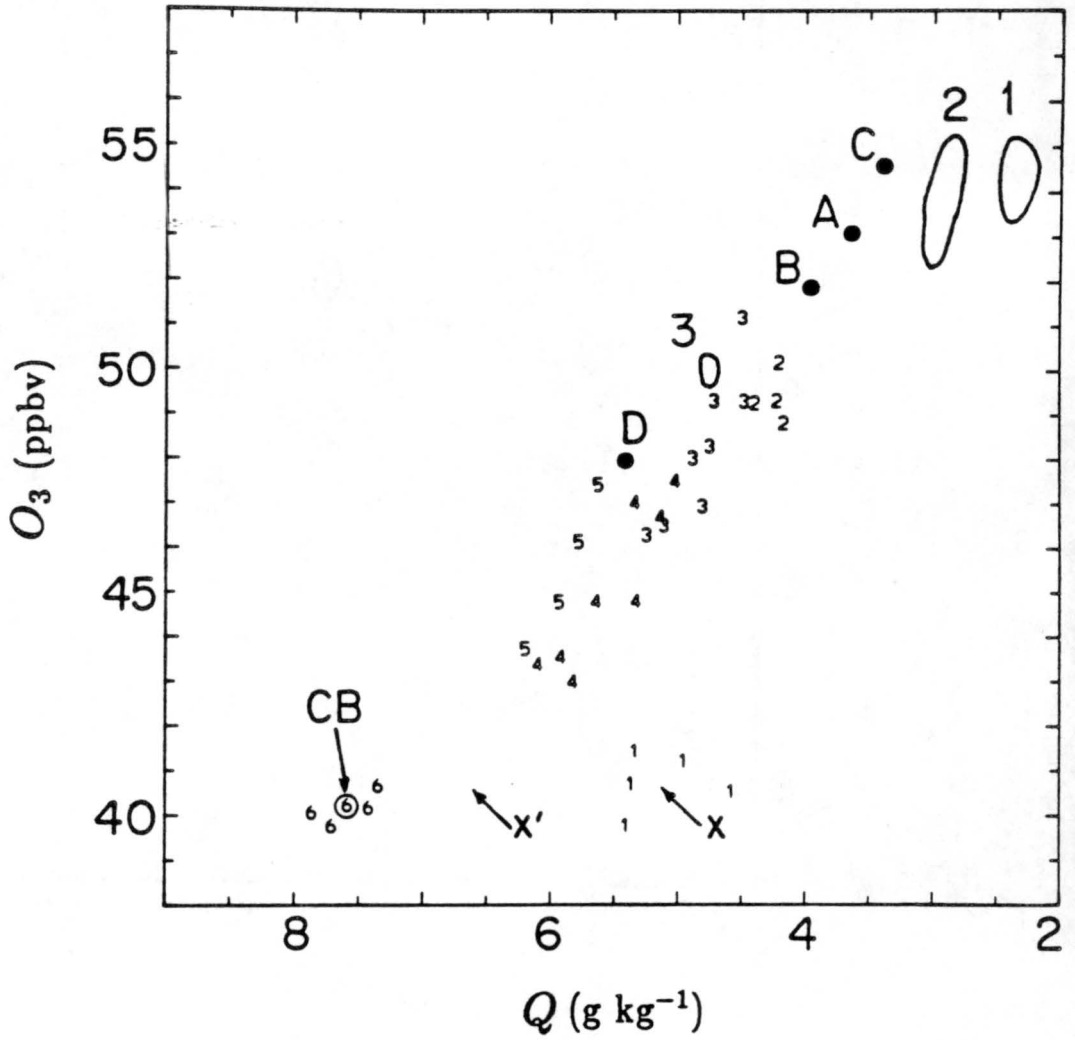


Figure 1.6c. Mixing line diagram of (Q, O_3) for Case 2. See Figure 1.6a for details.

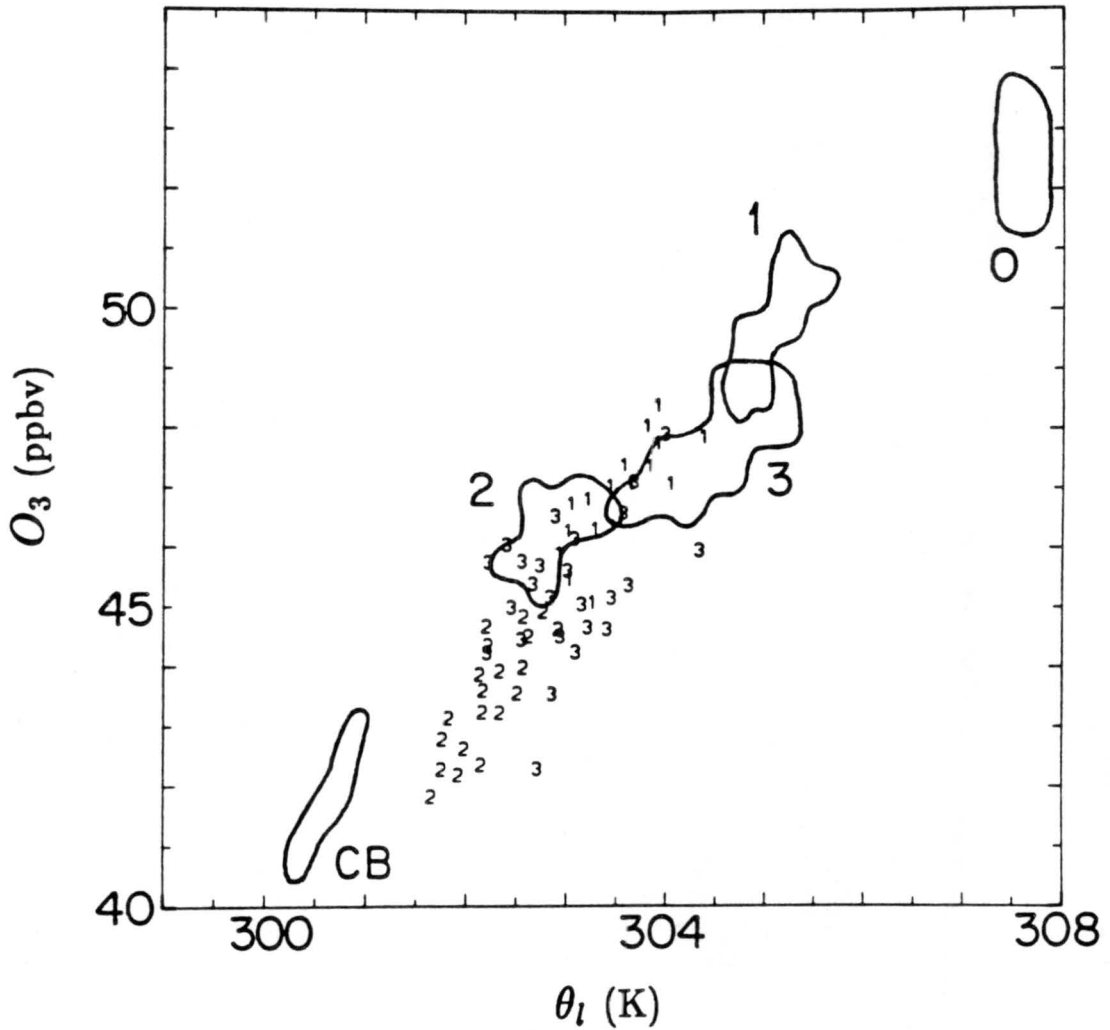


Figure 1.7a. Mixing line diagram of (θ_l, O_3) , for Case 3. One second averaged in cloud points from each penetration level are labeled as follows: 1 - 3540 m level, 2 - 2930 m level, 3 - 3240 m level. The environmental air sampled outside the cloud is labeled with the corresponding number. Environmental air from the 4000 m level above cloud top is labeled by 0. Subcloud air from 2000 m is labeled CB and denotes the range of possible cloud base values.

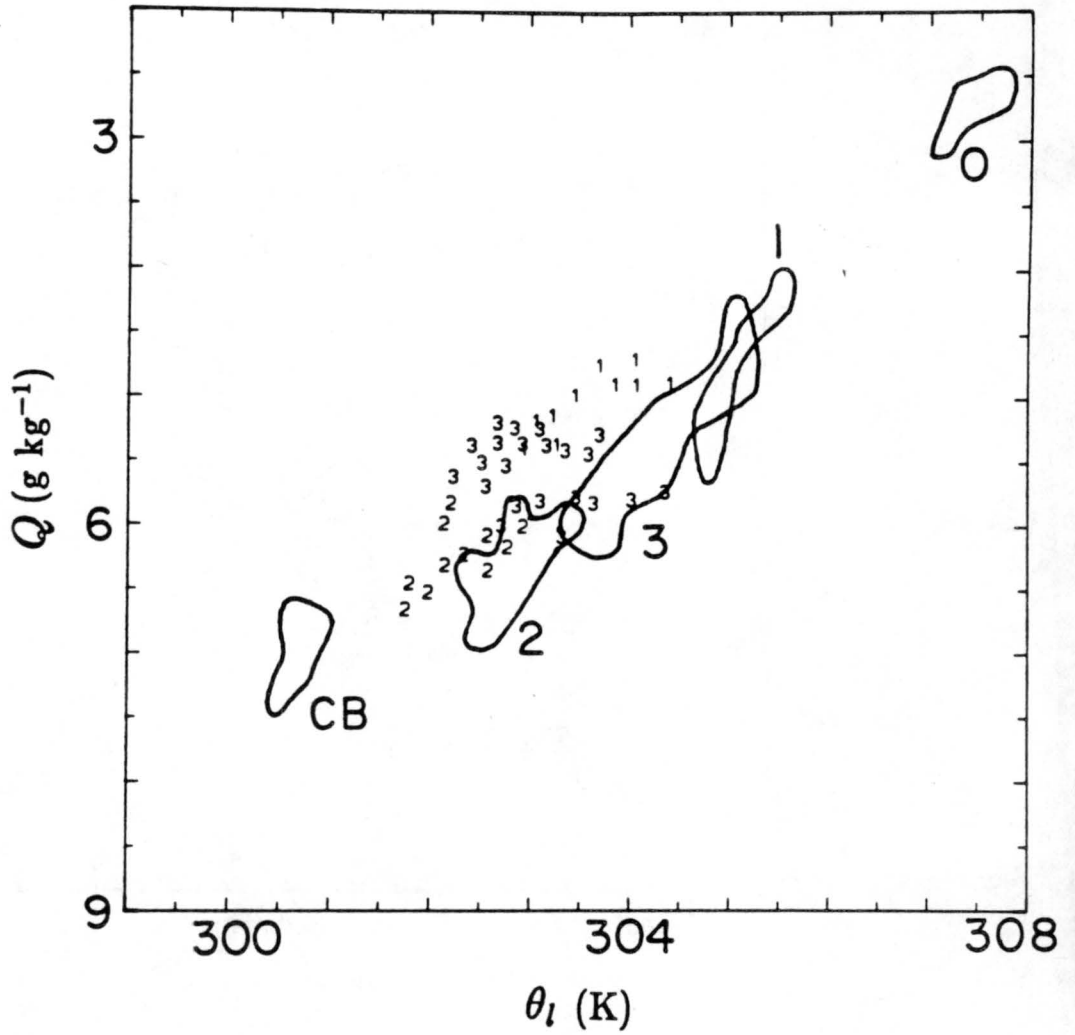


Figure 1.7b. Mixing line diagram of (θ_l, Q) for Case 3. See Figure 1.7a for details.

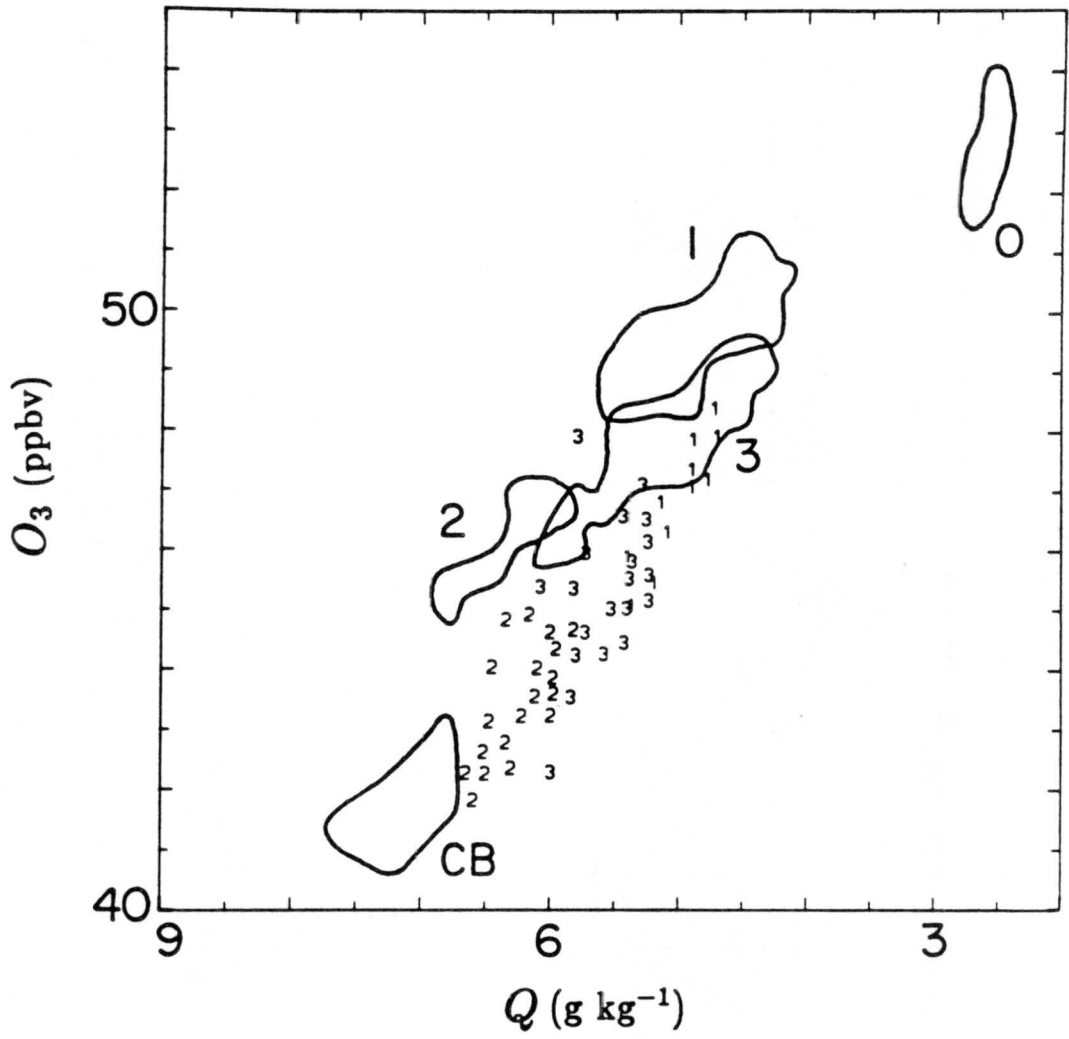


Figure 1.7c. Mixing line diagram of (Q, O_3) for Case 3. See Figure 1.7a for details.

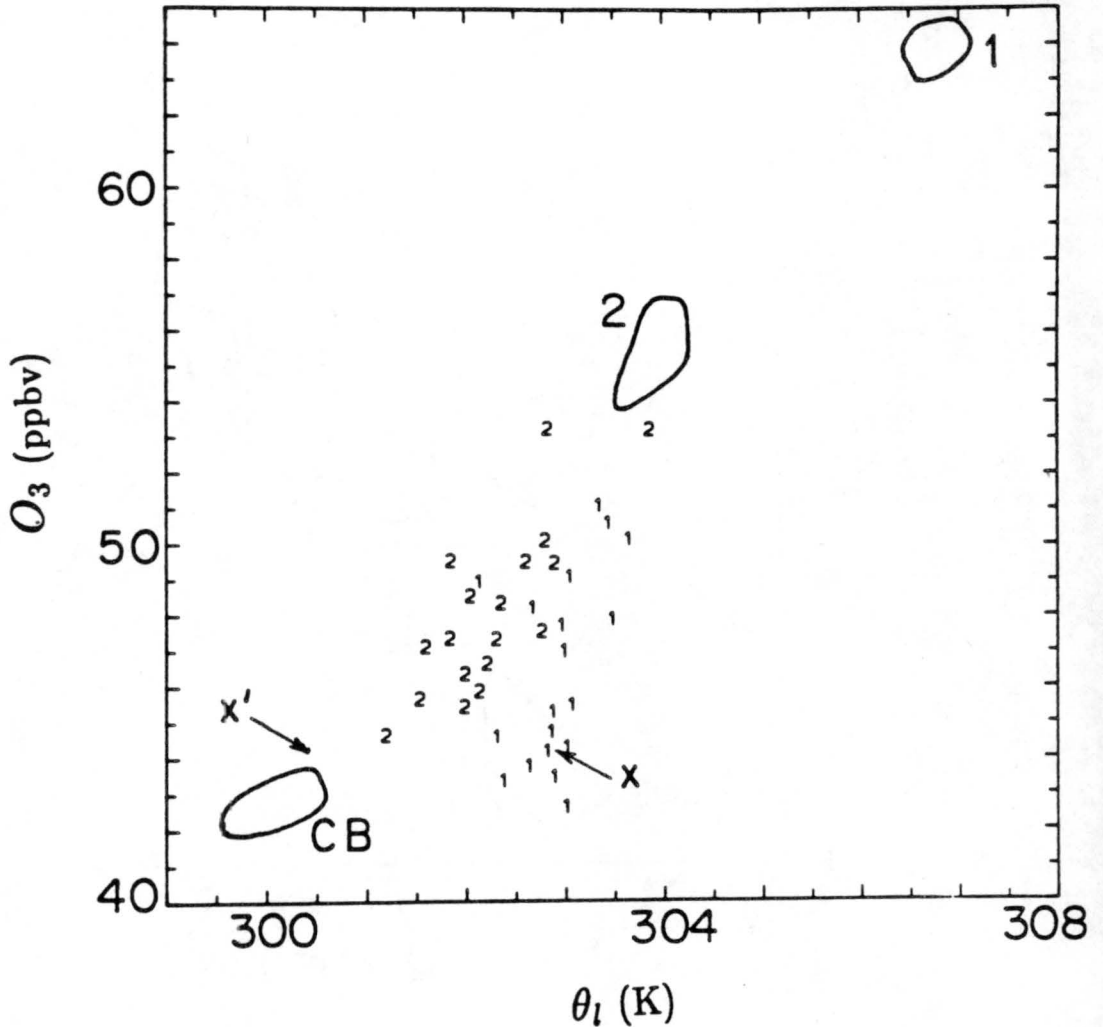


Figure 1.8a. Mixing line diagram of (θ_l, O_3) , for Case 4. One second averaged in cloud points from the highest penetration level at 4000 m are labeled as follows: 1 - updraft region and 2 - downshear region. The two enclosed areas are locations of environmental points sampled at 4000 m just outside the cloud. The enclosed area labeled CB is the range of cloud base values from the lowest cloud penetration level. See text for definition of X and X'.

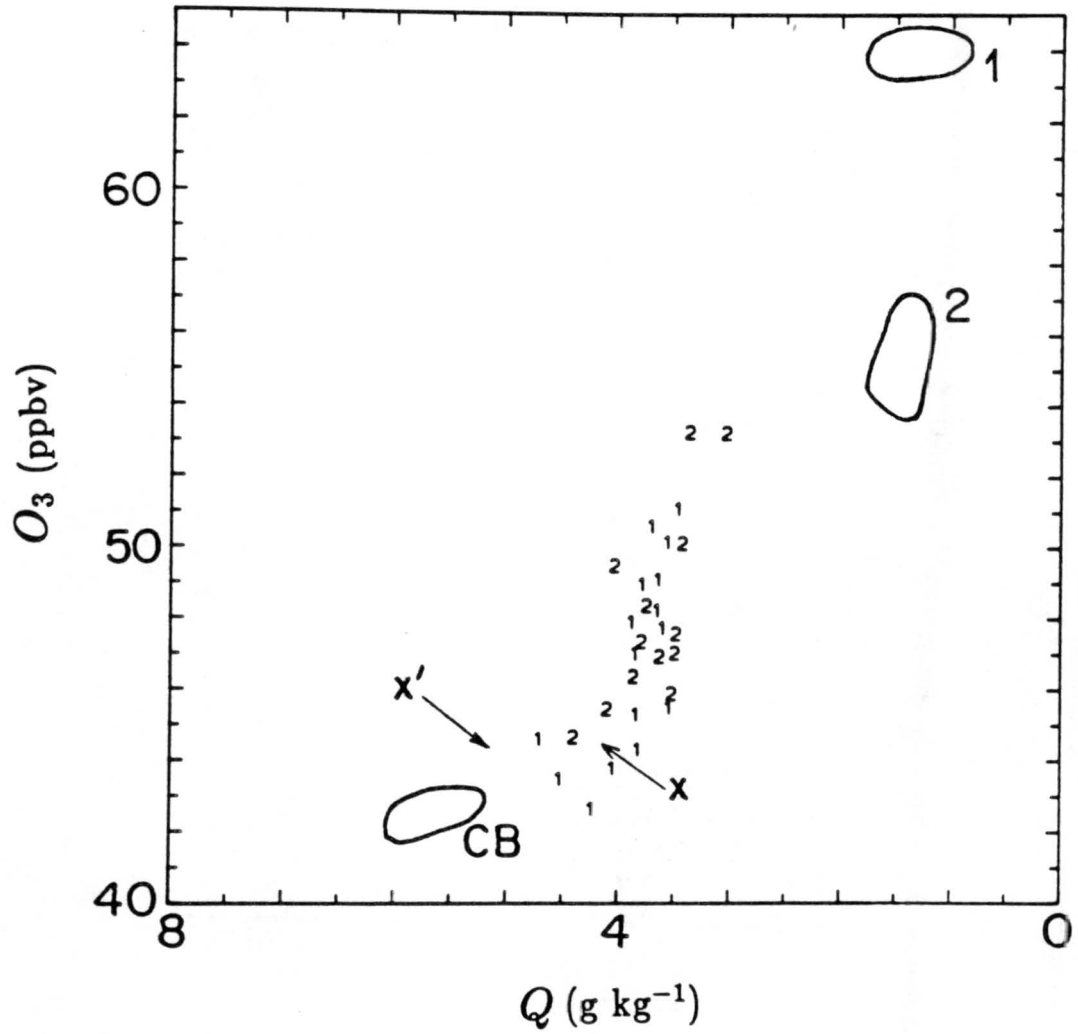


Figure 1.8b. Mixing line diagram of (Q, O_3) for Case 4. See Figure 1.8a for details.

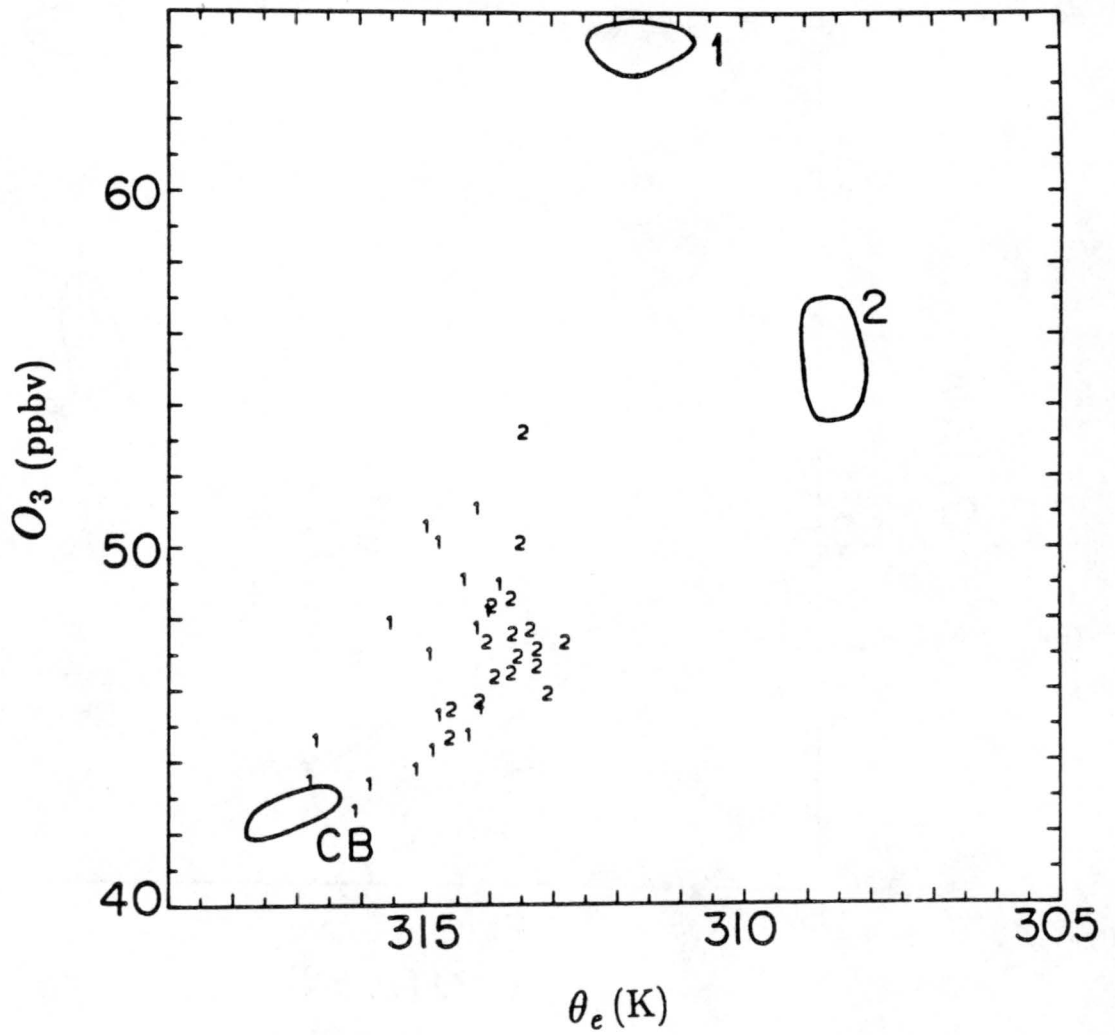


Figure 1.8c. Mixing line diagram of (θ_e, O_3) for Case 4. See Figure 1.8a for details.

Chapter 3: DISCUSSION

Our principle objective is to investigate ozone conservation during moist convection. Since the cloud is neither stationary nor horizontally homogeneous, it is not possible to employ the budget equations for a scalar (Lenschow et al., 1980) directly to the cloud. But it is possible to ask whether the processes which may account for the distribution of points on the (θ_t, Q) diagram are also consistent with the corresponding diagrams employing O_3 . To answer this, three topics bear discussion. First, I discuss the mixing line analysis. Second, I discuss the interpretation of those in-cloud points at the highest levels sampled which appear to have mixing scenarios which vary with the diagram considered. The underlying cause has been attributed to icing of the liquid water sensor and I give a more detailed discussion. Third, I discuss problems with θ_t and Q .

3.1 Mixing Line Analysis

Throughout this study I have interpreted the composition of in-cloud air as if it were a two or three-part mixture of cloud base and environmental air. Since the cloud probably entrains air from a range of altitudes, this is an oversimplification and we may be unable to determine the more complicated aspects of the mixing process. However, we can describe those processes that could have physically occurred and those that were impossible as dictated by the mixing diagrams. It is also significant that the time to sample the cloud was on the order of the cloud's lifetime (c.a. 30 min). We have assumed that properties measured at a given location remained constant throughout the study even though this may not have been the case.

3.2 In-cloud Points Subject to Icing

Those in-cloud points labeled by 1's in Cases 1, 2 and 4 appear to have mixing scenarios which vary with the mixing diagram considered. For every case the (θ_l, O_3) and (Q, O_3) diagrams placed these points to the right of the mixing line connecting cloud base with the environment from the highest penetration. The (θ_l, Q) and (θ_e, O_3) diagrams always placed the points close to or on this line. The (θ_e, O_3) diagram for Case 2 is not shown, but is similar to the corresponding diagram from Case 4. One might argue that the environmental O_3 profile above the highest penetration level might account for these points and that this unsampled air is entrained. However, this profile tends to disagree with the climatological ozone profile which increases with height. Further, this explanation can be ruled out because the (θ_e, O_3) diagram has these points on this mixing line. As discussed above, this apparent discrepancy is resolved if we assume that measurements of l are systematically low, and corresponding adjustments are made in θ_l and Q .

A plausible explanation for the error in l is accumulation of ice on the JW liquid water probe at the coldest cloud temperatures measured. The JW probe consists of two wires: a sensing wire, cooled by evaporating cloud droplets as well as by convection; and a compensating wire subject to the same convective losses, but placed so that it should not encounter droplets. The difference in the resistance of the two wires, as measured by a Wheatstone bridge, is a function of the liquid water content. Faulty readings occur when ice builds up on the compensating wire and bridges to the instrument body which is at electrical ground. Although ice is not a good conductor, enough current is siphoned to ground so that the resistance of the wire appears higher to the sensing electronics than that due to convective heat losses alone. This leads to overcompensation and liquid water content readings which are below the true value or even negative (Baumgardner, 1985). Heaters designed to minimize this problem were available, but could not

be operated at the same time as the O_3 measurements due to limited power on board the research aircraft.

The response of the JW during an icing episode under laboratory conditions has been described by Straap and Schemenauer (1982) during wind tunnel calibrations. Their description fits our JW response at the high penetration levels. A buildup of ice on the compensating wire was observed at temperatures below $-15\text{ }^\circ\text{C}$ when the probe heaters were operating. During the icing episode, they found that the baseline value went below zero when the instrument was removed from the liquid water spray. It regained its zero value, presumably, as the ice was shed.

We observed similar behavior at -7 to $-9\text{ }^\circ\text{C}$ operating the JW without deicing heaters. The JW signal would often abruptly fall below zero as the aircraft left the cloud. Shortly thereafter it would rise to the baseline value. Presumably, ice had accumulated on the probe during the penetration and remained as the airplane left the cloud thereby causing the negative readings. But as the ice melted (or was shed) during the next 10 to 20 s, the baseline returned to its value at the start of the penetration. A correction factor was added to the data during suspected icing episodes in an attempt to compensate for this problem. Nevertheless, JW values in this work from temperatures significantly below freezing are probably not reliable.

3.3 Choice of Thermodynamic Parameters for Mixing Line Analysis

Given the difficulties in measuring l in supercooled water, one might be led to conclude that θ_e , which is independent of l , should be the preferred thermodynamic temperature for use in mixing line analysis. Here we show that this view is incorrect because it overlooks the strong functional dependence of θ_e upon water vapor mixing ratio (q), and some formidable experimental obstacles to measuring q in and around clouds.

3.3.1 Mathematical Dependence of θ_e and Q on q

Ideally, mixing line analysis should employ quantities which are totally independent of one another. Then for a binary mixing process, the regression of two scalar quantities would be expected to yield points along a straight line as in Figure 1.2. In the absence of such a process, points would not be expected to fall along a straight line unless the quantities were mathematically dependent. It is difficult to tell by inspection whether linear correlation is the result of mixing, or simply the result of an underlying dependence in the definition of the terms. Mixing diagrams for θ_e and Q are an example of the latter case in which the dependence arises from the definition of the parameters, as can be seen in Figure 1.9a. It will be shown that the strong linear dependence in (θ_e, Q) diagrams makes conclusions about mixing ambiguous.

The four conserved quantities O_3 , θ_l , θ_e , Q can be thought of as dependent variables and are functions of independent variables which are measured directly. The approximate linearized functions are:

$$O_3 = (1 + 5q)O_{3m}$$

$$Q = q + l$$

$$\theta_l = \theta - (L/c_p)l$$

$$\theta_e = \theta + (L/c_p)q.$$

The independent variables are q , l , potential temperature (θ), and measured ozone mixing ratio (O_{3m}). The subscript m denotes raw values from the ozone instrument not yet corrected for water vapor. The first equation removes the dependence of O_{3m} on q (Lenschow et al. 1981). Here L is the heat of vaporization of water and c_p is the heat capacity of dry air. The formulas for θ_l and θ_e shown have been simplified to show the linear dependencies on either q or l ; the more exact ones were used in the analysis. When two dependent variables are used in

a mixing diagram, the tendency for the points to fall on a line can be a function of how linearly dependent they are. Let R be the linear correlation coefficient for a two-parameter diagram. A quantitative measure of this linear dependence is obtained by randomizing the independent variables, calculating the dependent variables and considering the new correlation coefficient, R_{mix} . The result will be that θ_e at a given time might use θ measured 10 s earlier and q measured 20 s later. When $|R_{mix}|$ is close to unity, the quantities are probably mathematically dependent, and the resulting diagrams will be of limited use in studying mixing processes.

The boundaries shown in Figure 1.9a and 1.9b are the domain of possible points when this randomization process is done on the in-cloud data from Case 1. Note how the (θ_e, Q) domain is elongated along the e_1 axis and squashed along the e_2 axis. The points shown in Figure 1.9a are not randomized and $R = 0.88$. When the dependent variables are evaluated with the randomization process, they fill the domain shown and still have a strong correlation $R_{mix} = 0.83$. The randomization removes any physical dependence but the mathematical dependence on q remains. The unrandomized (Q, O_3) points shown in Figure 1.9b also have a high correlation $R = 0.87$ but the domain for this pair does not favor a particular axis and $R_{mix} = 0.09$. Although there is a slight mathematical dependence on q it is small and the value of R is physically real. Correlation values for all pairs are:

$$(\theta_e, Q) \quad R = 0.88 \quad R_{mix} = 0.83$$

$$(Q, O_3) \quad R = -0.87 \quad R_{mix} = 0.09$$

$$(\theta_l, O_3) \quad R = 0.85 \quad R_{mix} = -0.03$$

$$(\theta_e, O_3) \quad R = -0.66 \quad R_{mix} = 0.07$$

$$(\theta_l, Q) \quad R = -0.88 \quad R_{mix} = -0.09.$$

Just as θ_e and Q are dependent on q , so θ_l and Q are dependent on l . However, q is only a weak function of l since $l \ll q$ and thus θ_l is the preferred quantity to use.

The (θ_e, Q) diagram can be used in a mixing line analysis but the underlying functional dependence complicates matters. When using the (θ_e, Q) diagram, at least for the clouds in this study, the functional dependence and the uncertainties in the data can mislead one into concluding that more combinations of parcels are mixing than is inferred from other diagrams.

3.3.2 Limitations on Moisture Measurements

A second problem for θ_e , mentioned above with regard to Q , is the response of the dew point hygrometer near the downshear edge of the cloud where the aircraft encounters pockets of unsaturated air. Immediately after the aircraft encounters an area of subsaturation after flying through cloud, the cooled mirror still is covered with liquid water. Erroneous dewpoints are recorded until the instrument equilibrates by evaporating most of the liquid water leaving a thin film of dew on the mirror. Further complicating the measurement of q in this region is the classification of points as saturated or unsaturated. For this study, l was used to determine saturation. Because l is subject to the accuracy of the baselining procedure, it is easy to misclassify points as saturated or unsaturated. Both these problems could be avoided using a cloud droplet spectrometer (Particle Measuring Systems, Inc.) to determine when to use the saturation assumption in combination with the Lyman- α hygrometer which does not have the response problems of the cooled mirror. But for this study points at the edge of the cloud were analyzed on the (θ_l, O_3) diagram which is not subject to either of these problems.

3.4 Ozone as a Conserved Quantity

The primary objective of this study was to test ozone conservation in cumulus convection. The mixing line diagrams all showed that O_3 behaved generally like the thermodynamic tracers confirming our hypothesis. When there was disagreement, I argue that it can be traced to problems in the thermodynamic quantities

rather than ozone. These are: problems in measuring l , the mathematical dependence in the (θ_e, Q) diagram and the classification of some unsaturated points as saturated or vice versa. Not observed in this study, but equally important, is the potential for inaccurate temperature measurements by the reverse flow thermometer in warm clouds (Lawson and Rodi, 1987). As other thermometers are subject to this problem (except for those measuring radiometric temperature) measurement of temperature can be added to the list of problems. Ozone is immune from problems involving temperature, saturation and is only weakly dependent on moisture. It can therefore be used to verify the thermodynamic quantities.

While testing for ozone conservation we have been able to learn something about the the cloud entrainment process as well. Figure 1.10 is a schematic cloud mixing diagram incorporating the conclusions of Cases 1,2 and 4. This schematic diagram is not intended to show every observation, but instead is to aid in the discussion. It shows that the core (i.e. the strongest updrafts associated with the highest l values) at a given penetration level contained a high fraction of cloud base air. Furthermore, the entrained environmental air tends to come from altitudes at or below the penetration level. This is represented by the boxes in the upshear part of the cloud. The downdrafts found in the downshear part of the cloud contain a higher fraction of environmental air than the updrafts, which originate at or within several hundred meters above the penetration altitude. The right most box shows that parcels at the extreme downshear portion of the cloud with little vertical motion are cloud mixtures highly diluted with environmental air.

Ozone is important to these detailed conclusions. Without it they would have been less rigorous and possibly incorrect. Conclusions based solely on the (θ_e, Q) diagram indicate that at the highest penetration levels the deeper clouds were entraining air from above the observation level. This would tend to support the theory of cloud-top entrainment. However, those mixing diagrams employing O_3 pointed up the fact that our l was still underestimated at the highest penetration

levels, even though we tried to correct for icing by baselining the l time series. With the use of O_3 , it appears instead that the entrainment is lateral at the higher levels.

It is highly recommended that O_3 be sampled during future cloud entrainment studies. With O_3 , three or four mixing diagrams are available compared with one or two using conventional techniques. More detailed and accurate conclusions are possible and confidence in the results is increased.

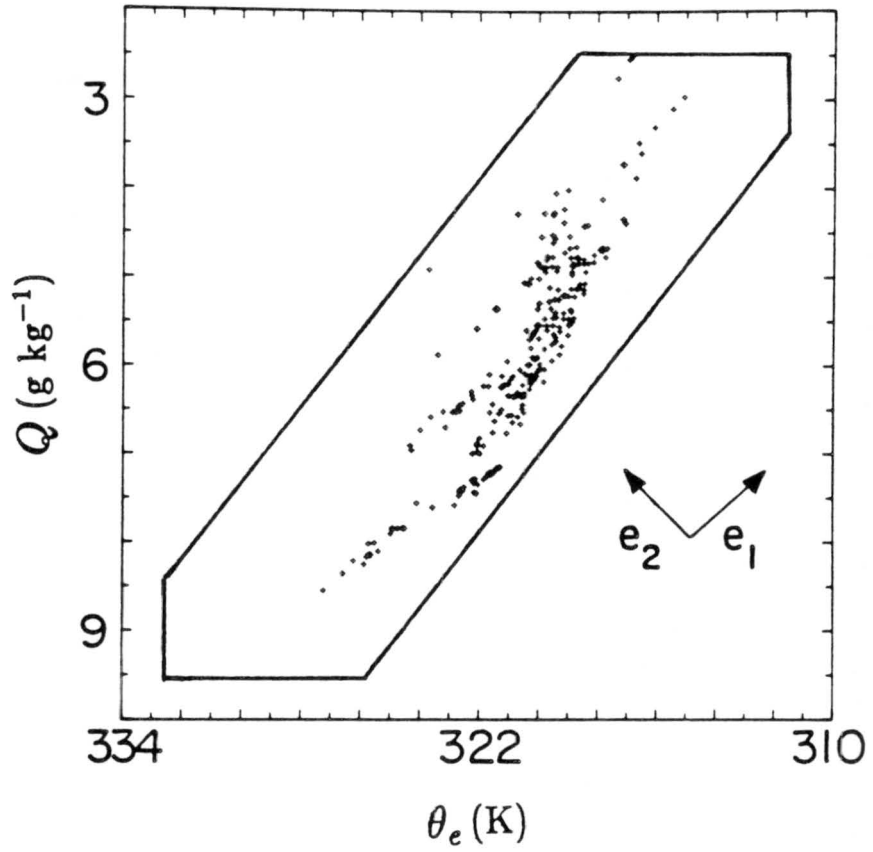


Figure 1.9a. Mixing line diagram of (θ_e, Q) showing only the in-cloud points from Case 1. Boundaries shown are described in the text.

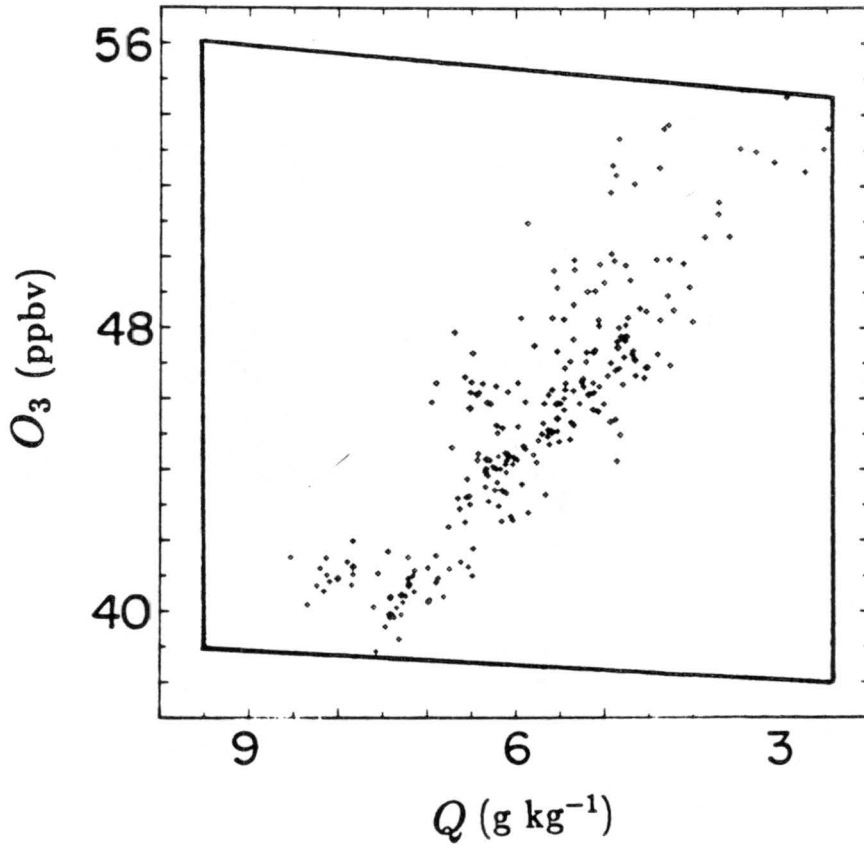


Figure 1.9b. Mixing line diagram of (Q, O_3) showing only the in-cloud points from Case 1. Boundaries shown are described in the text.

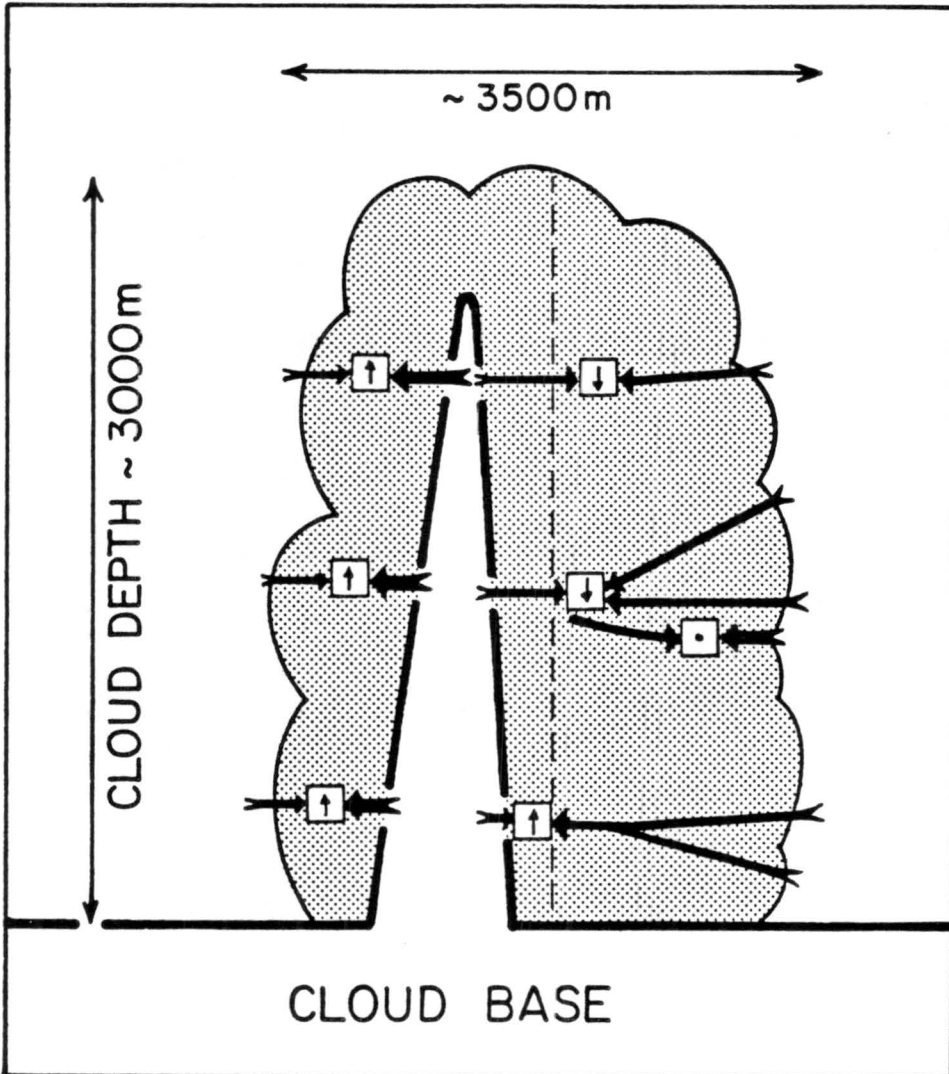


Figure 1.10. Schematic diagram of entrainment for Cases 1, 2 and 4. Environmental air (above the bold line) mixes with cloud base air (below the bold line) to form the diluted part of the cloud (stippled area). The undiluted adiabatic core is cloud base air which penetrated deep inside the cloud. The upshear part of the cloud is to the left of the dashed line while the downshear is to the right. The arrows pointing to a box show the origin of the air which when mixed characterizes the air in the boxes. The air mixes in approximate proportion to the thickness of the arrows. The direction of the vertical motion is shown inside the boxes.

REFERENCES

- Baumgardner, Darrel, 1983: An analysis and comparison of five water droplet measuring instruments, *J. Climate. Appl. Meteor.*, **22**, 891-910.
- Baumgardner, Darrel, 1985: Personal communication.
- Betts, Alan K., 1982: Saturation point analysis of moist convective overturning, *J. Atmos. Sci.*, **39**, 1484-1505.
- Boatman, Joey F. and August H. Auer, Jr., 1983: The role of cloud top entrainment in cumulus clouds, *J. Atmos. Sci.*, **40**, 1517-1534.
- Bolton, David, 1980: The computation of equivalent potential temperature, *Mon. Wea. Rev.*, **108**, 1046-1053.
- Chameides, W. L. and D. D. Davis, 1982: The free radical chemistry of cloud droplets and its impact upon the composition of rain, *J. Geophys. Res.*, **87**, 4863-4877.
- Danielson, E. F., and V. A. Mohnen, 1977: Project Dustorm report: ozone transport, in situ measurements, and meteorological analyses of tropopause folding, *J. Geophys. Res.*, **82**, 5867-5877.
- Garland, J. A., A. W. Elzerman and S. A. Penkett, 1980: The mechanism for dry deposition of ozone to seawater surfaces, *J. Geophys. Res.*, **85**, 7488-7492.
- Greenhut, Gary K., 1986: Transport of ozone between boundary layer and cloud layer by cumulus clouds, *J. Geophys. Res.*, **91**, 8613-8622.
- Heymsfield, Andrew J., Peter N. Johnson and James E. Dye, 1978: Observations of moist adiabatic ascent in northeast Colorado cumulus congestus clouds, *J. Atmos. Sci.*, **35**, 1689-1703.

- Kawa, Stephan Randolph, 1985: Ozone deposition, scalar budgets and radiative heating over Texas coastal forest and ocean. M.S. Thesis, Atmospheric Science Paper No. 398, Colorado State University, Department of Atmospheric Science, Fort Collins, Colorado.
- LaMontagne, Robert G. and James W. Telford, 1983: Cloud top mixing in small cumuli, *J. Atmos. Sci.*, 40, 2148-2156.
- Lawson, R. Paul and Alfred R. Rodi, 1987: Airborne tests of sensor wetting in a reverse flow temperature probe, Sixth Symposium on Meteorological Observations and Instrumentations, January 12-16, 1987, New Orleans.
- Lenschow, D. H., J. C. Wyngaard, and W. T. Pennel, 1980: Mean-field and second-moment budgets in a baroclinic, convective boundary layer, *J. Atmos. Sci.*, 37, 1313-1326.
- Lenschow, D. H., R. Pearson, Jr., and B. B. Stankov, 1981: Estimating the ozone budget in the boundary layer by use of aircraft measurements of ozone eddy flux and mean concentration, *J. Geophys. Res.*, 86, 7291-7297.
- Maahs, Howard G., 1983: Kinetics and mechanism of the oxidation of S(IV) by ozone in aqueous solution with particular reference to SO₂ conversion in nonurban tropospheric clouds, *J. Geophys. Res.*, 88, 10,721-10,732.
- Matthews, R. D., R. F. Sawyer, R. W. Shefer, 1977: Interference in chemiluminescent measurements of NO and NO₂ emissions from combustion systems, *Environ. Sci. Technol.*, 11, 1092-1096.
- McClatchey, R. A., R. W. Fenn, S. E. A. Selby, F. E. Volz, and V. S. Garing, 1972: Optical properties of the atmosphere (Third edition). Environmental Research Papers No. 411, Air Force Cambridge Research Laboratories, Bedford, MA 108 pp.
- Paluch, I. R., 1979: The entrainment mechanism in Colorado cumuli, *J. Atmos. Sci.*, 36, 2467-2478.
- Pearson, R. Jr., and D. H. Stedman, 1980: Instrumentation for fast response ozone measurements from aircraft, *Atmos. Technol.*, 12, 51-55.

- Pearson, R. Jr., B. F. Weber, D. H. Lenschow, and B. B. Stankov, 1982: Ozone flux and mean concentration budget over short-grass prairie, Second Symposium Nonurban Troposphere, AMS/AGU/NASA, Williamsburg, Virginia, May 25-28. Reprint Volume published by the American Meteorological Society, Boston, Massachusetts.
- Rawson, A. E., 1953: Studies of ozonisation, 2, Solubility of ozone in water, *Water Eng.*, 57, 102-111.
- Rodi, A. R. and P. Spyers-Duran, 1972: Analysis of time response of airborne temperature sensors, *J. Appl. Meteor.*, 11, 554-556.
- Strapp, Walter Straap and Robert S. Schemenauer, 1982: Calibrations of Johnson-Williams liquid water content meters in a high-speed icing tunnel, *J. Appl. Meteor.*, 21, 98-108.
- Wesely, M. L., D. R. Cook and R. M. Williams, 1981: Field measurement of small ozone fluxes to snow, wet bare soil, and lake water, *Bound.-Layer Meteor.*, 20, 459-471.

Part II

ENTRAINMENT INSTABILITY AND VERTICAL MOTION AS
CAUSES OF STRATOCUMULUS BREAK UP

Chapter 1: INTRODUCTION

1.1 Problem

The alchemists of the middle ages sought a method to convert common substances into gold. With similar success, present-day cloud modelers are searching for a simple parameter to predict the breakup of marine stratocumulus. The desired parameter would use commonly measured quantities to determine the stratocumulus cloud coverage and would be useful for low-resolution models and forecasting. The approach has been to base the parameter on the thermodynamics of the interface between cloud and overlying air. All assume that the mechanism driving stratocumulus cloud breakup is cloud top cooling due to mixing and evaporation of cloud droplets. However, the mere fact that every few years a “new and improved” parameter appears leads one to believe that a satisfactory quantity has not yet been discovered.

1.2 Objective

The objective of this paper is to rigorously evaluate existing parameters by comparing values derived from aircraft measurements with photographs of clouds at the time of measurement and some time later. Because there is little association between the parameters and cloud breakup, a second mechanism based on large scale dynamics rather than thermodynamic stability is investigated.

Chapter 2: BACKGROUND

2.1 Physics of Entrainment Instability

Mixtures of unsaturated overlying air with the cloud air below may be positively or negatively buoyant, with respect to the cloud air, depending on the composition and the characteristics of the two air parcels. Figure 2.1 shows this buoyancy in terms of virtual potential temperature (θ_v) for three different pairs of air parcels as a function of the fraction of unsaturated overlying air in the mixture (χ). The characteristics of the three pairs of air parcels are detailed in Table 1.1. For all examples the overlying air is warmer than the cloud air reflecting a general tendency for the mixture to warm as the overlying air is added. However, evaporative cooling of cloud droplets will lessen the warming effect when χ is small.

Starting at the left-hand side of the plot (see magnified area) addition of the warmer unsaturated air to the pure cloud air evaporates the cloud droplets. For the solid and dashed examples this is strong enough to cool the mixture with respect to the pure cloud parcel, whereas the warm overlying air for the dotted example overwhelms the evaporative cooling. When there is no more liquid water and the mixture is barely saturated, the curve kinks; this is defined as χ' . Note how this point is at a greater χ for the dashed case compared with the solid case which has a smaller initial liquid water content (l). Further addition of overlying air warms the mixture. At the point where $\delta\theta_v$ becomes positive $\chi = \chi_{crit}$.

Figure 2.2 illustrates how the above process might lead to stratocumulus breakup, depending on the fraction of overlying air in the mixture (χ). If $\chi > \chi_{crit}$,

the mixture will be positively buoyant with respect to the cloud and breakup will not occur. However, if only a small amount of overlying air is entrained and $\chi < \chi_{crit}$, a negatively buoyant mixture may form as shown in Figure 2.1. The resulting buoyancy-driven turbulent kinetic energy (TKE) may entrain even more overlying air and the cycle is repeated. When $\chi < \chi_{crit}$ a feedback mechanism is possible leading to instability and breakup of the cloud.

2.2 Definition of Stratocumulus Stability Parameters

Stage and Businger (1981) developed the Δ_2 parameter which parameterizes entrainment instability discussed above. This theory is based on the earlier works of Randall (1980) and Deardorff (1980).

Consider a saturated cloud parcel just below the interface with the warm overlying air. In the cloud, the equation for the perturbation virtual potential temperature θ_v is

$$\theta'_v = \theta' + \bar{\theta}\epsilon q' - \bar{\theta}l'$$

where the prime denotes the perturbed part and the overbar the mean part from a Reynolds decomposition, θ is potential temperature, q is water vapor mixing ratio, l is liquid water mixing ratio, and $\epsilon = .622$. Assuming that the cloud parcel remains saturated, q' can be approximated as $\theta'(dq_s/dT)$ where dq_s/dT , the change of saturation mixing ratio with temperature, is a known function of temperature. Using the linearized form of equivalent potential temperature θ_e ,

$$\theta'_e = \theta' + \frac{L}{c_p}q',$$

where L is latent heat of vaporization and c_p is the heat capacity of dry air at constant pressure we get

$$\theta'_v = \beta\theta'_e - \bar{\theta}Q',$$

where perturbation total water is

$$Q' = q' + l'$$

and

$$\beta = \frac{1 + (1 + \varepsilon)(dq_s/dT)}{1 + (L/c_p)(dq_s/dT)}$$

The flux form of θ'_v is

$$\overline{\theta'_v w'} = \beta \overline{\theta'_e w'} - \bar{\theta} \overline{Q' w'}$$

Assuming that diabatic processes are negligible at cloud top so that θ_e is conserved, we can make use of the relationship between the entrainment velocity w_e and the flux of any conserved scalar S at cloud top

$$-w_e \Delta S = (\overline{w' S'})_{cloudtop} \quad (1)$$

Here and throughout this study Δ denotes the the overlying air value minus that of the cloud air. Finally, we get

$$\begin{aligned} \overline{\theta'_v w'} & eq \quad -(\beta \Delta \theta_e - \bar{\theta} \Delta Q) w_e \\ & eq \quad -\Delta_2 w_e \end{aligned}$$

where Δ_2 is defined as

$$\Delta_2 = \beta \Delta \theta_e - \bar{\theta} \Delta Q.$$

The sign of Δ_2 should predict cloud break up. Since w_e is always positive, a positive Δ_2 means that there is negative buoyancy flux at the cloud top. In other words, when warmer (colder) than average air is brought down (up) TKE is converted to potential energy (PE). This process is non-spontaneous and therefore work, which is derived from TKE, must be done on the cloud. Because there is a limited amount of TKE the entrainment is controlled. On the other hand, if Δ_2 is negative PE will be converted to TKE, which is a spontaneous process. There will be no control on the entrainment and the cloud will dissipate. This assumes that $\chi < \chi_{crit}$ for the cloud parcel (i.e. the mixture).

The X parameter developed by Randall (1984) is an extension of Δ_2 and accounts for cloud deepening through entrainment which comes into play for deep boundary layers. Apparently, the effect of entraining warm air which may cause

cloud breakup is offset by increasing liquid water content. As the boundary layer deepens, the temperature at cloud top will decrease moist adiabatically causing condensation. In the derivation of X the sign of the time change of liquid water rather than the flux of buoyancy is the criteria for instability, but all the physics of Δ_2 discussed above is included.

The Δ_m parameter of Nicholls et al. (1985) builds on the theory of the above two parameters. It accounts for density fluctuations, due to evaporation, generated by mixtures with all values of χ and not just saturated mixtures. They reason that because all values of χ are observed in the layer between the cloud and the overlying air, all mixtures should be equally important in determining the interfacial stability. Hence, Δ_m is proportional to the area under the particular curve in Figure 2.1.

$$\Delta_m = 2 \int_0^1 \delta\theta_v d\chi.$$

The quantity associated with cloud break up is Δ_m normalized by $\Delta\theta_v$. The result is that $\Delta_m/\Delta\theta_v$ is related to the area of a triangle at points $\chi = 0, \chi = \chi'$ and $\chi = 1$ for a given curve in Figure 2.1 and is related to the net cooling due to evaporation of liquid water over all values of χ . This quantity has no criteria for cloud break up, as does Δ_2 , except that lower values should be associated with dissipating clouds and higher values with solid cases.

2.3 Evaluation of Parameters from Real Data

Previous studies have tested the association of various parameters with cloud break up. Hanson (1984) categorized the observed stratocumulus clouds from EPOCS-1981 as “solid”; “broken”, (meaning homogeneous cloud with holes through which the ocean was visible); or “patchy”, (meaning clouds separated by large clear areas). He compared these descriptions with Δ_2 values determined from appropriate soundings. His conclusion was that in general large positive values of Δ_2 occur for solid clouds and large negative values for broken clouds but that many

anomalous cases exist (i.e. $\Delta_2 > 0$ for broken and $\Delta_2 < 0$ for solid clouds). Thus, Δ_2 may not be an adequate criterion for cloud breakup.

To test the effectiveness of their new parameter, $\Delta_m/\Delta\theta_v$, Nicholls et al. (1985) calculated its value along with Δ_2 from aircraft data sampled from five stratiform clouds over United Kingdom coastal waters. Instead of comparing the parameters with cloud observations, they used measured entrainment velocities normalized by the mixed layer convective velocity scale, w_e/w^* . The entrainment velocity was derived from observed fluxes of total water. For these five cases, along with one other, Δ_2 is poorly correlated with $-w_e/w^*$. The $\Delta_m/\Delta\theta_v$ correlation is much better.

Although comparison of the parameters with cloud observations is a more direct evaluation than comparison with normalized entrainment velocities, there are drawbacks. Cloud observations must be made over an extended period of time to determine changes in cover and the results are subjective. On the other hand, evaluation with normalized entrainment velocities also has problems. This is because the entrainment velocities usually use ΔQ or $\Delta\theta_e$ in their derivations which are also quantities used to calculate the parameters, especially Δ_2 . Any observed correlation or lack of correlation may be partly due to this mathematical dependency rather than physical processes. Furthermore, it is difficult to obtain reliable measurements of q and l in cloud. This problem can be circumvented by using ozone mixing ratios to calculate entrainment rates. In addition, ozone has the advantage of being conserved while θ is subject to diabatic processes and Q must be corrected for drizzle flux.

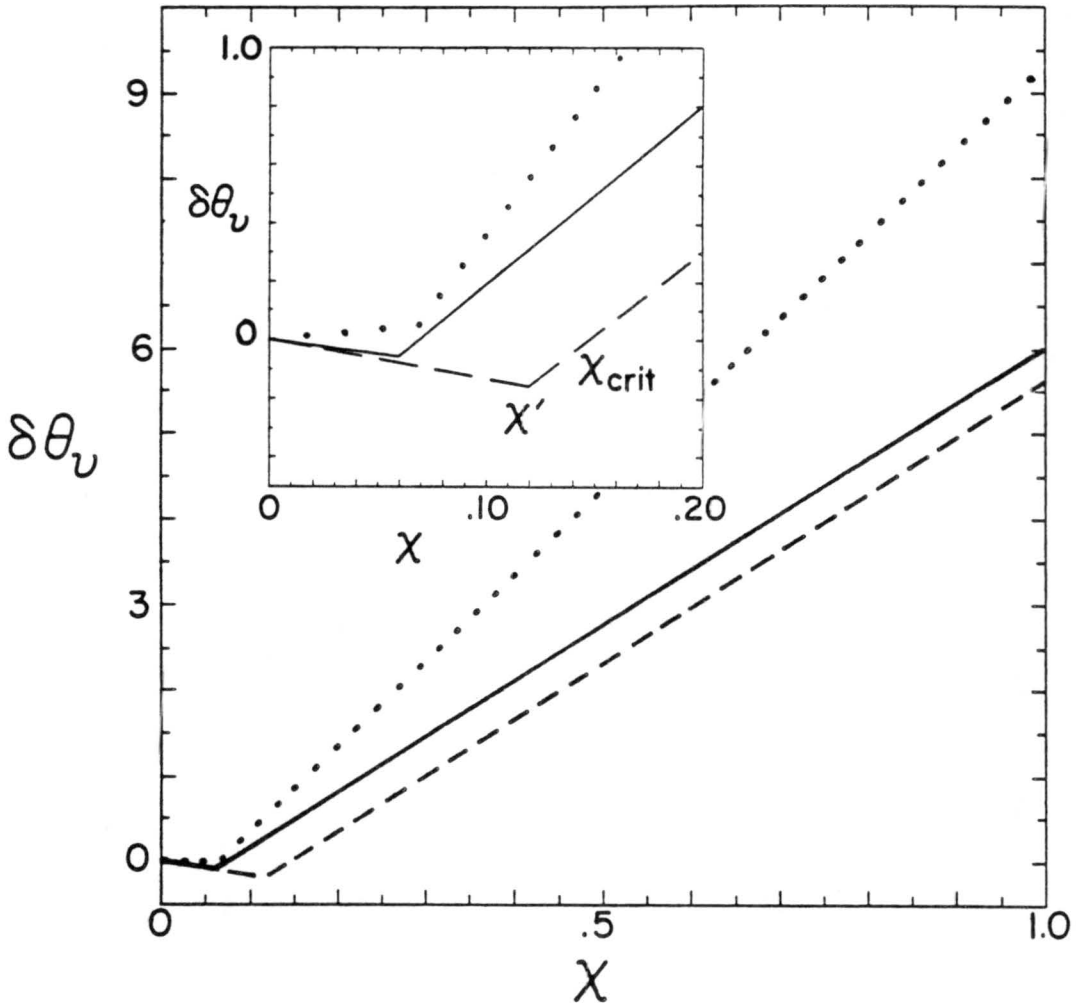


Figure 2.1. Three examples of buoyancy of cloud air and overlying air mixtures as a function of the fraction of overlying air in the mixture (χ). The buoyancy is with respect to pure cloud air at $\chi=0$ and is in terms of $\delta\theta_v(\chi)$ defined as $\theta_v(\chi) - \theta_v(0)$. All three examples use the same values of liquid water potential temperature ($\theta_l = 289$ K) and total water mixing ratio ($Q = 9.0$ g kg $^{-1}$) for the cloud air. Values for the jump across the mixing interface are shown in Table 2.1. Given values of θ_l and Q for the cloud and overlying air, values for any mixture are easily obtained because both are conserved and mix linearly (i.e. $\theta_l(\chi) = \theta_l^{\text{overlying}}(\chi) + \theta_l^{\text{cloud}}(1 - \chi)$). With θ_l and Q of the mixture $\delta\theta_v$ can be calculated. For all examples χ' is defined where there is a kink in the curve. For the solid and dashed examples $\chi = \chi_{\text{crit}}$ is defined as nonzero χ where $\delta\theta_v = 0$.

Table 2.1. Quantities associated with each buoyancy curve shown in Figure 2.1. Jumps of θ_l and Q across the mixing interface between cloud and overlying air ($\Delta\theta_l = \theta_l^{\text{overlying}} - \theta_l^{\text{cloud}}$), cloud liquid water before mixing, l and two parameters discussed later in section 6.4 are shown.

line	$\Delta\theta_l$ (K)	ΔQ (g kg ⁻¹)	l (g kg ⁻¹)	Δ_2	$\Delta_m/\Delta\theta_v$
-	6.5	-5.0	0.20	-1.70	0.96
--	6.5	-5.0	0.40	-1.72	0.89
...	10.0	-5.0	0.30	+0.06	0.97

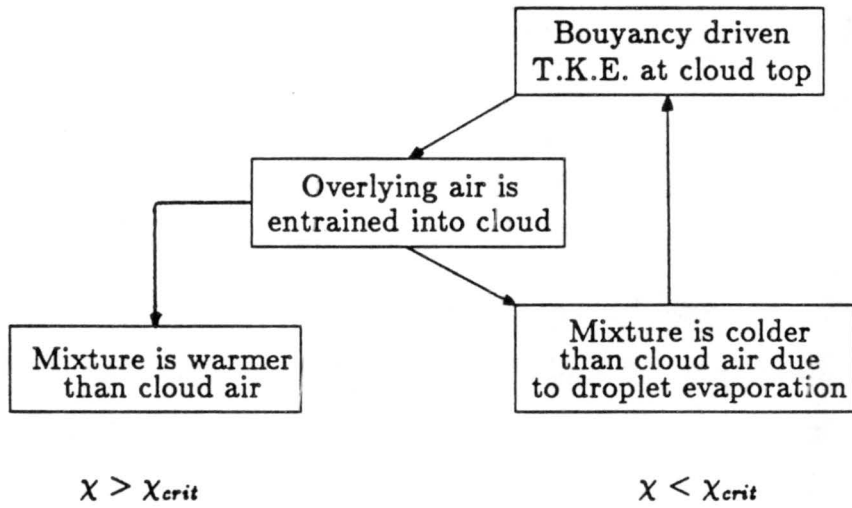


Figure 2.2. Diagram depicting a possible mechanism of cloud destruction by entrainment. See text.

Chapter 3: EVALUATION OF ENTRAINMENT INSTABILITY

3.1 Description of DYCOMS

During July and August 1985 the NCAR Electra sampled the stratocumulus clouds off the California coast for the Dynamics and Chemistry of Marine Stratocumulus (DYCOMS) experiment. The aircraft was equipped to measure air motion perturbations, moisture, temperature and ozone; further details are given in Appendix A. It sampled the uppermost part of the cloud as well as the overlying air on all but one of the ten flights. The combination of this data with simultaneous aircraft and satellite photographs of the clouds makes this an excellent source of information about cloud top instability. For each flight, the aircraft sampled the interface between the cloud and the overlying air during soundings and horizontal legs. The stability parameters derived from this data can be compared with the photographs.

3.2 Determination of Cloud Thermodynamic Stability

To determine the stability we need to know the origin of the air entrained into the mixed layer. Mixing line analysis can help us with this problem by determining the possible mixing histories for a parcel of air. Although this type of analysis cannot tell us all the details, it can often be used to support or reject hypotheses. Consider two different parcels of air each with a different value of scalars X and Y . Figure 2.3 shows the points representing these two parcels as A and B . Assuming there is no production or destruction of X or Y , the \times points represent possible mixtures of A and B . The ratio of $A:B$ in the mixture is equal to the ratio of the

length of the point from B to the length of the point from A. Point D cannot be solely a mixture of A and B but rather must include some air from parcel C. Local destruction of X at parcel A (e.g. diabatic cooling if X is θ_l) will shift A to A'. The mixture points will be co-linear (shown by +) if the production time scale is slower than the mixing time scale. However, if both time scales are comparable the points will lie on a curve as shown by the \circ points. With this in mind we will later see that insights in the mixing process are possible using this approach.

To do this analysis, a set of independent quantities which are conserved on the time scale of the mixing processes are needed. The three chosen are θ_l , which is strongly temperature dependent; Q , which is moisture dependent, and ozone mixing ratio, O_3 , which is independent of both. Equivalent potential temperature, θ_e , is not chosen for two reasons. One is that both θ_e and Q are linearly dependent on q . When they are plotted against each other, the points tend to fall on a line making it difficult to separate physical processes from mathematical dependence. The second reason is that θ_l uses fewer assumptions in its evaluation. The saturation assumption is never invoked and in cloud-free conditions θ_l and Q do not both depend on q . Ozone is a useful quantity because it is independent of θ_l , its slight dependence on q can be removed and it is not subject to the diabatic effects that may affect θ_l . Part I Section 3.3 details these two problems as well as the advantages of using ozone.

3.2.1 Soundings

To obtain the vertical structure of cloud we first consider aircraft soundings at constant heading. High resolution profiles of θ_l , Q , O_3 , Δ_2 , θ_e and l from the cloud-overlying air interface sampled on two different days are shown in Figure 2.4 and 2.5. For both cases all quantities except for l are well mixed from the cloud top (point A) down to the ocean surface and all show a jump across the top of the mixed layer. These two cases have been chosen because, as we will see, $\Delta_2 < 0$ for Figure 2.4 and $\Delta_2 > 0$ for Figure 2.5.

To find the appropriate jumps for the determination of Δ_2 we employ mixing line analysis. Figures 2.6a and 2.6b show diagrams of (θ_1, O_3) and (Q, O_3) from the cloud-overlying air interfaces shown in Figure 2.4 and 2.5. The 20 Hz sample rate of the soundings has been reduced to 4 Hz for the mixing line diagrams and is plotted by the mean of five values. Each point is labeled according to the standard deviation of vertical velocity, σ_w , of those five points.

These diagrams as well as those from all flights of this project showed the same basic mixing features. Cloud air labeled point A (see Figure 2.4a, 2.5a and 2.6) mixes with overlying air, point C, to form the Entrainment Interface Layer (EIL). Roach et al. (1982) define this as the layer containing the temperature jump across mixing interface. An example of a mixture in this layer is point B. Starting in the cloud layer, point A, the mixing is rapid as indicated by the high values of σ_w (note the low numerical labels) but as point C is approached the turbulence dampens. We can interpret this according to the intermittent entrainment episodes observed by Caughey et al. (1982). During a past entrainment episode turbulent mixing between point A and C formed the points along a line \overline{AC} . Since that mixing occurred the turbulence has dampened; moreover, production of O_3 or diabatic processes have been negligible, otherwise the points would not be linear. Above point C, σ_w decreases further and it is likely that these points have never mixed with the cloud.

Other conclusions can be gleaned from the diagrams. Both EIL mixing lines from Flight 5 and 9 are continuous meaning that the resulting mixtures have values of χ from 0 to 1. This is not always the case. Figure 2.6c show diagrams from a Flight 10 sounding with a non-continuous mixing line. Apparently, here and in several other observed soundings there is a sharp discontinuity across the EIL where there was no mixing at the location of sampling.

Another feature of some of the mixing diagrams is the tendency for the (O_3, θ_1) points from the EIL mixing line to be slightly curved compared with the straighter (O_3, Q) set of points. Figure 2.6d has many of the (O_3, θ_1) points off the A to C

line extending toward the lower right-hand corner of the plot. This is probably not due to instrument response as ascent soundings do not show a curved EIL toward the upper left-hand corner. Instead, this may be due to diabatic effects. These observations about the mixing processes are addressed again in Section 4.3.

Regardless of whether Δ_2 , X or $\Delta_m/\Delta\theta_v$ is used to estimate stability, jumps in the thermodynamic quantities across the EIL are needed. Determination of the in-cloud value for the jump is straightforward. Averaged values from the top 50 m of the cloud are used. Obtaining the value for the overlying air is not as easy. Mixing line analysis suggests that point C is a likely choice. Although turbulence here may be less vigorous than at point A, the co-linear nature of EIL points indicates that point C air is being entrained.

Figures 2.4b and 2.5b show the profile of Δ_2 values derived using a constant in-cloud value and an overlying value taken from the plotted height. As mentioned above, these cases were chosen so that at point C $\Delta_2 < 0$ for Figure 2.4, therefore unstable according to entrainment instability theory. Figure 2.5 was chosen as a stable case ($\Delta_2 > 0$).

Sometimes, profiles where $\Delta_2 < 0$ at point C, the top of the EIL, may have $\Delta_2 > 0$ when a deeper jump is considered. One might argue that this stable air will eventually be entrained into the cloud. But by this time diabatic processes such as long wave radiative divergence may cool the air rendering it unstable. Therefore, it is not advisable to determine the jump simply by inspection of the soundings.

Table 2.2 shows important characteristics of all the other soundings from the DYCOMS project. Jumps and derived stability parameters are determined using mixing line analysis. Other stability parameters X and $\Delta_m/\Delta\theta_v$ are shown in Table 2.2. Both are evaluated in the same spirit as Δ_2 using mixing line analysis to determine the value to be used for overlying air. The formula used to calculate X is from Randall (1984).

3.2.2 Horizontal Legs

A second method of obtaining the vertical structure of the cloud is to consider the horizontal legs at cloud top. Here the plane skipped in and out of cloud for 25 to 50 km and provided multiple samples of the EIL. With this approach we can address the problem of horizontal inhomogeneities of the overlying air. The soundings sample the EIL only once and do not provide this opportunity.

Figure 2.7 shows an example of a cloud top time series. Notice how all the instruments used to derive these results responded well to the very sharp changes in temperature, moisture, liquid water and ozone as the aircraft flew in and out of the cloud turrets. This is a virtue of having at least a 5 Hz bandwidth which results in a 20 m resolution at the aircraft speed.

Figure 2.8 shows a mixing line analysis of the horizontal leg from Figure 2.7. It presents two problems not seen in the soundings. Of course the basic mixing process is the same: cloud and overlying air sources (labeled A and C, respectively) mix to form the EIL. However, horizontal inhomogeneities in the overlying air and the fact that the aircraft does not always reach the top of the EIL, when it makes an excursion out of cloud, present difficulties. For this segment the maximum jump occurs at 13.5 minutes after the hour ($\theta_1=298$). Here the aircraft remains out of cloud for about 3 km in the horizontal and likely gets close to the EIL top. Points above are probably not sampled because the points in Figure 2.7 fall along a single line (not shown) suggesting all points are within the EIL. At 15.4 minutes out- of-cloud air is again sampled. Although this may be considered a second jump distinct from the first, the entrained air is similar for both as points from both jumps lie on the same mixing line. The fact that there is one point C and therefore one mixing line means that the overlying air is probably homogeneous in the thermodynamic quantities and that the aircraft simply did not get to the top of the EIL during the second jump. Other legs show indications of horizontal inhomogeneities, usually in O_3 , when there are several point C's on a mixing

diagram and the points fall along several mixing lines. Here the two jumps from the two most pronounced mixing lines are used.

Derived Δ_2 values are shown in Figure 2.7. The in-cloud values used in the jump were simply the average of in-cloud points while the overlying values are from the plotted points. Thus, as with the soundings, Δ_2 for the in-cloud points should be close to zero. The out of cloud points having the lowest water vapor content and highest temperature are close to point C on the mixing line analysis plots. For these points Δ_2 is a measure of the stability; those overlying air points with a more positive Δ_2 are within the EIL but probably not from the EIL top.

Table 2.3 shows important quantities from all the cloud top legs. When a second jump in addition to the maximum is observed, derived values from both are shown. All but two cases have the EIL points on a single (θ_l, Q) mixing line which suggests horizontal homogeneity for these two quantities. As a result, when it seems appropriate to show two jumps for a given case, the magnitudes of Δ_2 will differ but the sign will usually be the same. This should not be of concern because it is the sign of Δ_2 rather than the magnitude which ultimately determines the direction of the buoyancy flux.

3.3 Comparison of Δ_2 with Photographs

Quantifying the degree of brokenness for a stratocumulus cloud field is a subjective and therefore difficult task. Instead, we discuss the structure of the stratocumulus cloud for each flight as derived from photographs in relation to the stability parameters. The satellite pictures from the visible spectrum were obtained from the GOES West satellite by Shih (1987) who prepared them in a presentable format. The resolution for these pictures is 2 km. The aircraft photographs are from two 16 mm time lapse color cameras placed on the right and left hand sides of the aircraft. The photographs were taken every 10 seconds and a continuous record is available. Unfortunately, they reproduce poorly and are not shown.

Flight 5 (August 9) is very unstable judging from the sign of Δ_2 for the soundings as well as the horizontal legs. Figure 2.9 shows a satellite photograph at the time of the first sounding 1103 PDT (a) and at 1633 PDT (b). The line is the location of the cloud top leg shown in Figure 2.7 and the dots are the locations of the three soundings. According to these photographs the cloud appears to be getting thicker not breaking up as the stability parameter would predict.

The aircraft photographs also show no sign of breakup; however, it is sometimes difficult to reconcile the aircraft and satellite pictures. For example, the aircraft pictures just prior to the sounding labeled A on Figure 2.9a do not show the broken structure as seen from the satellite. Instead there is only a faint lead in the cloud deck. The seeming lack of agreement between satellite pictures with broken clouds and aircraft pictures, showing only faint holes and splits in the cloud deck, is seen in the other cases. It is partly a result of the low viewing angle from the aircraft which enables the viewer only to see small holes close to the aircraft. Those far away are not apparent, especially if the deck is thick. In addition, the size of the dark holes on Figure 2.9a may be near the resolution of the satellite camera and may be indicating thinner areas rather than large cloud free areas. This would tend to agree with the aircraft pictures. Regardless of the interpretation, there is no sign of dissipation within several hours of the negative Δ_2 measurements. In addition satellite photos for the following two days (not shown) show an unbroken persistent stratocumulus deck although by this time the sampled clouds have probably been advected to the south.

Flight 4 (August 7) sampled air that was definitely unstable and similar to Flight 5 in this respect. Two of the soundings have $\Delta_2 < -2.0$ and the cloud top legs had significant portions with $\Delta_2 < -3.0$. Figure 2.10 shows a satellite photograph at 1303 PDT (a) and at 1603 PDT (b) again with soundings and cloud top legs shown. During the three hour period the clouds are becoming more pronounced despite the negative Δ_2 values. Aircraft photographs just prior to the soundings labeled B and C show faint leads in the deck. There is little sign

of dissipation, even though the Δ_2 remains negative. However, by 0600 PDT the following day the flight area is clear.

Flight 2 (August 2) is one of the more stable flights according to entrainment instability theory with several instances of positive Δ_2 measurements. The 1503 PDT satellite photograph, shown in Figure 2.11a, and the simultaneous aircraft photo (not shown) show solid clouds. None of the aircraft photos for this day had holes or leads in the cloud deck which are seen in other flights, especially Flights 4 and 5. Thus, the solid appearance of the cloud from both cloud and aircraft generally agree with the measured Δ_2 values. The satellite photos for the two following days also show solid clouds in the research area .

Flight 10 (August 21) sampled the most stable air at the cloud-overlying interface of the project. This was observed in the morning hours during the cloud-top legs. The soundings however are all unstable. Satellite photos (not shown) during the flight show solid clouds but later images show signs of dissipation some three hours after the flight. The change in cloud appearance is small enough that this could be due to a difference in photographic processing technique.

Flight 3 (August 4) sampled the edge of a dissipating stratocumulus cloud deck and shows several instances where the measured Δ_2 values are associated with cloud breakup. Figure 2.11b shows a satellite photograph at 1303 PDT with sounding and cloud top locations. At 1052 PDT the first sounding yielded a value $\Delta_2 = -1.8$. By 1303 PDT the sounding location (point A) is almost cloud free and several hours later all clouds in this area have disappeared. Another instance is the first cloud-top leg flown about 30 minutes prior to the photograph shown (L-1). The westerly flight direction means that the plane is encountering solid cloud at the beginning with gradual thinning at the legs end. Note how Δ_2 values agree having almost stable values at the beginning and unstable values in the region of dissipation.

3.4 Evaluation of Parameters

There is an underlying trend in the data where flights with frequent sightings of holes and splits in the cloud deck sample the lowest Δ_2 values (e.g. Flight 4 and 5) and flights with solid cloud sample the highest Δ_2 values (Flight 2).

However, Δ_2 values do not predict the breakup of the clouds. Often when a negative Δ_2 value is measured the cloud shows no sign of dissipation after several hours and sometimes after several days. One might expect Flight 5 with its very negative Δ_2 values to break up rapidly, but as shown by the satellite pictures the clouds remain solid for two days, then suddenly disappear. The parameter X also shows cases with very negative values which do not breakup, e. g. Flights 1,4 and 5.

We can evaluate Δ_2 and X because both have a critical value below which the cloud should breakup and we have observations above and below this value. Without having the critical value for Δ_m/θ_v and having no example of a dissipating cloud simultaneous with Δ_m/θ_v measurements, it is difficult to assess whether Δ_m/θ_v is associated with cloud breakup. It is possible that the critical value is below all values measured in this study and that all our cases were stable; this would explain why we observed no breakup. We need a measurement during breakup to adequately test this parameter. With the present data we can only discuss Δ_m/θ_v in comparison with Δ_2 .

The Δ_m/θ_v parameter might be expected to be an improvement over Δ_2 because it accounts for the unsaturated mixtures which contribute to the interfacial stability. However, Δ_2 can also account for fluctuations in density due to all mixtures regardless of saturation if we only use the sign of Δ_2 to predict cloud breakup. Consider the equation for Δ_2 in terms of θ_l rather than θ_e

$$\Delta_2 = \beta \Delta \theta_l + \left(\frac{L}{c_p} \beta - \theta \right) \Delta Q$$

where an approximate formula $\theta_e = \theta_l + \frac{L}{c_p}Q$ is used. Rearranging we get

$$\Delta_2 \frac{K_1}{\Delta\theta_l} = \beta K_1 + \frac{\Delta Q}{\Delta\theta_l}$$

where

$$K_1 = 1 / \left(\frac{L}{c_p} \beta - \theta \right)$$

and $\beta K_1 = 5.2 \times 10^{-4} \text{K}^{-1}$. Here we assume $\theta = 290 \text{ K}$. Now $K_1/\Delta\theta_l$ is always > 0 so the slope of the (θ_l, Q) mixing line $b (-\Delta Q/\Delta\theta_l)$ can be used to determine the sign of Δ_2 . If $b > \beta K_1$ then $\Delta_2 > 0$ and if $b < \beta K_1$ then $\Delta_2 < 0$. This approach was used to verify the sign of Δ_2 throughout this study. Recall that for a horizontal run several values of Δ_2 were recorded in Table 2.2 and that Figure 2.6 shows a range of Δ_2 values. The Δ_2 value with the largest magnitude is associated with the overlying air. All other values use a mixture in the EIL as the overlying value. The value for any mixture in the EIL will range from the overlying air value to zero but the sign will always be the same. This agrees with Equation 1 which states that the sign of the buoyancy flux is determined by Δ_2 and that w_e only influences the magnitude.

Although Δ_2 can tell us whether negatively buoyant mixtures will form in the EIL, it cannot account for l in the cloud layer. Liquid water content plays an important role in determining the intensity of the entrainment. Recall that Figure 2.1 showed a solid and dashed buoyancy curve, the latter having a greater value of l . The potential for evaporative cooling is greater for the dashed curve because negatively buoyant mixtures are more probable and therefore will occur more often. The mixtures will also result in stronger downward motions because $\delta\theta_v$ is less. The virtue of Δ_m/θ_v is that it accounts for this potential for greater evaporative cooling due to l . The Δ_2 values do not account for this as they are the same for both curves. But Δ_m/θ_v is not sufficient because it does not tell whether negatively buoyant mixtures are possible. As an example, note that the dotted curve and the solid curve in Figure 2.1 have almost the same Δ_m/θ_v value, yet all mixtures of the former curve are positive. One might argue that Δ_m/θ_v is

not likely to be of any use because there is no association between cloud breakup and the sign of Δ_2 .

Recent numerical experiments also question entrainment instability theory. Kuo (1987) tests this theory with his dynamical stratocumulus model. The initial conditions for one example was a cloud topped mixed layer with $\Delta\theta_e = -7$ K across the cloud-overlying air interface. Upon introducing a cold anomaly of 1 K about 500 m wide at cloud top, a 200 m hole in the cloud deck formed after about 10 minutes. This was expected from entrainment instability theory. However, some 10 minutes later the deck reformed. This may explain the holes sighted in Flights 5 and 4 which do not seem to grow and destroy the deck but instead may form only to be filled in later as happened in the model. In this case the introduction of unstable air into the cloud deck did not lead to breakup.

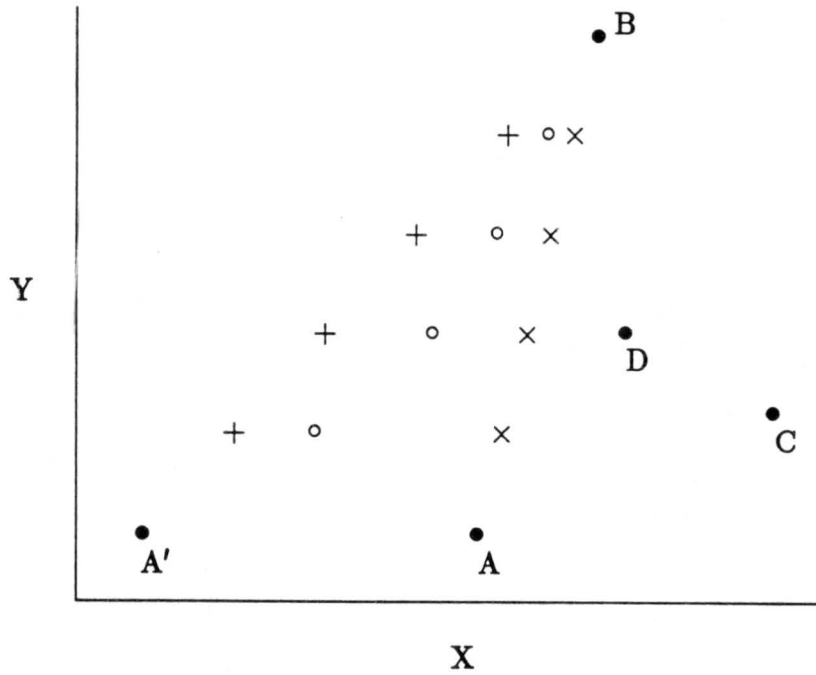


Figure 2.3. Illustration of processes which might effect a mixing diagram. Parcels of air labeled A, B, C, and D are shown having values of scalar X and Y. See text.

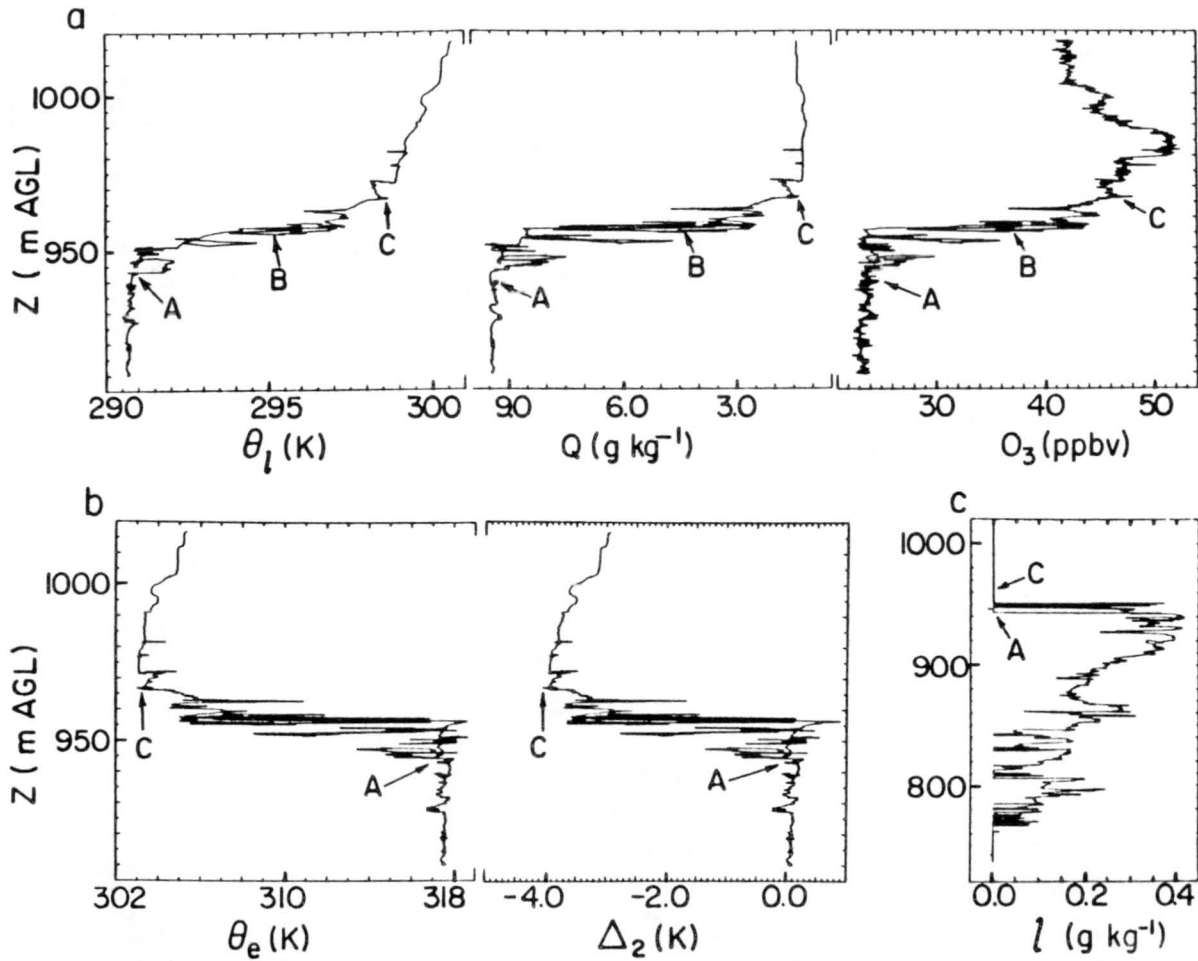


Figure 2.4. High resolution vertical profiles of θ_l , Q , O_3 (a); θ_e , Δ_2 (b), and l (c) vs. height for a cloud-overlying air interface. Data were obtained from 152920 to 153145 PDT 9 August 1985 during Flight 5.

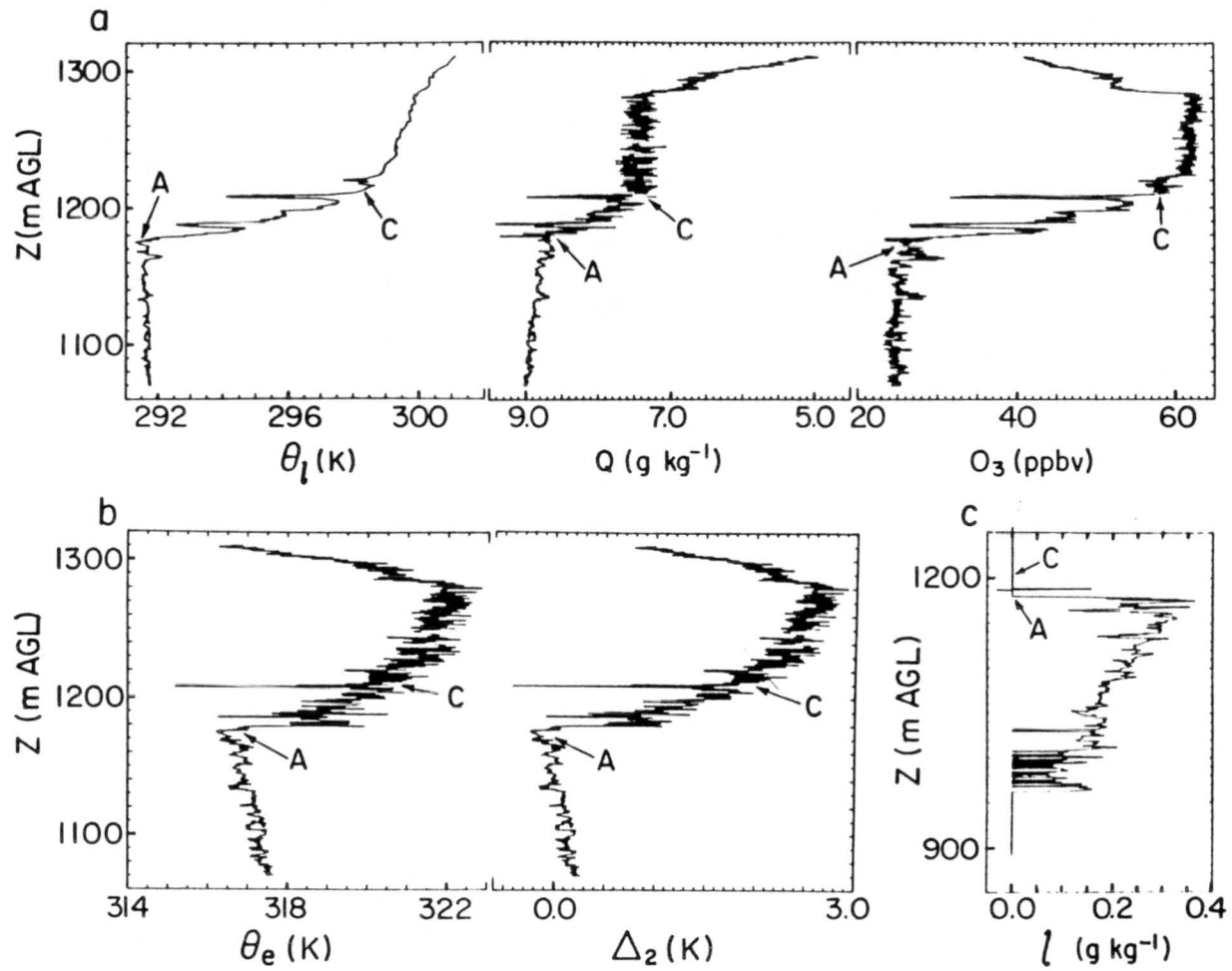


Figure 2.5. Same as Figure 2.4 except for data obtained from 151850 to 152150 PDT 19 August 1985 during Flight 9.

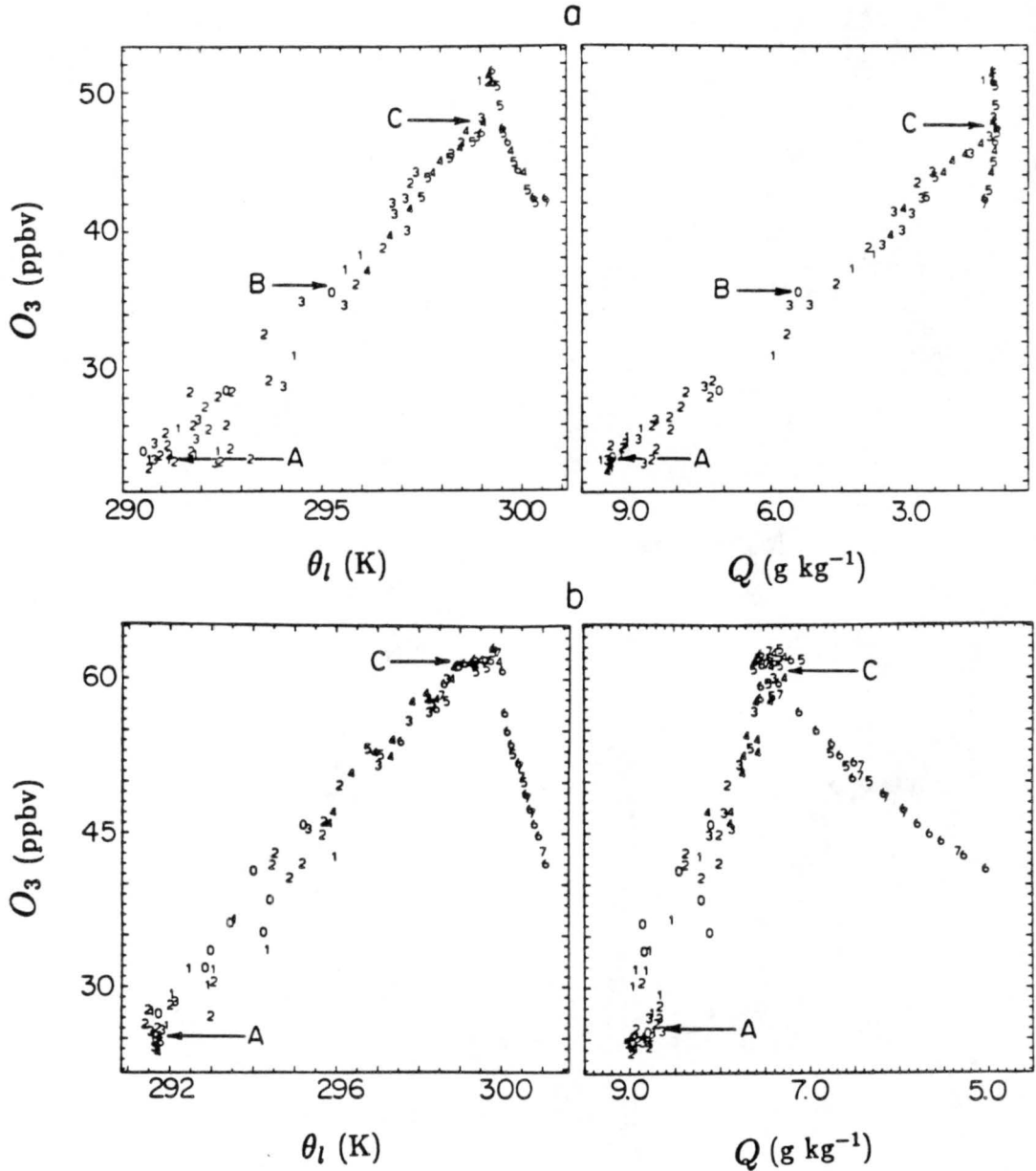


Figure 2.6. Mixing line analysis of (θ_l, O_3) and (Q, O_3) using data from the cloud-overlying air interface shown in Figure 2.4 (a), from the interface shown in Figure 2.5 (b), from the interface of the 091655 to 092000 PDT vertical profile of 21 August, Flight 10 (c), and from the 121640 to 122030 PDT vertical profile of 30 July, Flight 1 (d). Each point represents a mean of 5 values collected at 20 Hz. The points are labeled according to σ_w of those points as follows:

Label	σ_w (m s ⁻¹)	Label	σ_w (m s ⁻¹)
0	> 0.300	5	0.013 – 0.025
1	0.200 – 0.300	6	0.006 – 0.013
2	0.100 – 0.200	7	0.003 – 0.006
3	0.050 – 0.100	8	< 0.003
4	0.025 – 0.050		

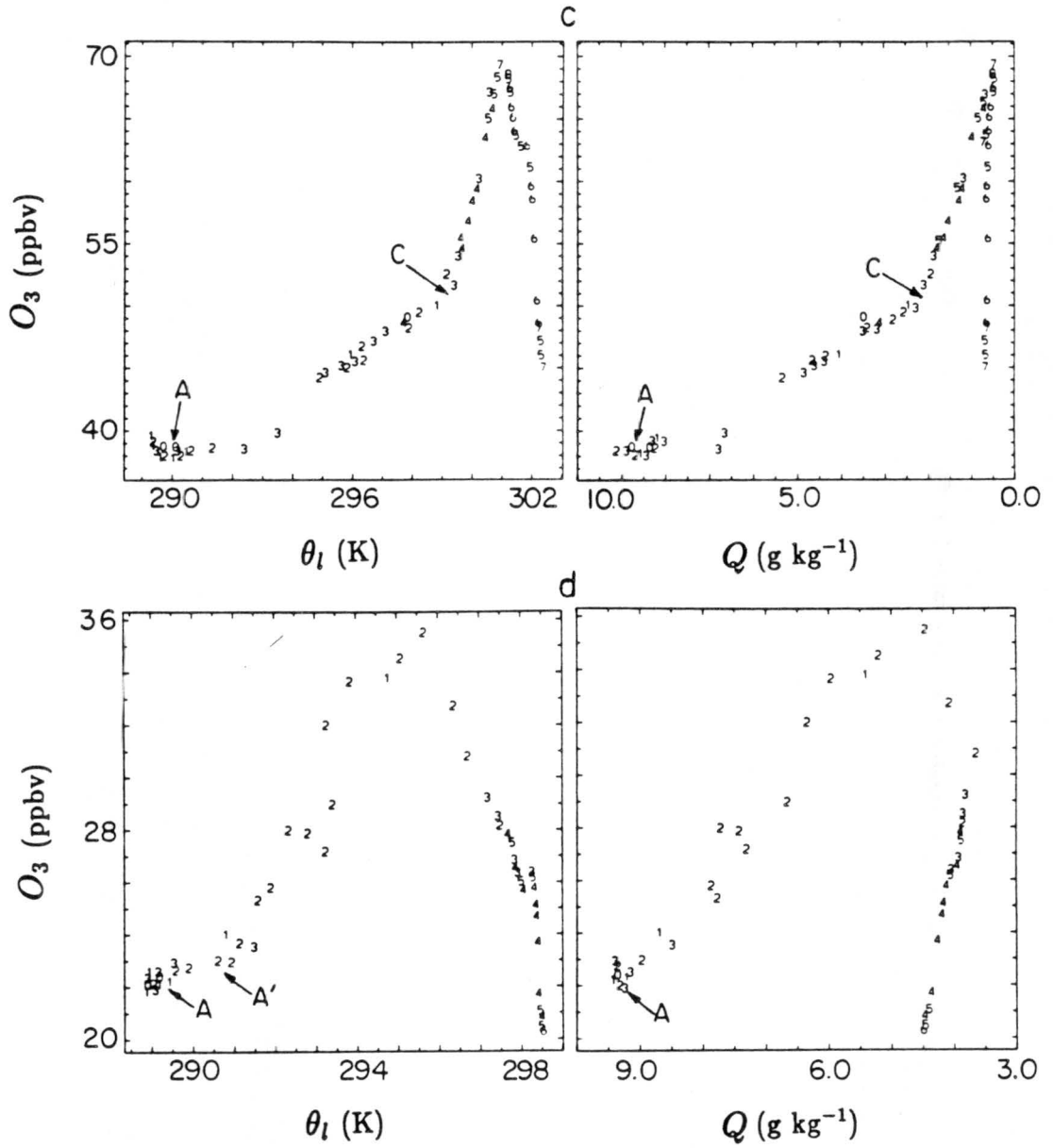


Figure 2.6. Continued

Table 2.2. Characteristics of the EIL from all DYCOMS vertical profiles. Listed are jumps across the cloud-overlying air interface for O_3 , θ_l , Q , and θ_e . Stability parameters Δ_2 , $\Delta_m/\Delta\theta_v$ and X are also shown. The average liquid water in the top 50 m of cloud is denoted \bar{l}_{50} .

FLIGHT	PROFILE	DATE	TIME (PDT)	z_i (m)	ΔZ_{EIL} (m)	ΔO_3 (ppbv)	$\Delta \theta_l$ (K)	ΔQ (g kg ⁻¹)	$\Delta \theta_e$ (K)	Δ_2 (K)	$\Delta_m/\Delta\theta_v$	X	\bar{l}_{50} (g kg ⁻¹)
1		7-30	12 16 40 12 20 30	765	10	+14	+7.5	-5.9	-7.2	-1.9	.77	-16	.35
1		7-30	14 36 00 14 40 30	750	22	+29	+9.0	-5.3	-4.2	-0.6	.92	-15	.36
1		7-30	16 26 30 16 28 00	685	30	+5	+7.7	-5.0	-4.8	-0.9	.95	-14	.22
2	A	8-2	10 21 50 10 24 30	710	40	+13	+7.5	-3.5	-1.2	+0.4	.92	-14	.30
2	B	8-2	13 00 30 13 06 00	760	32	+19	+8.5	-3.1	+0.8	+1.3	.88	-10	.41
3	A	8-4	10 52 20 10 54 30	540	32	+28	+11	-7.5	-7.7	-1.8	.91	-28	.22
3	B	8-4	13 37 10 13 44 00	615	11	+47	+5.5	-2.9	-1.7	-0.0	.87	-7	.30
3	C	8-4	15 33 50 15 35 50	544	30	+14	+4.6	-3.7	-4.6	-1.2	.92	-9	.10
3	D	8-4	15 44 40 15 46 05	592	27	+30	+5.5	-3.8	-4.0	-0.9	.97	-10	.10
4	A	8-7	11 10 00 11 14 00	840	60	+27	+8.2	-5.0	-4.3	-0.7	.91	-16	.65

FLIGHT	PROFILE	DATE	TIME (PDT)	z_i (m)	ΔZ_{EIL} (m)	ΔO_3 (ppbv)	$\Delta \theta_1$ (K)	ΔQ (g kg ⁻¹)	$\Delta \theta_e$ (K)	Δ_2 (K)	$\Delta_m/\Delta \theta_e$	X	\bar{i}_{50} (g kg ⁻¹)
4	B	8-7	13 52 00 13 54 20	870	50	+42	+9.0	-8.5	-12.2	-3.6	.91	-23	.30
4	C	8-7	15 41 30 15 44 55	908	12	+44	+8.0	-9.3	-15.2	-2.0	.92	-10	.35
4	D	8-7	15 51 30 15 55 30	850	33	+20	+6.8	-5.0	-5.7	-0.9	.93	-11	.31
5	A	8-9	10 56 15 10 59 30	870	28	+20	+10.2	-7.7	-9.0	-2.3	.91	-23	.45
5	B	8-9	13 38 05 13 40 25	900	18	+17	+7.6	-7.5	-11.1	-3.4	.93	-19	.35
5	C	8-9	15 29 20 15 31 45	945	20	+23	+8.5	-8.2	-11.9	-3.6	.89	-20	.30
5	D	8-9	15 41 40 15 44 00	950	17	+33	+8.0	-5.5	-5.7	-1.25	.92	0	.30
6		8-13	12 16 10 12 21 20	985	65	+4	+9.5	-6.2	-5.9	-1.2	1.0	-18	.17
7		8-16	14 20 20 14 24 00	1440	27	+20	+11.2	-7.0	-6.2	-1.6	.93	-14	.63
9		8-19	13 04 10 13 17 30	1210	15	+7	+5.0	-3.7	-4.2	-1.0	.95	+4	.23
9		8-19	14 13 10 14 16 00	1435	17	+20	+6.3	-4.8	-5.7	-1.4	.90	-1	.22
9		8-19	15 18 50 15 21 50	1176	34	+32	+6.3	-1.4	+2.8	+1.6	.96	+1	.30
10		8-21	06 31 20 06 35 00	960	45	+6	+7.0	-4.8	-5.0	-1.1	.90	-8	.40

FLIGHT	PROFILE	DATE	TIME (PDT)	z_i (m)	ΔZ_{EIL} (m)	ΔO_3 (ppbv)	$\Delta \theta_i$ (K)	ΔQ (g kg ⁻¹)	$\Delta \theta_e$ (K)	Δ_2 (K)	$\Delta_m / \Delta \theta_e$	X	i_{50} (g kg ⁻¹)
10		8-21	09 16 55 09 20 00	1060	13	+11	+9.0	-6.5	-7.2	-1.7	.91	-14	.40
10		8-12	11 05 30 11 08 00	1010	35	+11	+9.4	-6.5	-6.8	-1.5	.95	-17	.32
10		8-12	11 20 30 11 23 00	935	5	+21	+5.0	-3.5	-3.7	-0.8	.89	-4	.32

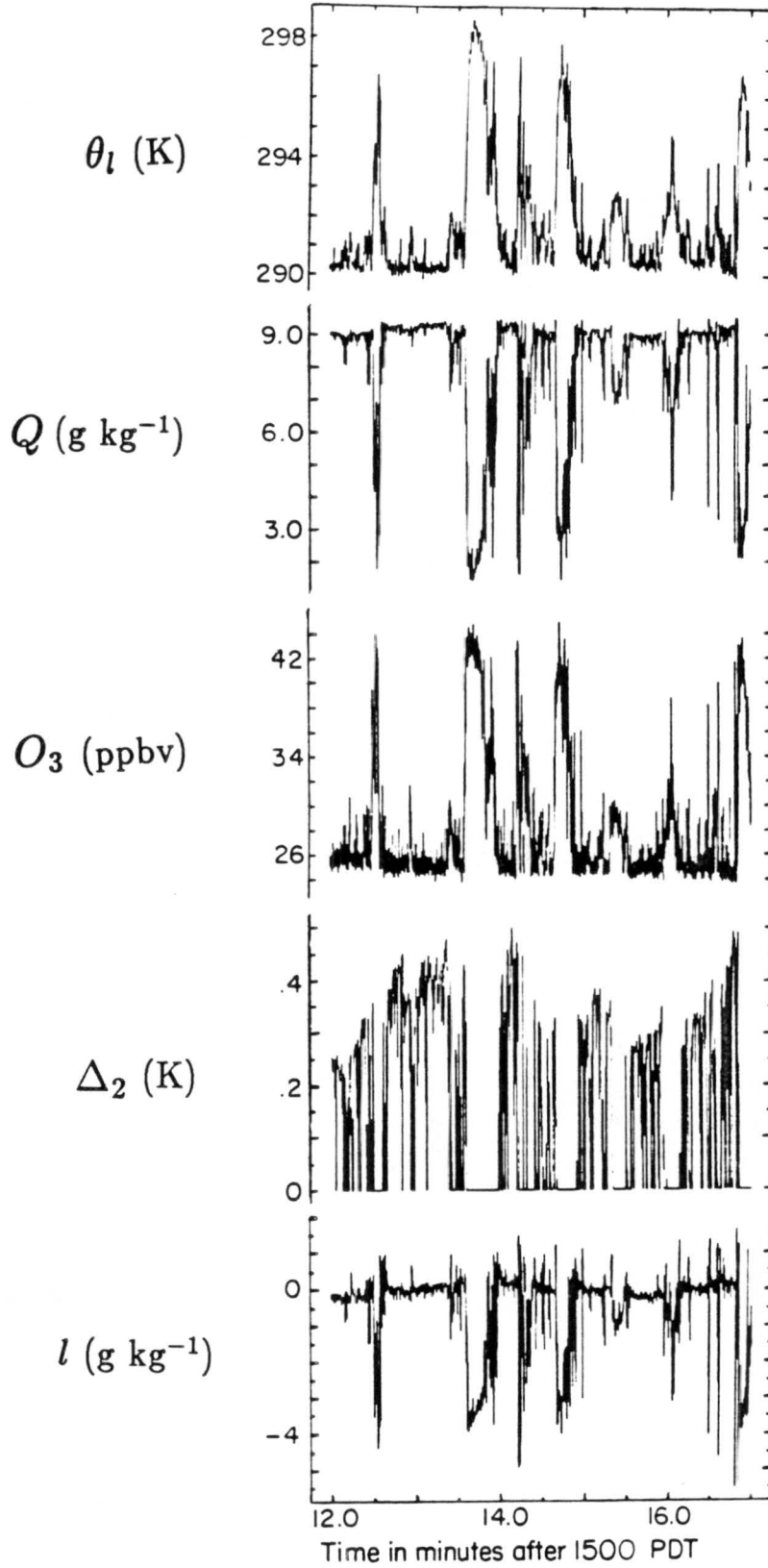


Figure 2.7. Time series of θ_l , Q , O_3 , Δ_2 and l from a horizontal leg at cloud top sampled 151200 to 151700 PDT 9 August 1985 during Flight 5.

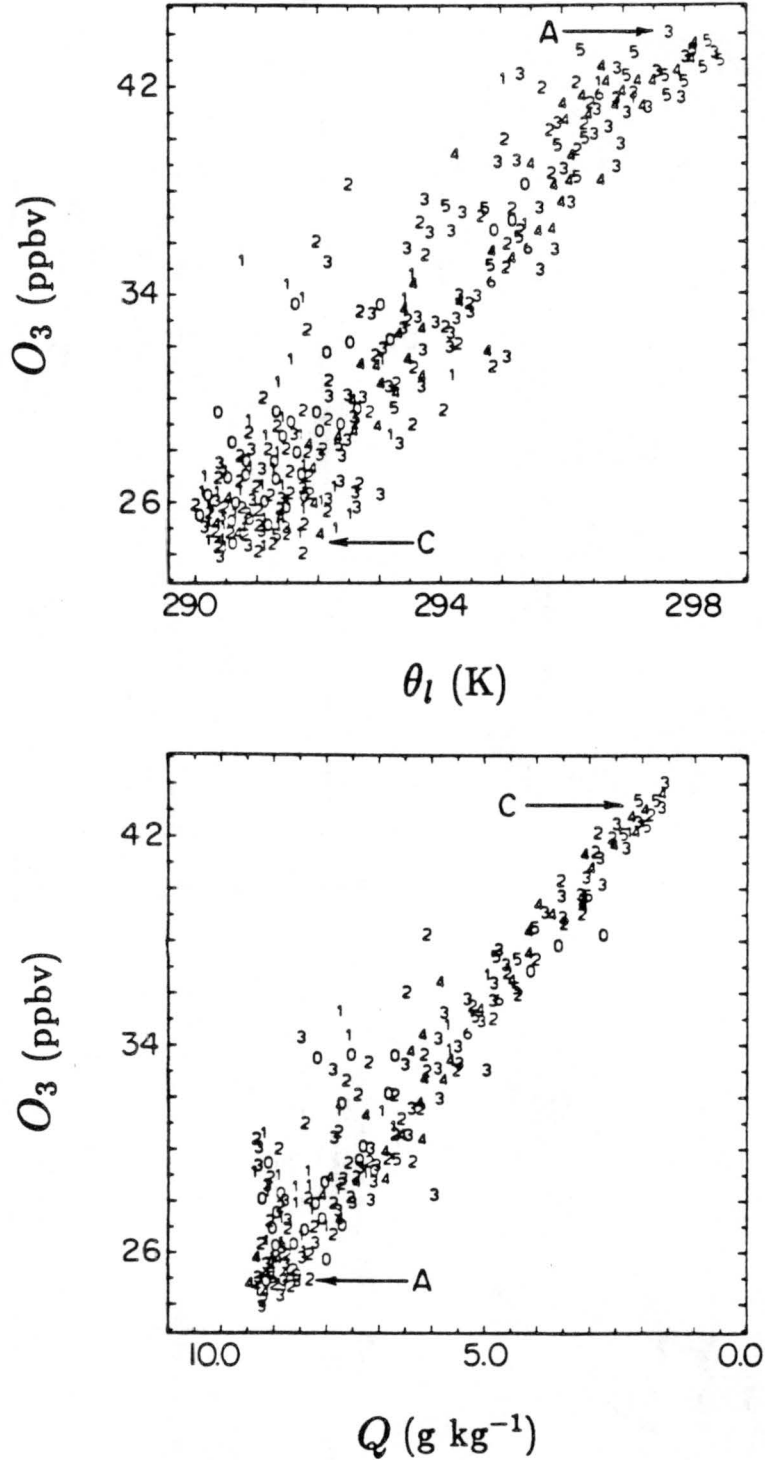


Figure 2.8. Mixing line analysis of (θ_l, O_3) and (Q, O_3) using data from the cloud top leg shown in Figure 2.7. See Figure 2.6 for an explanation of the labels.

Table 2.3. Important quantities obtained from all DYCOMS cloud top legs. Listed are jumps across the cloud-overlying air interface of O_3 , θ_l , Q , and θ_e . Stability parameters Δ_2 and X are also shown. The average liquid water mixing ratio when cloud is encountered during the leg is \bar{l} .

FLIGHT	LEG	DATE	TIME(PDT) START/STOP	ΔO_3 (ppbv)	$\Delta \theta_l$ (K)	ΔQ (g kg ⁻¹)	$\Delta \theta_e$ (K)	Δ_2 (K)	X (K)	\bar{l} (g kg ⁻¹)
1		7-30	13 33 10	+14	+9.3	-6.0	-5.6	-1.1	-19	.40
			13 38 00	+28	+7.3	-6.0	-7.6	-2.1	-18	
1		7-30	13 38 01	+15	+7.3	-5.5	-6.4	-1.6	-10	.40
			13 43 00	+25						
1		7-30	13 43 01	+22	+4.0	-2.4	-2.0	-0.3	-2	.40
			13 48 00	+32	+7.0	-4.9	-5.2	-1.2	-12	
1		7-30	15 56 00	+25	+2.7	-2.3	-3.0	-0.9	-1	.40
			15 59 58	+8.5	-8.0	-11.4	-3.4	-24		
1		7-30	16 00 11	+23	+7.9	-6.8	-9.0	-2.5	-19	.30
			16 05 00							
1		7-30	16 05 01	+5	+7.3	-6.3	-8.4	-2.4	-18	.35
			16 10 30							
2	L-1	8-02	11 55 30	+1	+5.0	-3.6	-4.0	-0.9	+1	.45
			11 58 30	+2.5	+6.8	-4.5	-4.4	-0.9	-10	
2	L-1	8-02	11 58 31	+2.5	+6.8	-4.5	-4.4	-0.9	-10	.45
			12 02 00	+11.5						
2	L-2	8-02	14 35 00	-1	+6.0	-4.2	-4.5	-1.0	-9	.40
			14 40 00							
2	L-2	8-02	14 40 01	+2	+6.8	-4.0	-3.2	-0.4	-10	.35
			14 45 00	+12						
2	L-2	8-02	14 45 01	+15	+4.7	-2.3	-1.0	+0.2	-2	.40
			14 49 00	+6.2	-4.0	-3.8	-0.7	-8		
3	L-1	8-04	12 26 00	+26	+2.8	-1.6	-1.2	-0.1	0	.40
			12 31 00	+39	+6.3	-3.8	-3.2	-0.5	-10	
3	L-1	8-04	12 31 01	+32	+8.5	-7.2	-9.4	-2.6	-22	.40
			12 36 00	+46	+7.0	-8.7	-14.7	-4.8	-25	
3	L-1	8-04	12 36 01	+7	+5.4	-3.9	-4.3	-1.0	-10	.35
			12 41 00							
3	L-2	8-04	15 15 00	0	+2.2	-1.8	-2.3	-0.6	-2	.16
			15 20 00							
3	L-2	8-04	15 20 01	+5	+2.3	-2.7	-4.4	-1.4	-2	.26
			15 25 00	+15	+5.3	-6.5	-10.9	-3.6	-16	
3	L-2	8-04	15 25 01	-3	-2.9	-2.8	-4.1	-1.2	-2	.28
			15 30 00	+5						

FLIGHT	LEG	DATE	TIME(PDT) START/STOP	ΔO_3 (ppbv)	$\Delta \theta_1$ (K)	ΔQ (g kg ⁻¹)	$\Delta \theta_2$ (K)	Δ_2 (K)	X (K)	\bar{I} (g kg ⁻¹)
4	L-1	8-07	12 45 00	+20	+4.7	-5.8	-9.7	-3.2	-10	.25
			12 50 00	+32	+7.2	-8.3	-13.5	-4.3	-20	
4	L-1	8-07	12 50 01	+32	+3.3	-1.8	-1.2	-0.1	0	.30
			12 55 00	+7.0	-7.3	-11.2	-3.5	-17		
4	L-1	8-07	12 55 01 13 00 30	+17	+7.0	-6.5	-9.2	-2.7	-12	.50
4	L-2	8-07	15 26 30	+28	+7.0	-6.5	-9.2	-2.7	-16	.40
			15 31 30							
4	L-2	8-07	15 31 31	+16	+4.5	-4.5	-6.7	-2.0	-4	.30
			15 36 00	+40	+7.5	-9.0	-14.9	-4.9	-21	
4	L-2	8-07	15 36 01	+11	+2.5	-2.5	-3.7	-1.1	+5	.30
			15 40 20	+41	+7.0	-8.0	-12.9	-4.1	-24	
5		8-09	12 29 30	+3	+1.5	-1.5	-2.2	-0.7	+4	.25
			12 34 00	+9	+4.0	-5.0	-8.5	-2.8	-5	
5		8-09	12 34 01	+8	+3.0	-3.0	-4.5	-1.4	0	.40
			12 39 00	+18	+7.0	-8.0	-12.9	-4.1	-18	
5		8-09	12 39 01	+12	+3.5	-3.0	-4.0	-1.1	0	.45
			12 44 30	+24	+5.5	-6.0	-9.4	-3.0	-14	
5	L-1	8-09	15 12 00	+3	+2.3	-2.0	-2.7	-0.8	+4	.40
			15 17 00	+18	+8.3	-8.5	-12.9	-4.0	-21	
5	L-1	8-09	15 17 01	+3	+1.9	-1.8	-2.6	-0.8	+7	.30
			15 22 00	+17	+5.7	-7.0	-11.7	-3.8	-14	
5	L-1	8-09	15 22 01	+4	+1.8	-2.0	-3.2	-1.0	+6	.40
			15 27 00	+23	+8.1	-8.9	-14.1	-4.5	-22	
7		8-16	11 19 00 11 23 00	+20	+10.3	-4.8	-1.75	+0.6	-8	.45
7		8-16	11 33 30 11 36 30	+18	+9.5	-5.1	-3.2	-0.1	-7	.70
9		8-19	13 45 00 13 49 00	+39	+4.4	-3.1	-3.3	-0.8	+5	.45
10		8-21	08 06 50 08 10 00	+12	+7.0	-3.4	-1.5	-0.3	-4	.50
10		8-21	08 10 00 08 13 10	+18	+7.0	-3.3	-1.2	+0.4	-2	.40
10		8-21	08 13 11 08 14 30	+20	+4.0	-1.4	+0.5	+0.7	+4	.50
10		8-21	08 14 31	+8	+5.2	-2.1	0.0	+0.6	0	.35
			08 19 00	+18	+5.5	-3.4	-2.7	-0.5	-2	
10		8-21	08 19 01	+10	+7.5	-3.8	-2.0	+0.1	-6	.40
			08 21 50	+3.8	-2.3	-0.5	+3			

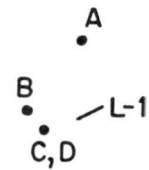
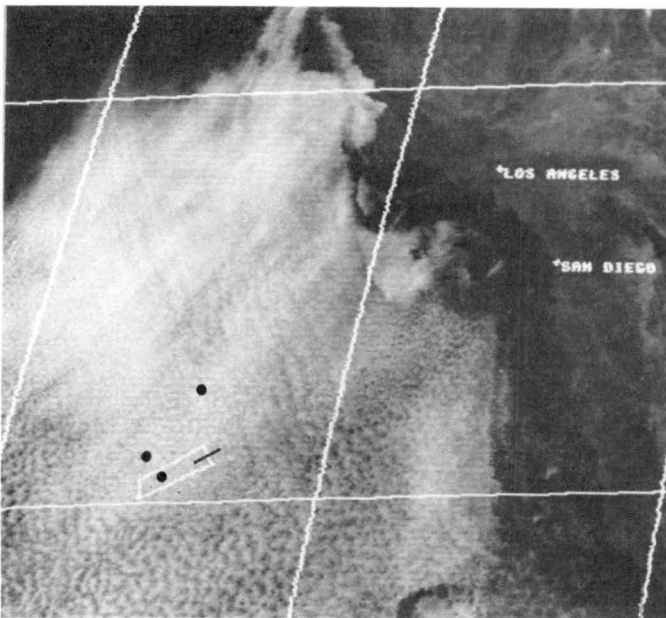
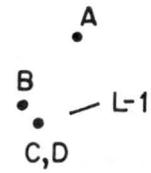
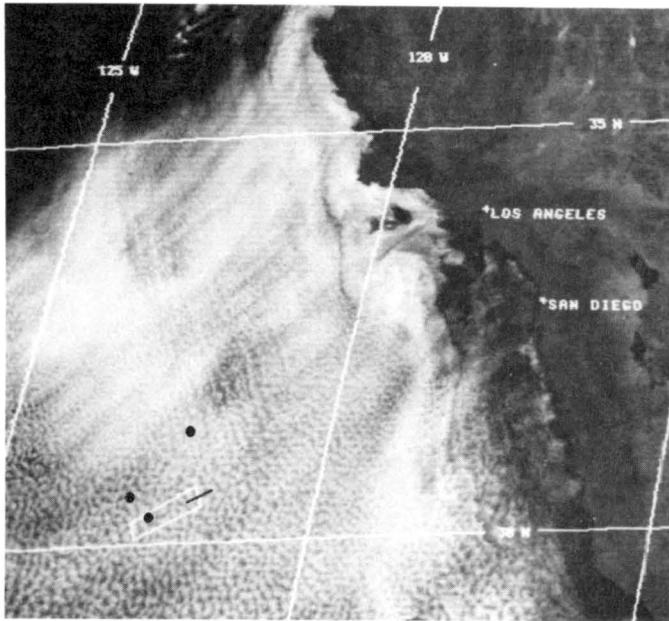


Figure 2.9. GOES-West visible satellite photographs from 110300 PDT 9 August 1985 (a) and 163300 PDT (b). Both figures show the four sounding locations (labeled: A 105600 PDT, B 134000 PDT, C 153000 PDT and D 154000 PDT) along with the location of the cloud top leg described in Figure 2.7.

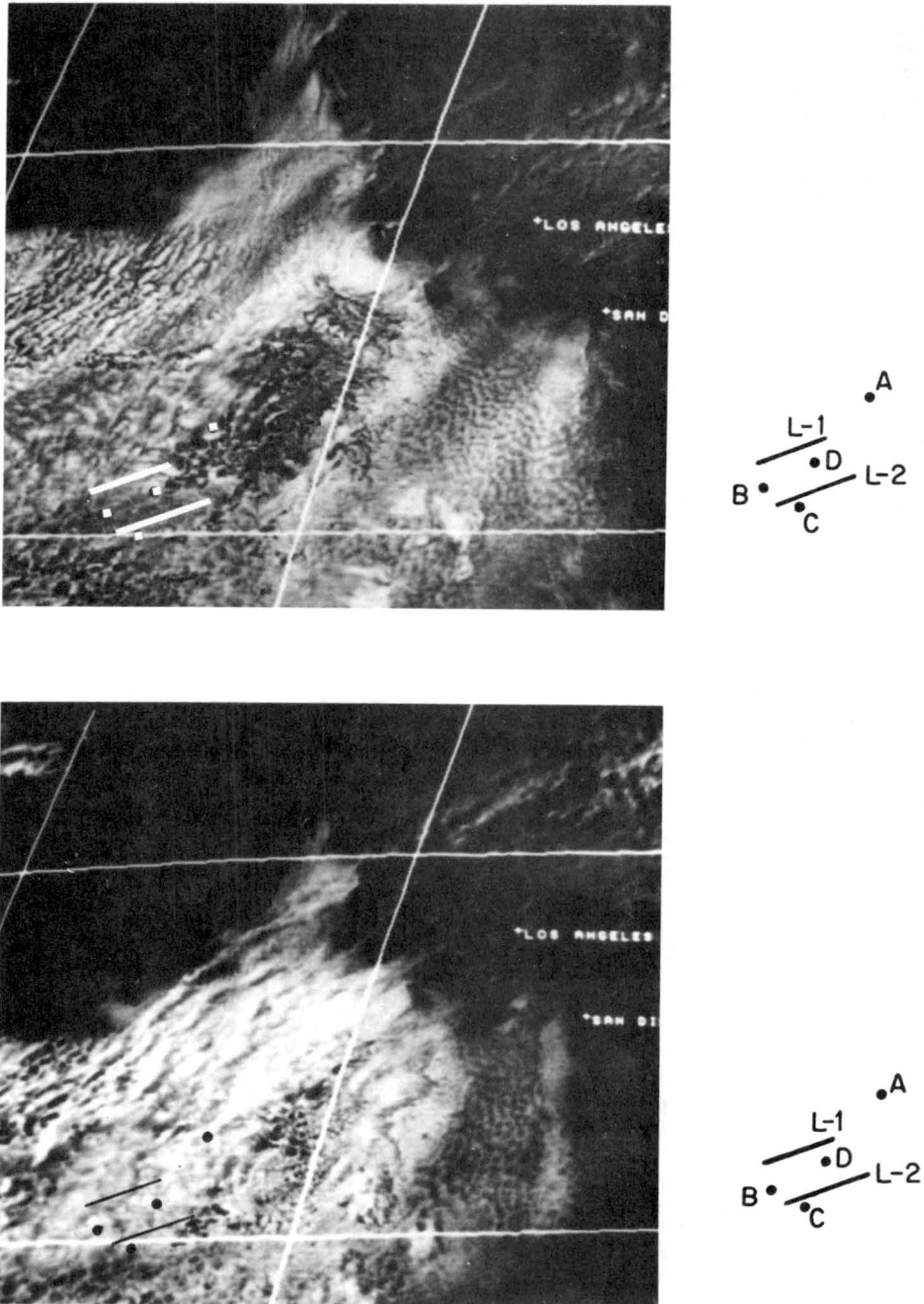


Figure 2.10. GOES-West visible satellite photographs from 130300 PDT 7 August 1985 (a) and 160300 PDT (b). Both figures show the four sounding locations (labeled: A 111000 PDT, B 135300 PDT, C 154100 PDT, and D 155500 PDT) along with the location of the two cloud top legs (labeled: 1 124500 to 130030 PDT and 2 152630 to 154020 PDT).

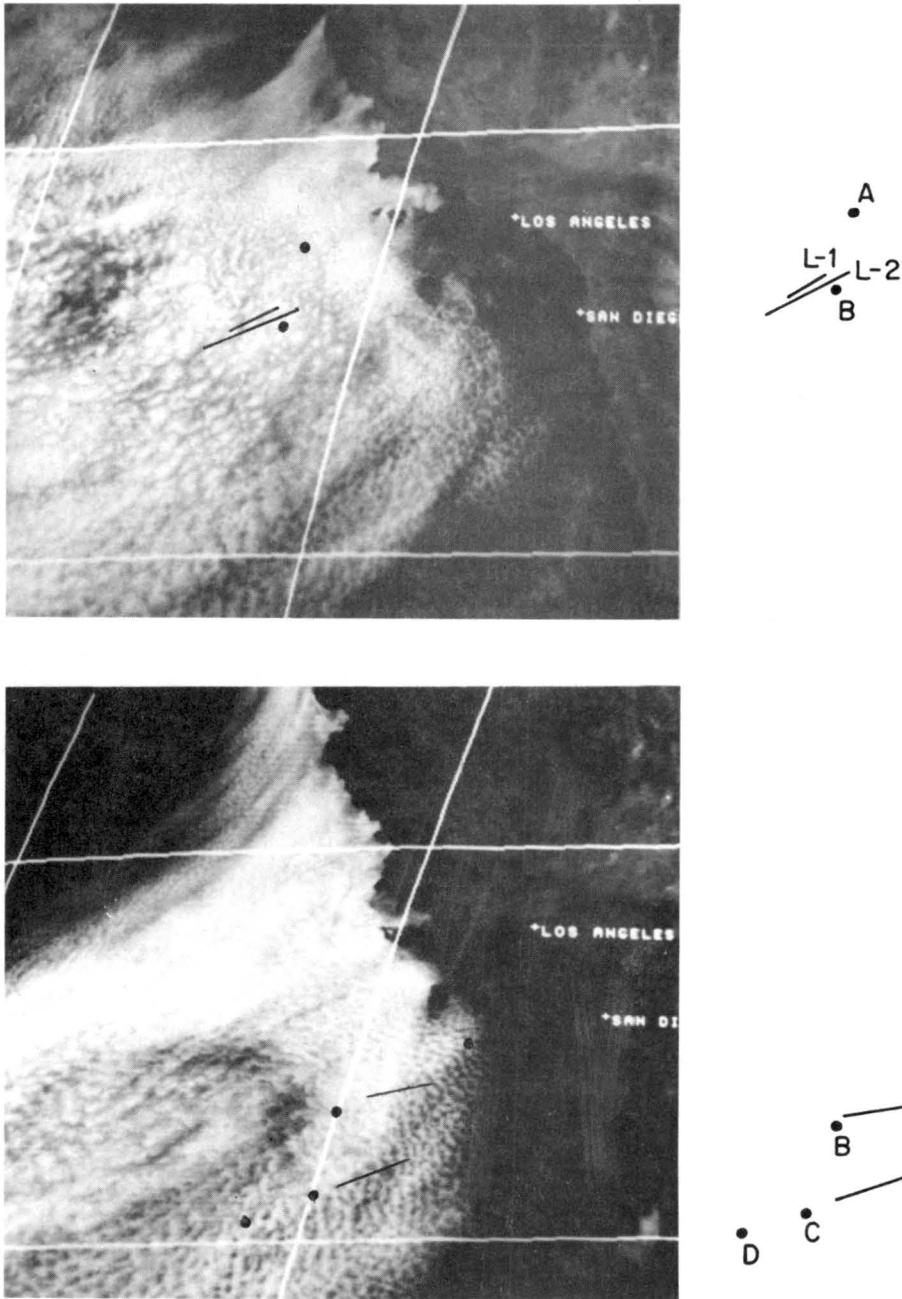


Figure 2.11. GOES-West visible satellite photographs from 150300 PDT 2 August 1985. The two sounding locations (labeled: A 102150 PDT and B 130030 PDT) are shown with the cloud top legs (labeled: 1 115530 to 120200 PDT and 2 143500 to 144900 PDT). (a)

GOES-West visible satellite photographs from 130300 PDT 4 August 1985. The four sounding locations (labeled: A 105220 PDT, B 133710 PDT, C 153350 PDT and D 154440 PDT) are shown along with the two cloud top legs (labeled: 1 122600 to 124100 PDT and 2 151500 to 153000 PDT). (b)

Chapter 4: VERTICAL MOTION

4.1 Background

It is clear that cloud top stability alone does not control the stratocumulus life cycle. Large scale vertical motion, another possible driving factor, may be important. Numerical experiments reported by Chen (1985) using a one dimensional second order closure model, which simulates the clouds off the California coast, support this. He shows that a doubling of the divergence rate from the climatological summer value, which in turn increases the subsidence rate, results in a decrease in the cloud liquid water content by some 30%. Use of climatological subsidence values causes enough cloud top warming to offset a significant part of the long wave radiative cooling. The cooling is still dominant and helps drive the positive heat flux observed in the model. When the subsidence rate is doubled the resulting warming offsets most of the long wave cooling and dissipates the cloud.

Roach et al. (1982) report the dispersal of a nocturnal stratocumulus cloud deck over the UK. They state that a 2-4 cm s⁻¹ subsidence rate could have been the break up mechanism but have difficulty demonstrating this from the observations. Ironically, for this case the cloud top stability criterion was never satisfied ($\Delta_2 > 0$)!

4.2 Observations

4.2.1 Description of Data

From the observational standpoint, the role of subsidence is difficult to assess since there are no direct measurements of divergence during the DYCOMS

experiment. This is because the change in the horizontal wind vector across the length of the research area is negligible and wind vector changes over larger distances in the eastern Pacific are sparse.

A different approach is to compare the vertical motion pattern typically associated with the observed synoptic disturbances to the satellite photographs on a daily basis. Furthermore, vertical motion fields from the Limited Area Fine Mesh (LFM) model of the National Meteorological Center (NMC) can be used in the analysis.

The approach for this study is to track the location and general intensity of the cyclones that frequent the eastern Pacific. The source used is the NMC weather charts. These are derived from ship data at the surface, aircraft observations at higher levels and previous analyses. A model is used to generate data where there are sparse observations which, unfortunately, covers a large area over the ocean. The 850 mb level is usually just above the inversion and therefore is the most appropriate analysis level to use when studying the vertical motion near the the EIL. The 6 hour forecast for the 700 mb surface was the best field available for the LFM derived motions.

The photographs shown are from the GOES West satellite and are in the visible spectrum. The infrared (IR) photographs (not shown) are sometimes used to infer the cloud top height.

The data considered for the remainder of this study are from the three summer months of 1986. The 1986 data are included because during DYCOMS the only example of cloud breakup is from a tropical cyclone on 12 to 13 August. Here we want to focus on breakup due to extra-tropical cyclones instead and there are three examples during 1986.

4.2.2 Case 1

Figure 2.12 shows four satellite photographs each taken at about 2000 GMT over a period of eight days in July 1986. Figure 2.13 shows a corresponding series

of 850 mb synoptic charts at 1200 GMT for the same days and Figure 2.14 shows the LFM derived vertical motion fields at 700 mb valid at 1800 GMT. On July 14 there is an area of stratocumulus clouds off the California coast extending to the south west; to the north of this band is a clear region. The 850 mb chart shows the typical high pressure system over the eastern Pacific and a low pressure synoptic system over western Canada. To the west of this synoptic cyclone is an area of cold air advection (CAA). This is shown by the height contours, indicating northerly flow, perpendicular to the isotherms off the Washington Oregon (WO) coast line. The derived motion field shows downward vertical motion greater than 1.6 cm s^{-1} over much of the CAA region which is also clear of stratocumulus. By July 16 the continued CAA has moved the 10°C and 15°C isotherms farther south along with the area of downward motion. Associated with this is the dispersal of the band of clouds lying off the California coast seen two days earlier. Two days later the cold pool of air off the WO coast has warmed but the 15°C isotherm has moved even farther south and the region off Baja California is cleared. However, the 700 mb level does not show downward motion. This is the farthest southern extent of both isotherms. By July 22 both isotherms have retreated north, the vertical motion field has smaller values over the eastern Pacific, and the clouds have returned.

4.2.3 Case 2

Figure 2.15 and 2.16 show a series of four photographs and 850 mb charts from a nine day period in August 1986. On August 13 a solid deck of stratocumulus lies off the California coast with thinner low level clouds off the WO coast. The synoptic map observed 20 hours before this has a low pressure system in western Canada which is associated with the northerly flow over the clouded region. Notice the location of the 10°C and 15°C isotherms in the eastern Pacific. On August 15 the WO coast has cleared and there has been simultaneous CAA behind the Canadian low pressure system. This system has also deepened some 90 m and

pushed the location of both isotherms south. The LFM derived vertical motions at 700 mb (not shown) are about -2 cm s^{-1} over the cloud free area off the WO coast at this time. By August 18 the California coast is clear. Although the WO coast is clouded, they appear to be middle to high level clouds judging from the IR satellite photo (not shown). This clearing is associated with the CAA and downward motion greater than 1.5 cm s^{-1} over the WO coast which lasted until 1200 GMT August 16. In addition, on August 18 the 10°C and 15°C isotherms have reached their most southern point. The clouds are back by August 21 because the CAA has stopped.

4.2.4 Case 3

Figure 2.17 and 2.18 show a series of photographs and 850 mb charts from an eight day period in June 1986. Figure 2.19 shows the LFM derived vertical motion fields at 700 mb valid at 1800 GMT. On June 13 solid stratocumulus lie off the California coast and the 15°C isotherm crosses the Canadian coast line. By June 16 the low pressure system that was further to the west has moved closer to the coast and there is a simultaneous break up of the once solid cloud deck making it more heterogeneous. Up to now the LFM shows that the region off the coast has experienced upward vertical motion of greater than 1.5 cm s^{-1} at 700 mb. This direction is reversed by June 18 as the system fills, continues to move east, and leads to CAA off the coast. Note the southerly movement of the 10°C isotherm. This CAA results in LFM downward vertical motions over the cloud-free area and maximum values of -4 cm s^{-1} . By June 20 the downward vertical motion is not as strong and the clouds show signs of returning; by June 23 (not shown) stratocumulus cover the entire region off the North American coast.

4.3 Discussion

One could argue that the association of CAA at 850 mb with cloud breakup tends to support entrainment instability theory. The weakening of the inversion

(the 850 mb level is usually above the inversion) means that Δ_2 and the θ_e jump across the EIL will become more negative resulting in greater instability and cloud dissipation. But this instability does not necessarily lead to a breakup of the cloud as shown in Chapter 3. Many clouds were observed and showed no sign of breakup despite the fact that the overlying air was unstable i.e. $\Delta_2 < 0$.

Breakup did not occur in these unstable cases because the entrainment of the overlying air was too slow, at least compared to the cloud building processes. An equation involving entrainment velocity at the cloud top illustrates how this might occur:

$$-w_e \Delta_2 = (\overline{w'\theta'_v})_{cloudtop}$$

Even if Δ_2 is very negative, a small w_e could still lead to a negligible buoyancy flux and stratocumulus persistence. The discontinuous mixing lines and the smaller σ_w at the EIL top, implies that the rate of entrainment was slow at times. Moreover, in the absence of significant vertical shear, it is physically unrealistic to expect the cloud to entrain the much warmer air above one of these discontinuities in temperature because this would require available potential energy at the expense of turbulent kinetic energy.

When entrainment does occur in the mixed layer it is probably limited to air in the EIL which is closest to the mixed layer's temperature and hence easiest to entrain. Here the degree of easiness is the amount of TKE used to bring the warmer air into the mixed layer. Entraining warmer EIL air means that more TKE must be expended and because TKE is limited the entrainment is controlled. Free entrainment, which does not require TKE, occurs when $\Delta_2 < 0$ and $\chi < \chi_{crit}$; otherwise, work must be done.

Several processes may change the jump in temperature across the cloud-EIL interface. Changes in temperature at the lower boundary of the mixed layer due to horizontal advection and above the EIL can both affect this jump—but not immediately. Time is needed to mix the temperature change down through the

EIL or up through the mixed layer. Advection of the mixed layer over a different sea surface temperature will affect the cloud-EIL interface after a time t_{ML} . This is the mixing time scale of the mixed layer equal to H/σ_w , where H is the mixed layer height and σ_w is the vertical velocity standard deviation of the mixed layer. Typical values for DYCOMS are 750m and 0.3ms^{-1} respectively, yielding a t_{ML} of about 40 minutes. Mixing warmer or colder air into the EIL from the top will also affect the temperature jump. But the mixing time scale for the EIL, t_{EIL} , is uncertain. One candidate is $\Delta Z_{EIL}/\sigma_w$ where ΔZ_{EIL} is the EIL thickness and σ_w is derived from the EIL. This estimate is probably too fast because unlike the mixed layer, there is a strong buoyancy gradient in the EIL which inhibits mixing. Instead, $\Delta Z_{EIL}/w_e$, the residence time scale in the EIL, may be a better estimate. Typical values for the thickness of the EIL and the entrainment velocity (Kawa, 1987) from the DYCOMS experiment are 20 m and 3 mm s^{-1} yielding a time scale of $7 \times 10^4\text{ s}$ (100 min). The similarity of these two mixing time scales means that the EIL and the mixed layer are basically in equilibrium with each other. However, because $t_{ML} < t_{EIL}$ there is the possibility that the EIL does not react quite as fast to changes in the mixed layer as the mixed layer reacts to changes in the EIL.

Once mixing effects a change in the temperature jump across the EIL-overlying air interface, it will modify the ease of entrainment. Advection of the mixed layer over warmer sea surface temperatures and the subsequent mixed layer warming would shift point A in Figure 2.6a to the right and allow the warmer air in the EIL to enter the mixed layer. The EIL probably adjusts rapidly to the new mixed layer temperature because no instances of curved EIL mixing lines toward the upper lefthand part of the (θ_l, O_3) diagram are observed. On the other hand a cooling of the mixed layer by the advection over colder sea surface temperatures would shift point A to left making entrainment even more difficult. It is conceivable that point A of Figure 2.6d used to be at A' and moved to the left as the mixed layer cooled. One explanation for the existence of the curved mixing lines on the (θ_l, O_3)

diagrams is that the mixing rate in the EIL sometimes cannot adjust fast enough to changes in air properties at the EIL boundaries. This tends to agree with the slight difference in mixing time scales of the EIL and mixed layer discussed above.

Radiative flux divergence at the cloud top is another process which can also ease entrainment. Its preferential cooling of air with a high water vapor content, such as found at the base of the EIL, means that there may be free entrainment if the cooling is strong enough.

The vertical motion associated with large scale dynamics could alter this conceptual model of entrainment. The following equation shows that decreasing w (to more negative values) will either decrease the boundary layer height or increase the entrainment rate

$$w = \partial H / \partial t - w_e.$$

It is generally thought that increased subsidence will lower the boundary layer height. This could push the cloud, below the lifting condensation level and evaporate the cloud. However, there is instead the possibility that H will remain constant and the entrainment rate will accelerate so that the overlying air will be entrained regardless of its buoyancy. The fact that this air is always dry would cause evaporation of the liquid water and dissipation of the cloud. Upward vertical motion may also play a role in altering the cloud structure as seen in Case 3. Here the lifting motion in front of the low pressure system raises the boundary layer top until the cloud is decoupled from the lower moisture source. When the clouds are cut off from their moisture source they take on a more heterogeneous cumulus appearance as seen in Figure 2.17b. Satellite photographs often show this structure after an 850 mb height fall due to an approaching low pressure system.

Vertical motion is not the only cause of breakup; there is at least one other. This was observed during DYCOMS when a tropical cyclone cleared the stratocumulus. But it appears that extra-tropical cyclones are often associated with

breakup. It is common knowledge among local forecasters that stratocumulus clouds will dissipate after the passage of a synoptic system (Peterson, 1987). It is ironic that there appears to be little if anything in the literature on vertical motion as a cause for dispersal.

Further research will be needed to investigate the physical mechanism for stratocumulus breakup. A network of radiosonde stations in the Pacific, perhaps on oil rigs or merchant ships could be organized for the determination of large scale divergence. Local measurements could be obtained from an aircraft measuring entrainment rates and changes of the boundary height with time. Aircraft measurements may yield information about boundary layer height, the entrainment rate and the thermodynamics of the cold pools of air behind the cyclones. However, it might be difficult to coordinate the flight plan with the location and time of cloud dispersal. Studies like this may show that there is no parameter based on thermodynamic jumps alone which can predict cloud breakup.

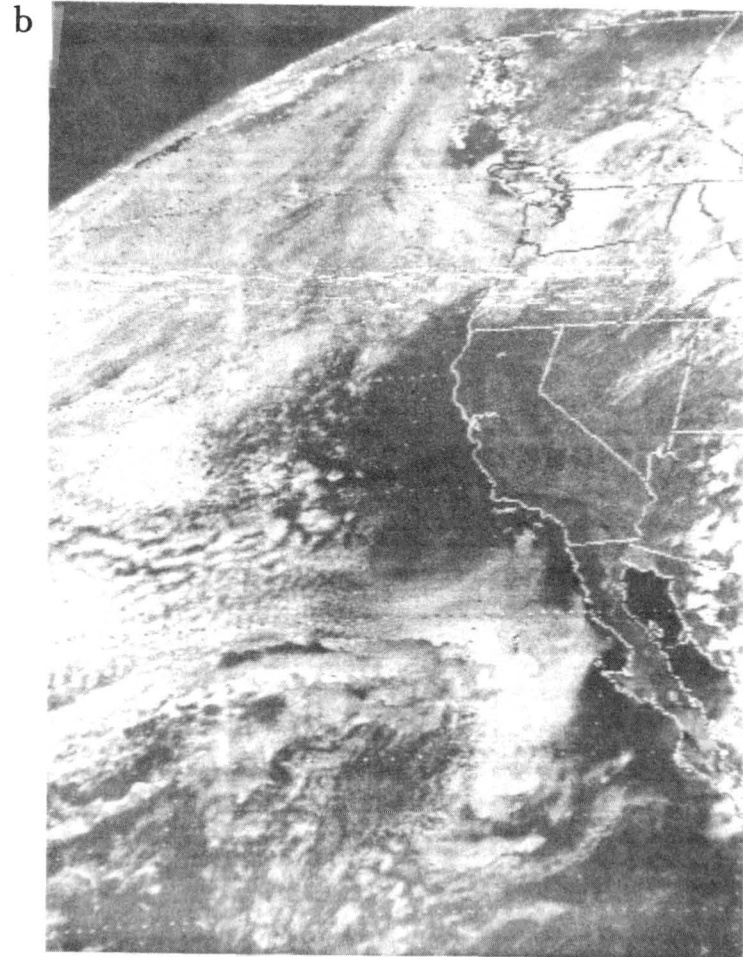
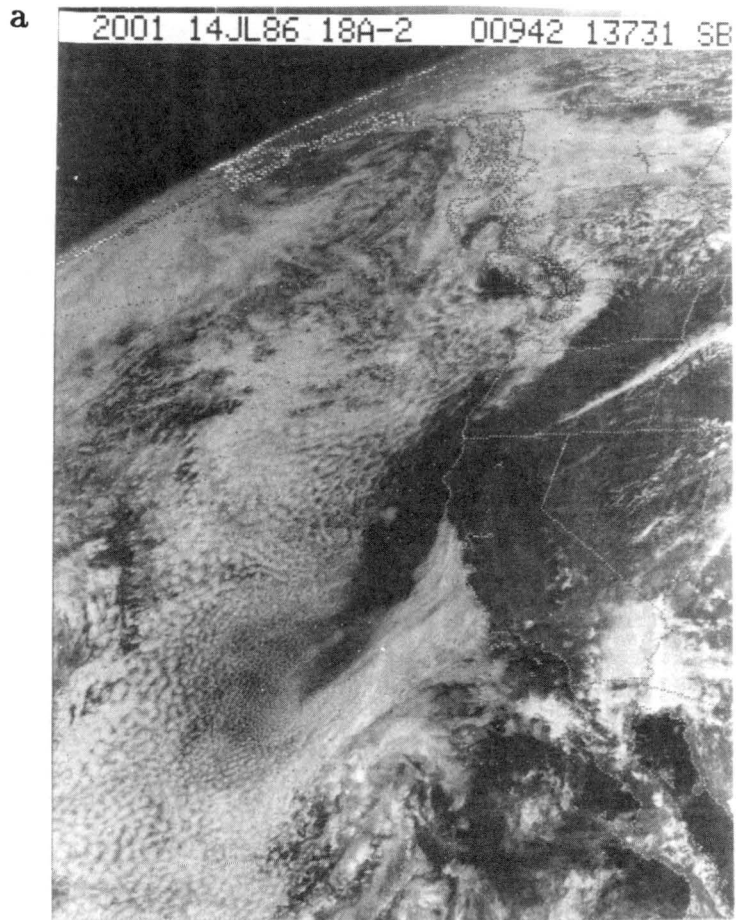
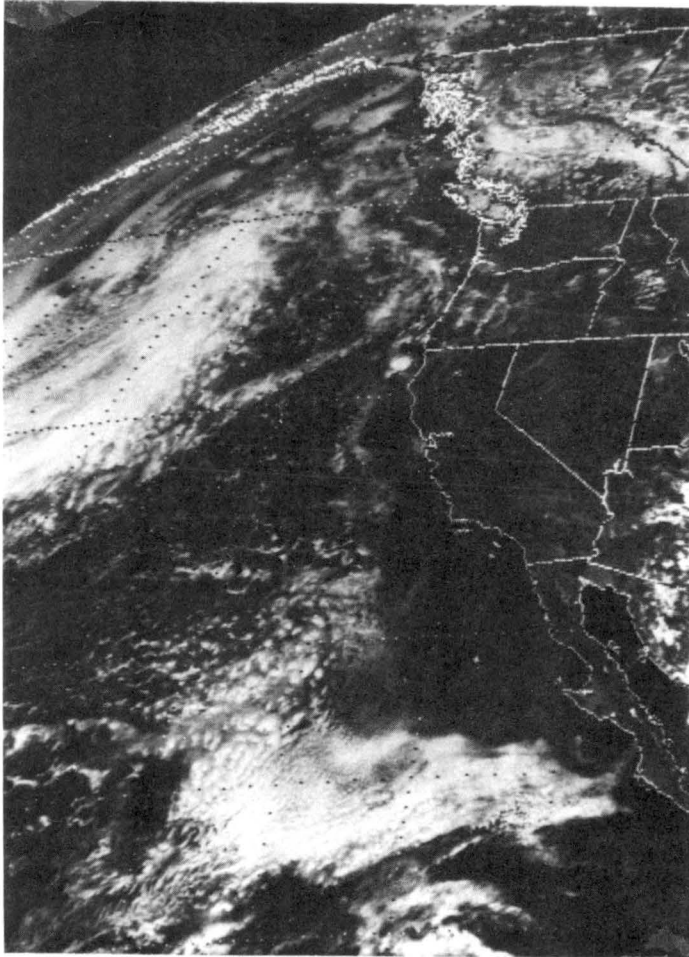


Figure 2.12. GOES-West visible satellite photographs from 14 July 1986 (a), 16 July (b), 18 July (c) and 22 July (d) all at approximately 2000 GMT.

c



d

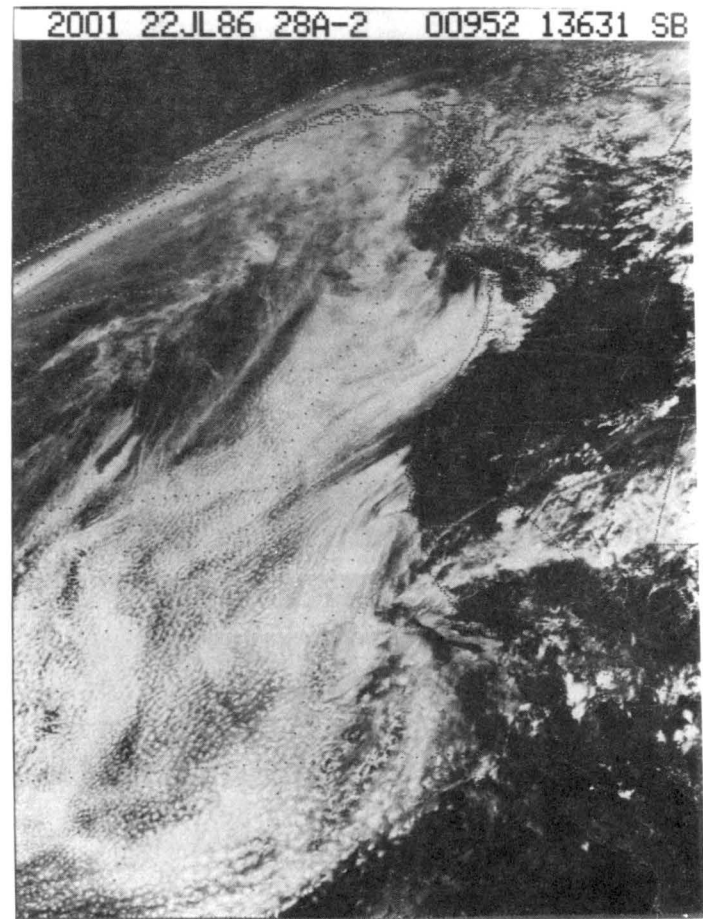
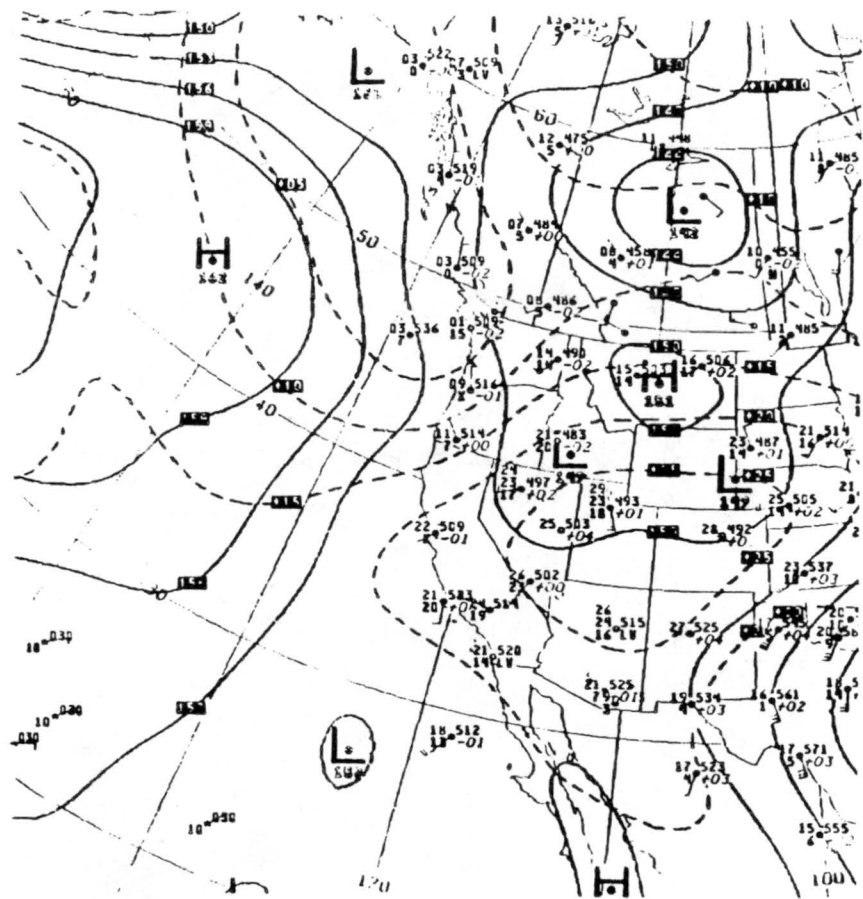
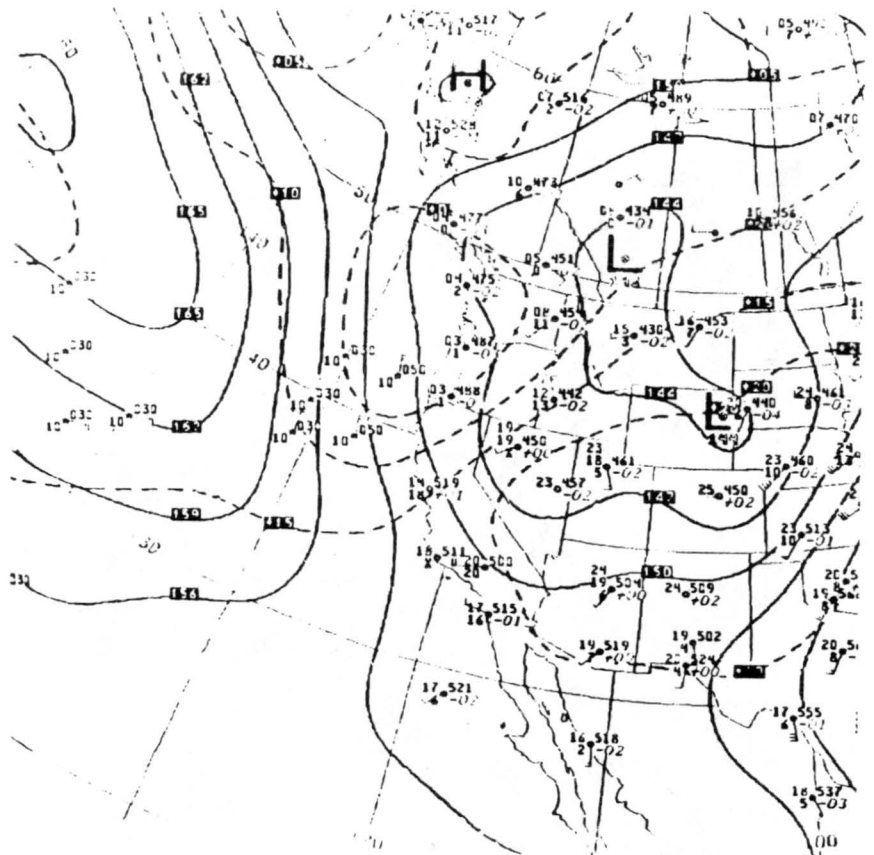


Figure 2.12. Continued



a



b

Figure 2.13. Synoptic analyses of 850 mb heights and temperatures from dates of Figure 2.12 at 1200 GMT.

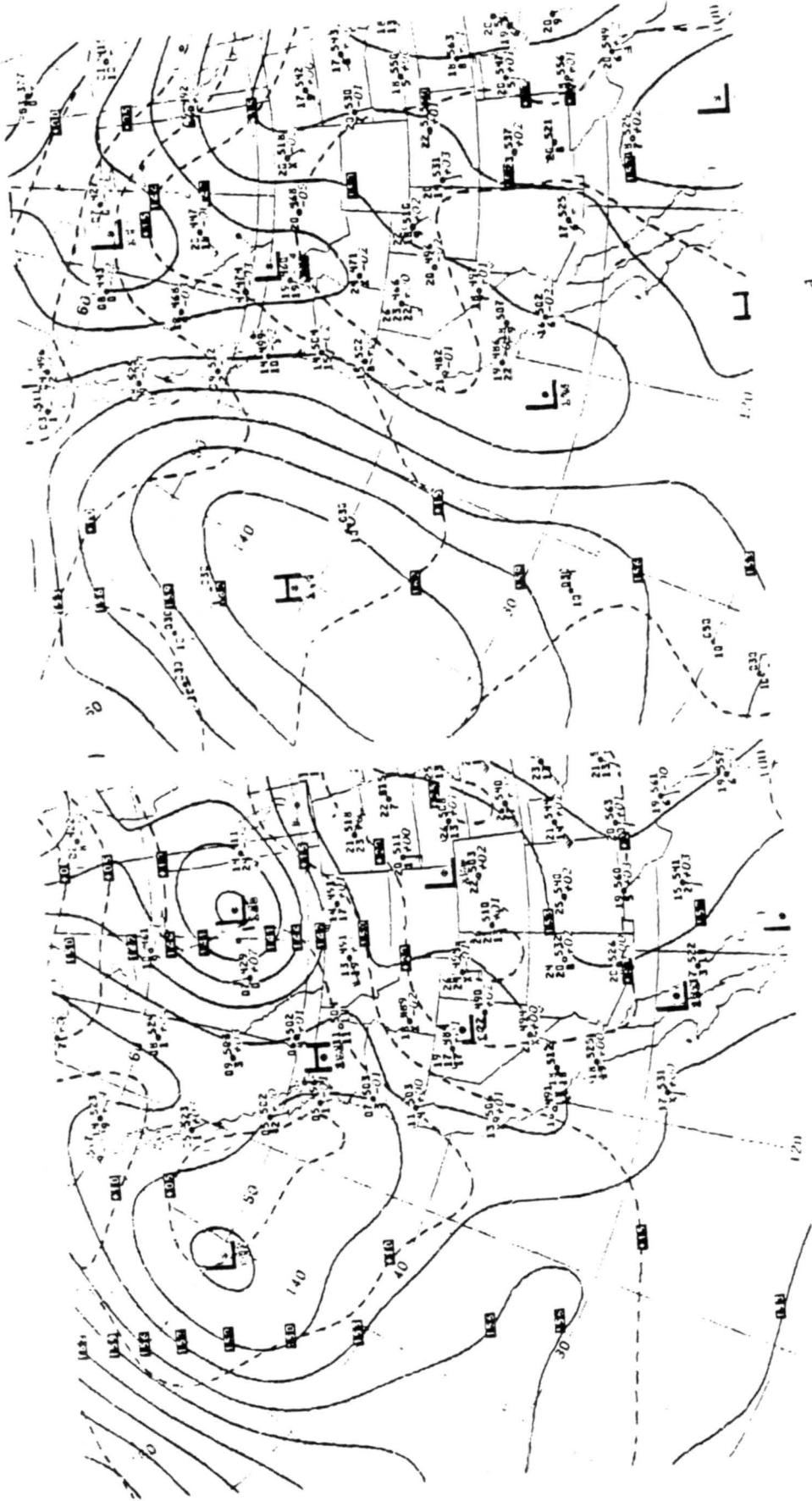


Figure 2.13. Continued

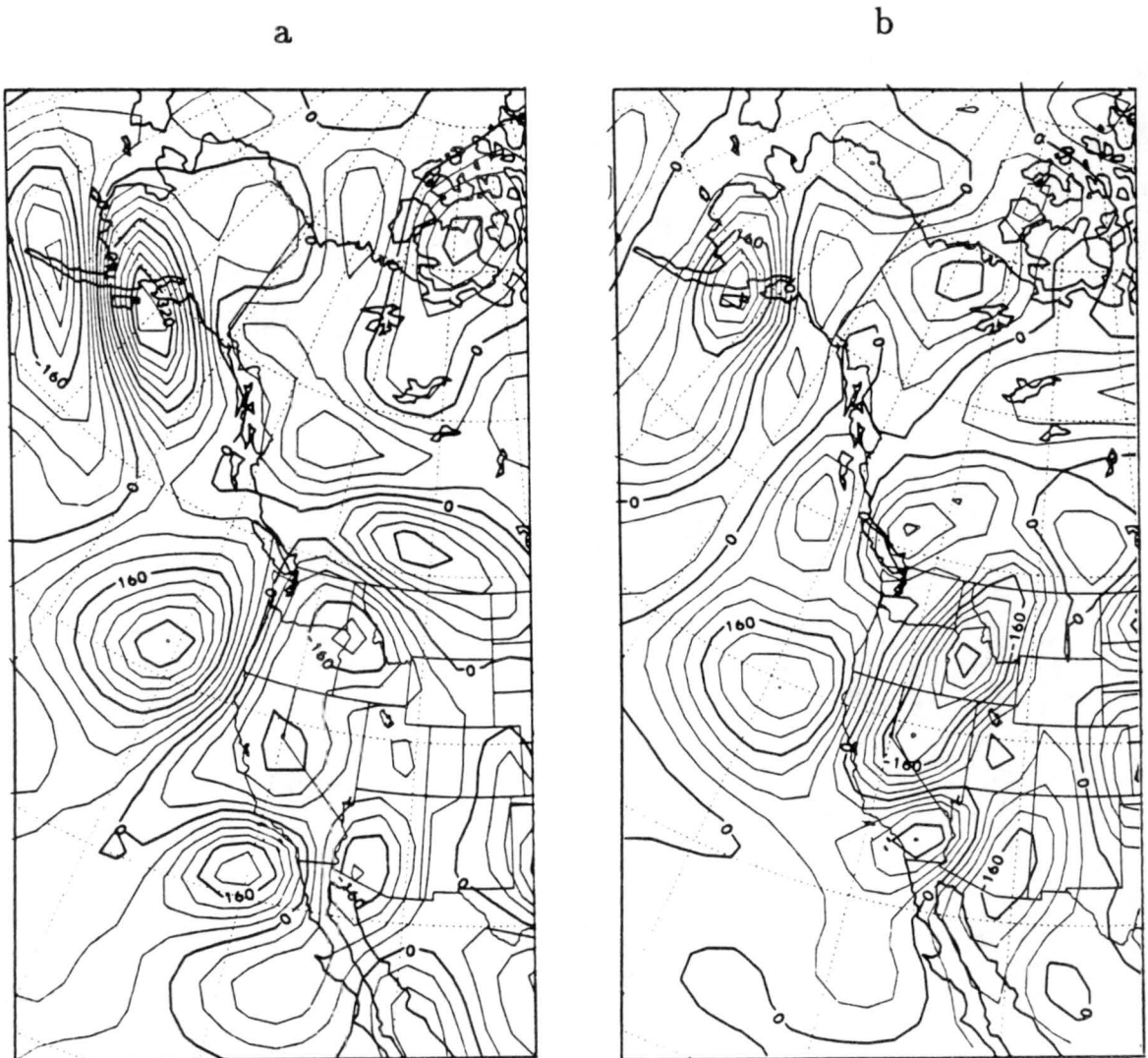
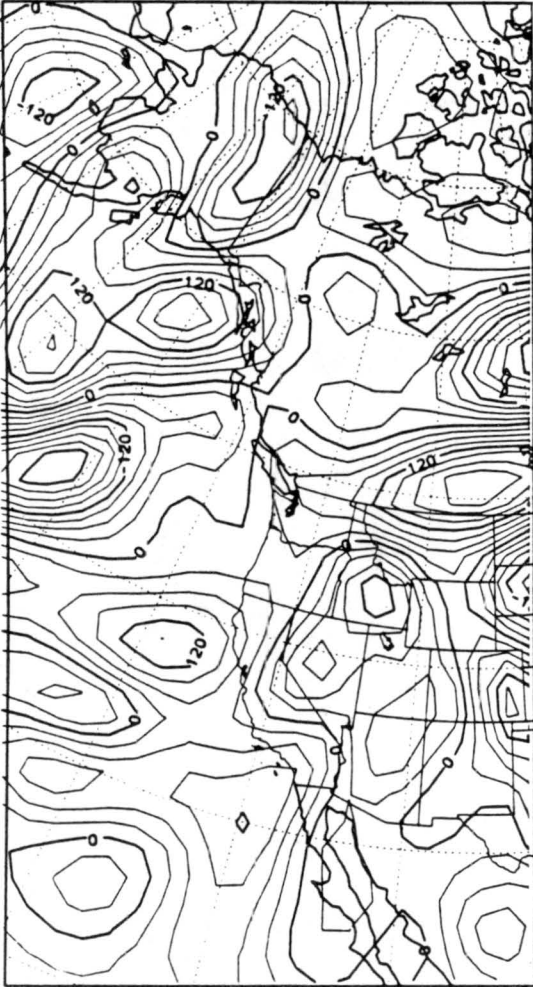


Figure 2.14. Vertical motion fields at 700 mb derived from the LFM model. Motions are from 6 hour forecasts and are valid at 1800 GMT on 14 July 1986 (a), 16 July (b), 18 July (c), and 22 July (d). The units are in mb s^{-1} and scaled by 10^5 . At this level $100 \times 10^{-5} \text{ mb s}^{-1}$ is approximately -1.0 cm s^{-1} .

c



d

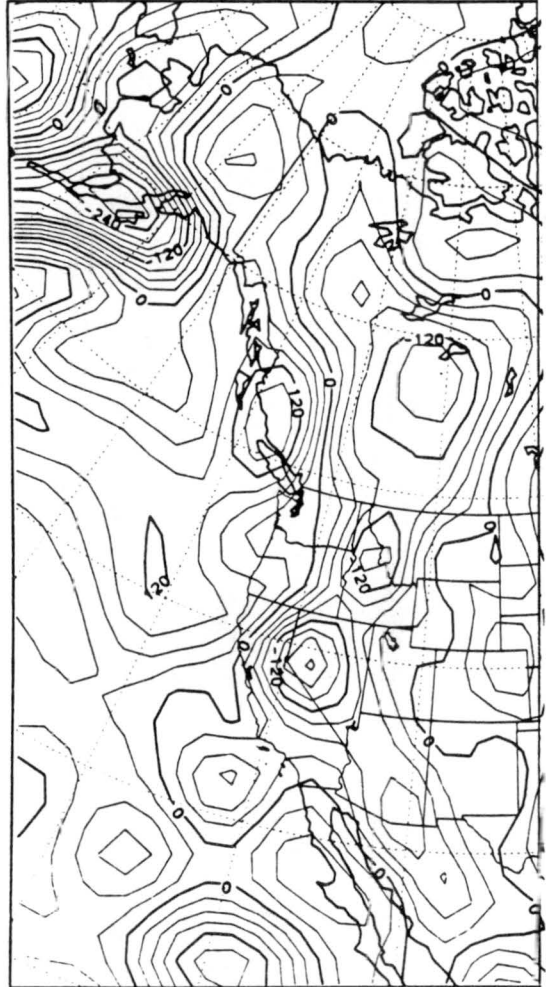


Figure 2.14. Continued.

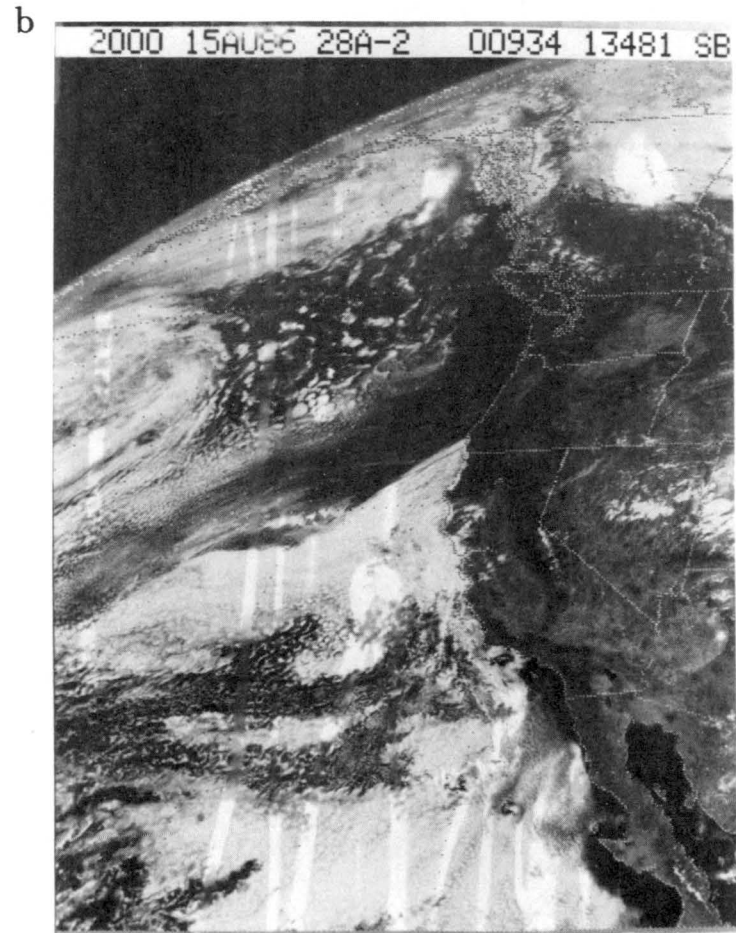
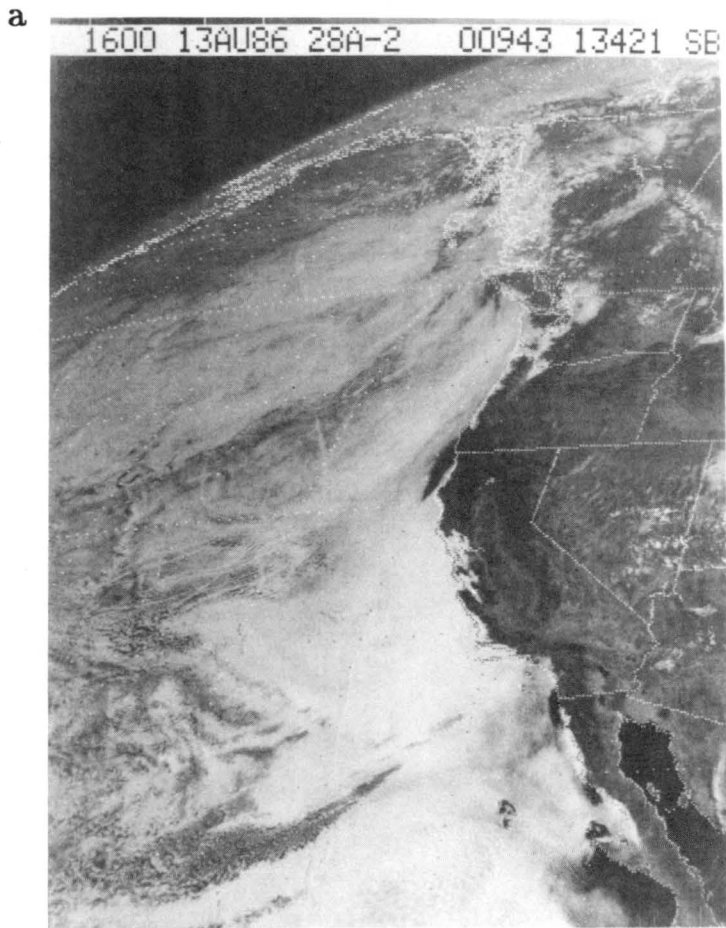


Figure 2.15. GOES-West visible satellite photographs from 13 August 1986 (a), 15 August (b), 18 August (c) and 21 August (d) all at approximately 2000 GMT.

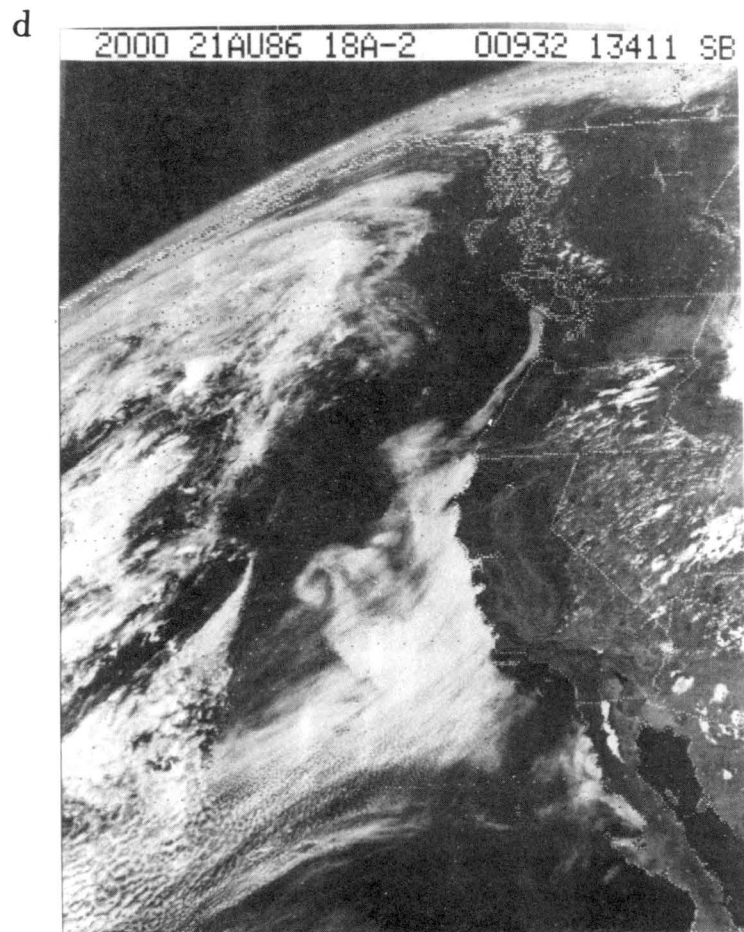
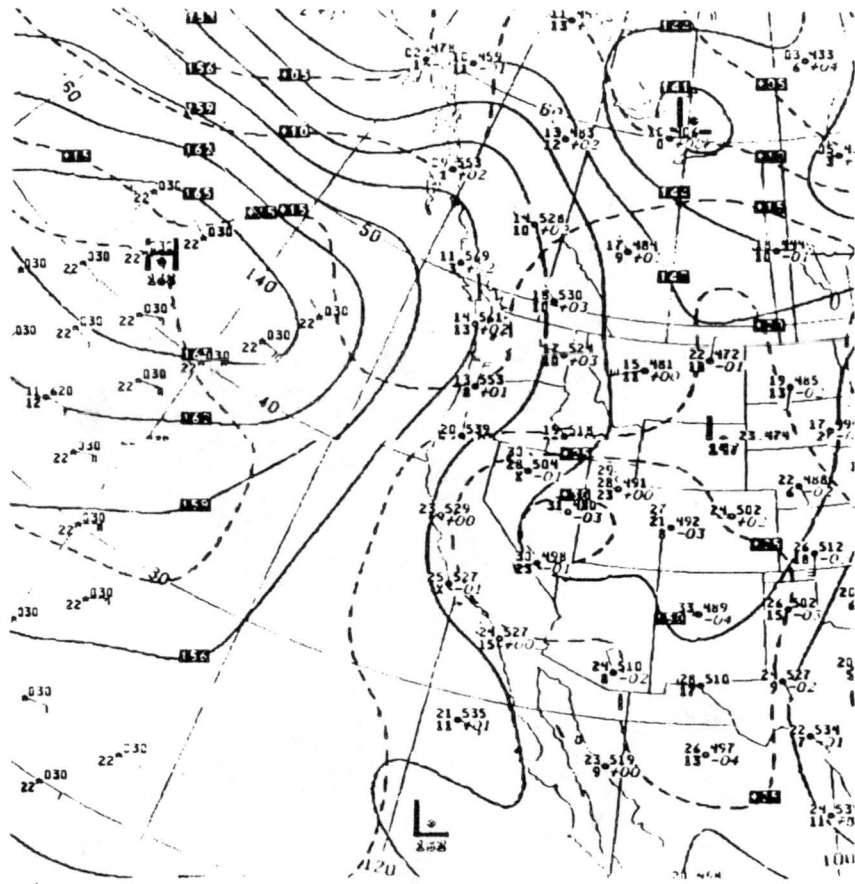
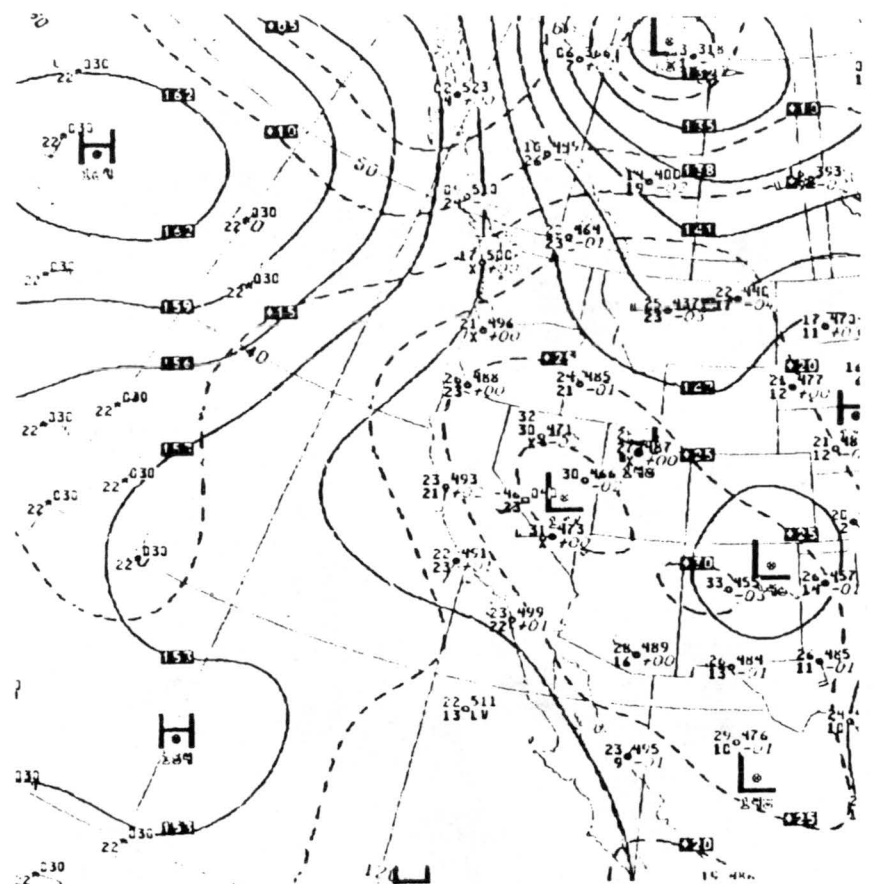


Figure 2.15. Continued



a



b

Figure 2.16. Synoptic analyses of 850 mb heights and temperatures at 0000 GMT for the dates of Figure 2.15.

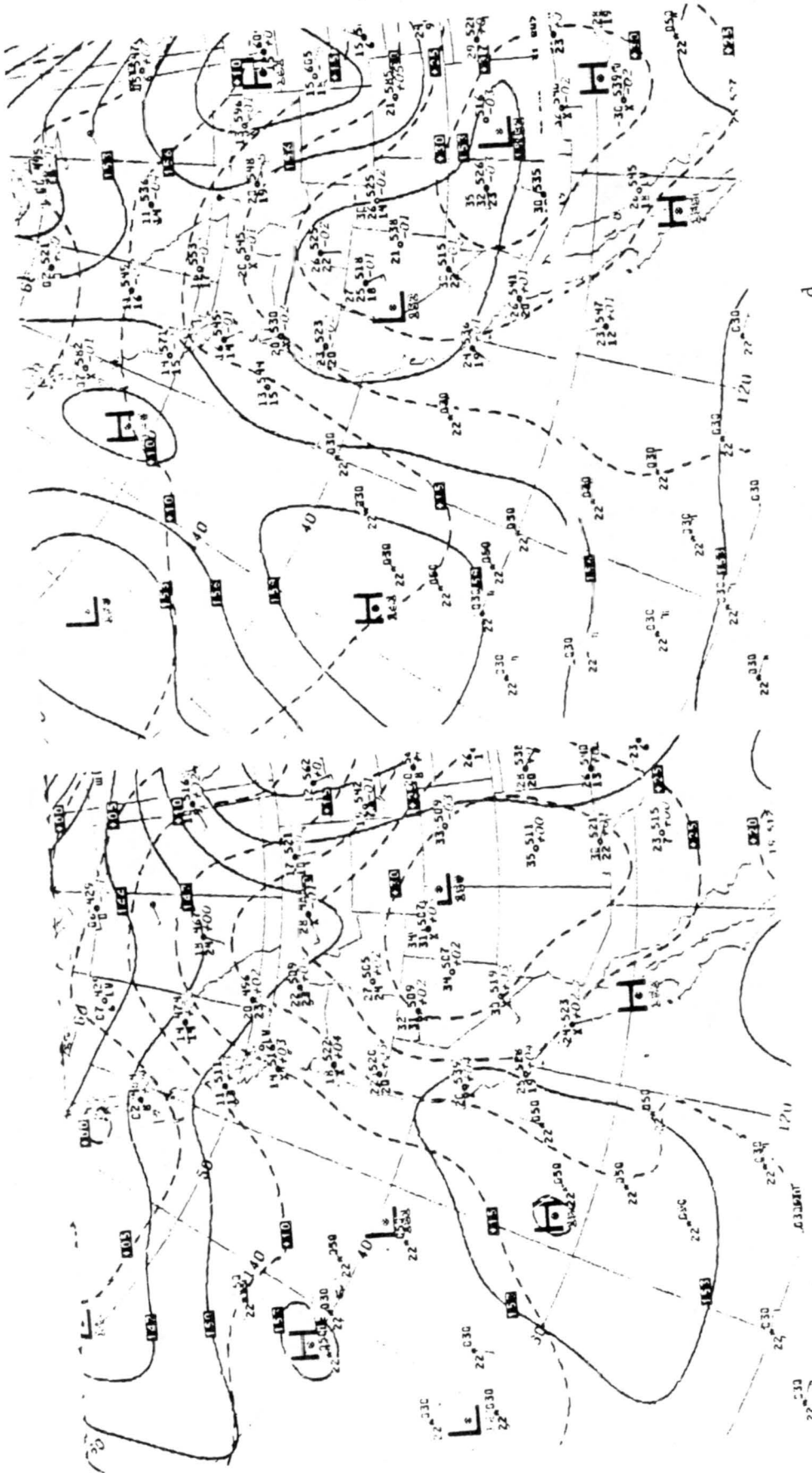


Figure 2.16. Continued

d

c

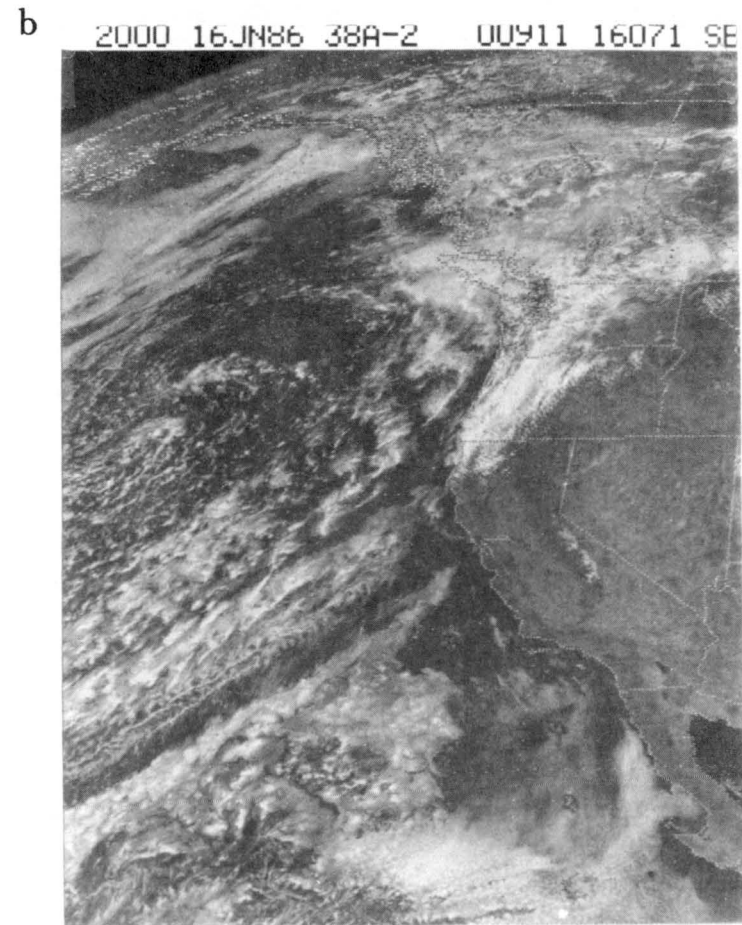
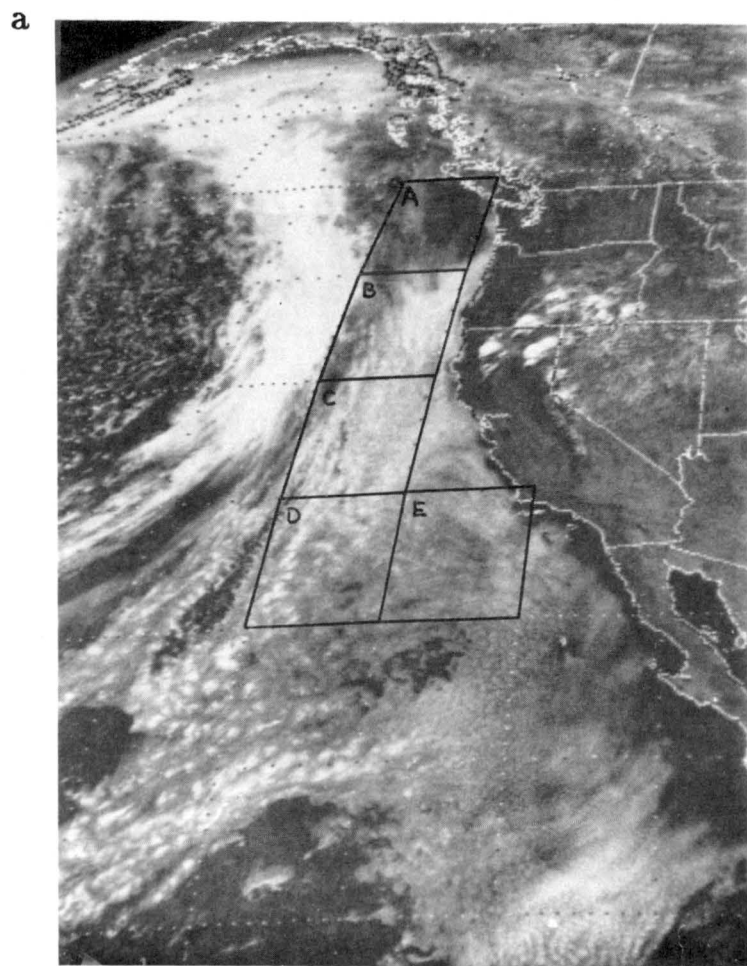


Figure 2.17. GOES-West visible satellite photographs from 13 June 1986 (a), 16 June (b), 18 June (c) and 20 June (d) all at approximately 2000 GMT.

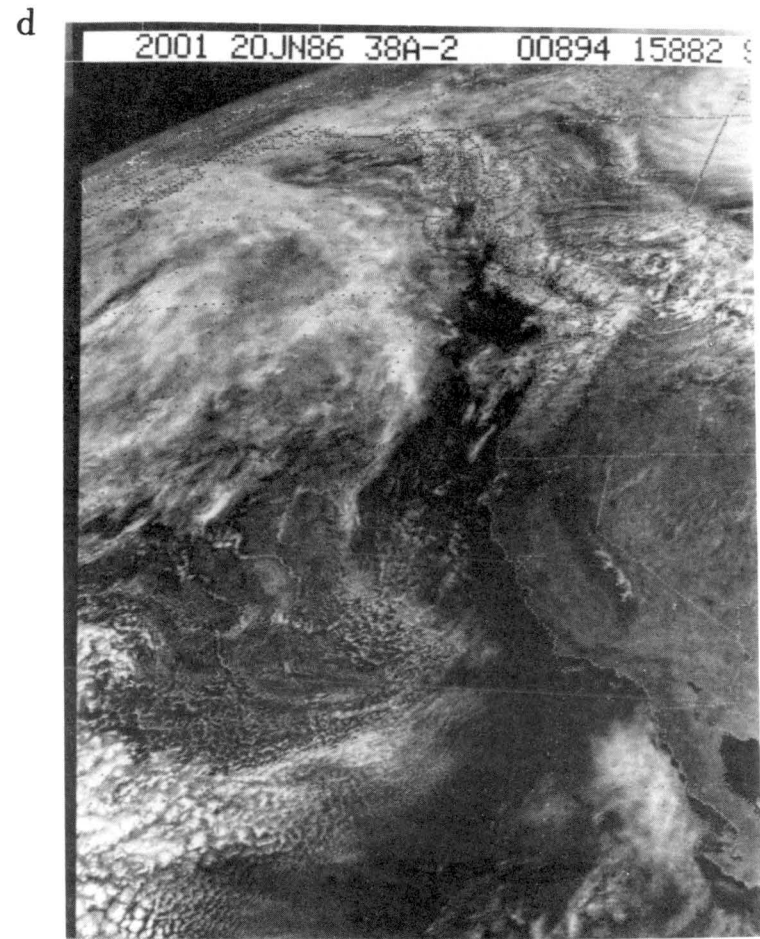
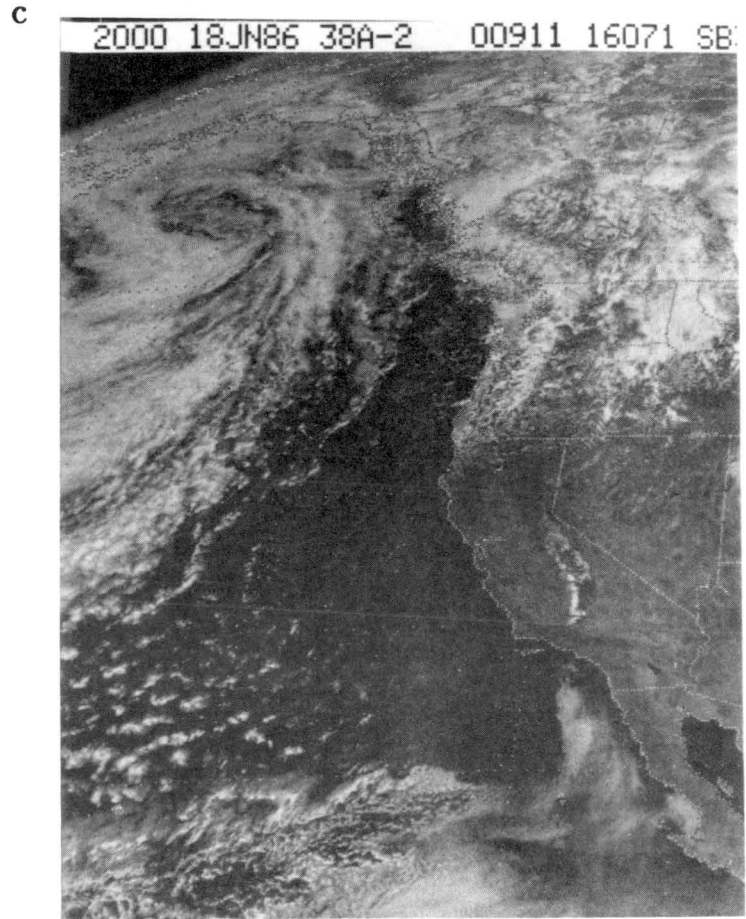
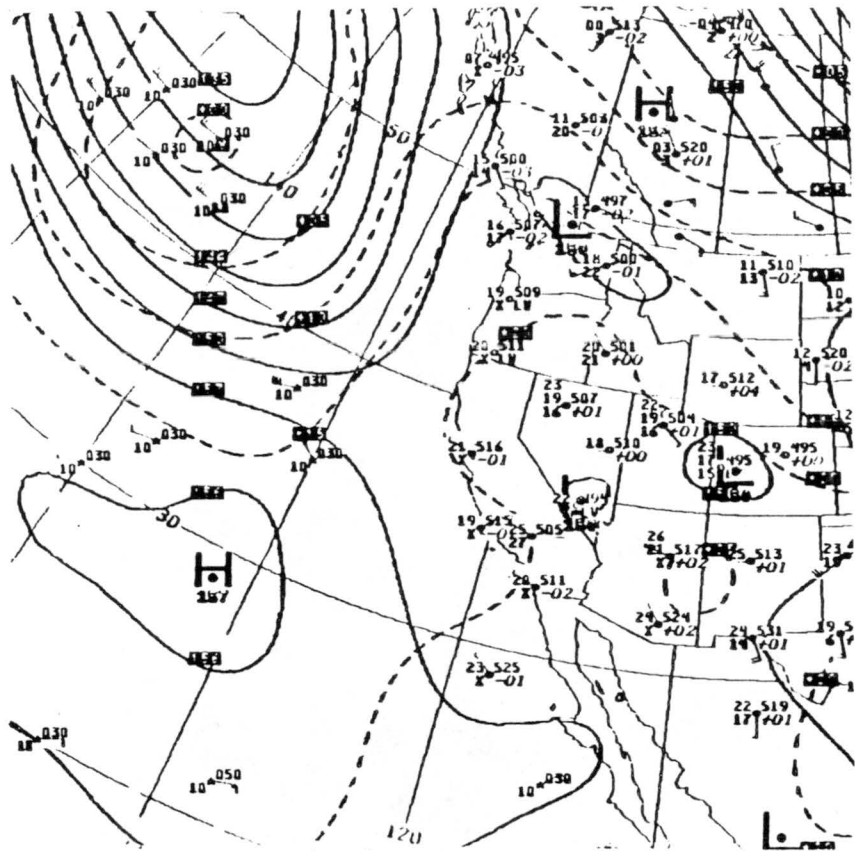
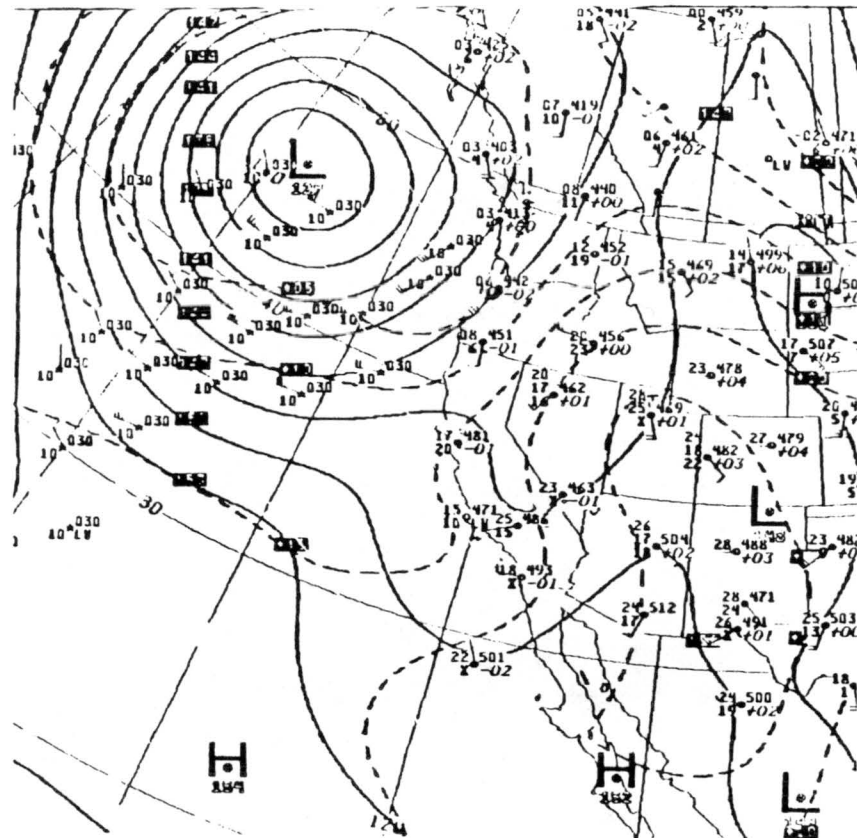


Figure 2.17. Continued



a



b

Figure 2.18. Synoptic analyses of 850 mb heights and temperatures from dates of Figure 2.17 at 1200 GMT.

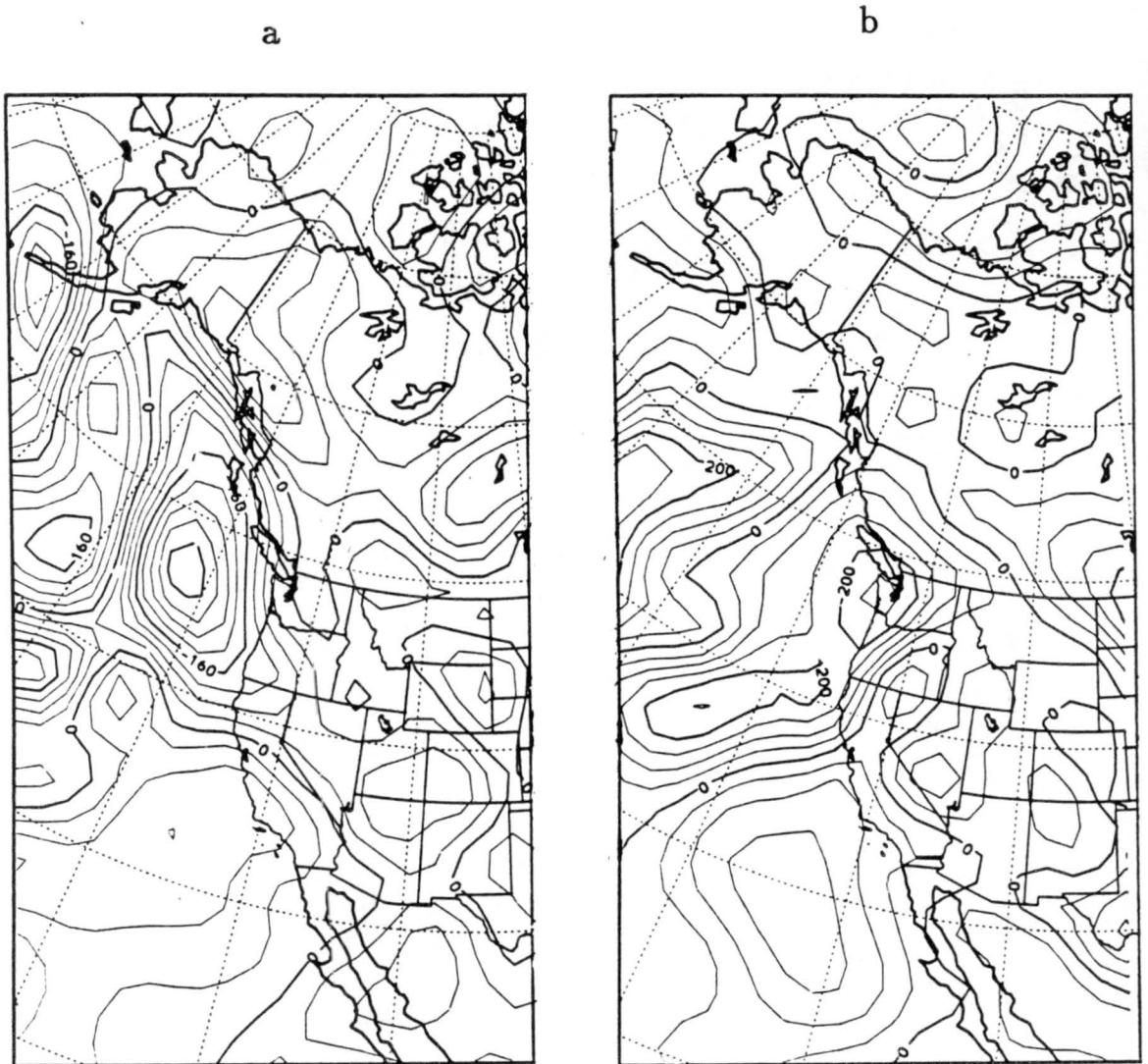


Figure 2.19. Vertical motion fields as described in Figure 2.14 for 13 June 1986 (a), 16 June (b), 18 June (c) and 20 June (d).

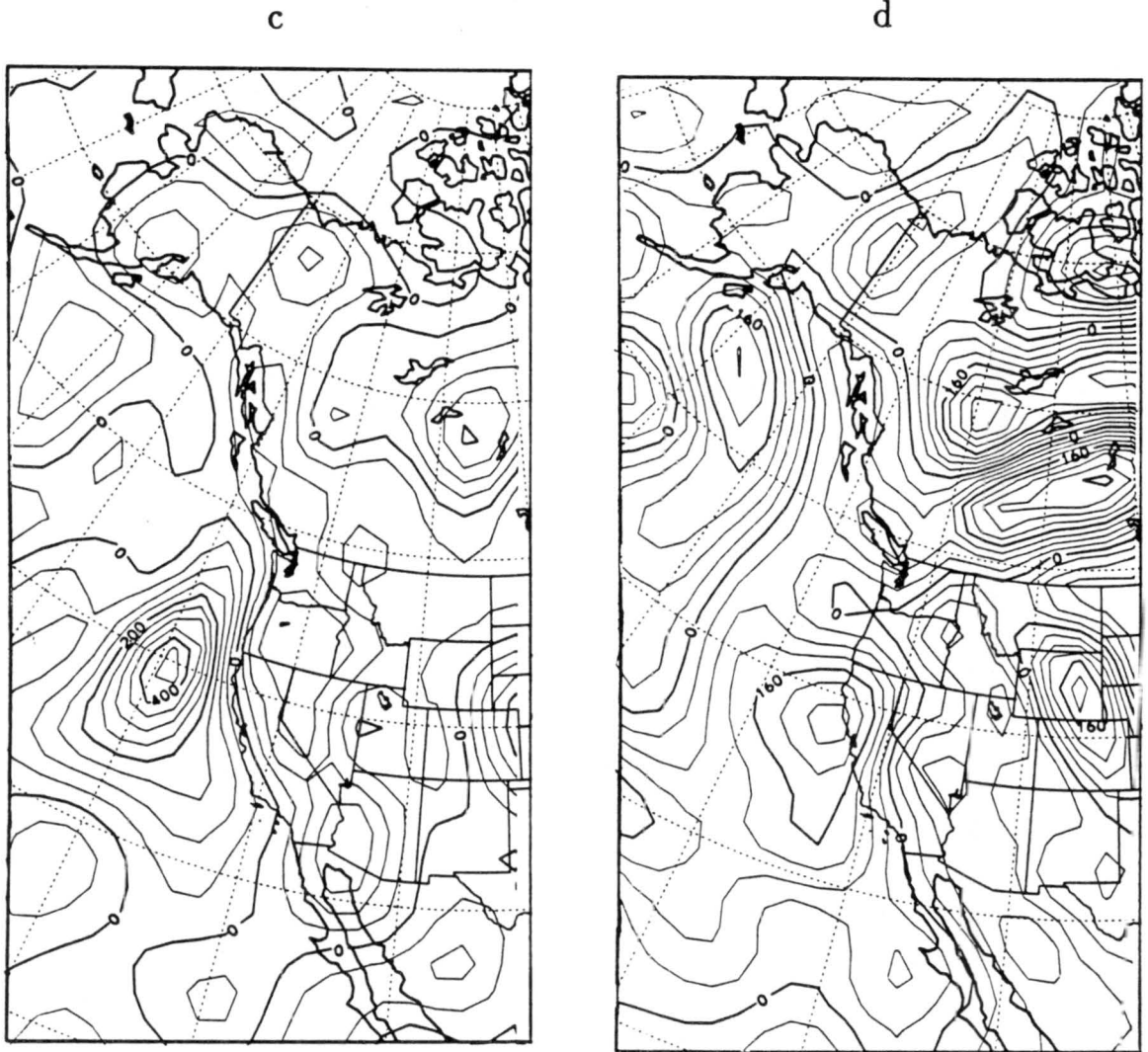


Figure 2.19. Continued.

REFERENCES

- Caughey, S. J., B. A. Crease and W. T. Roach, 1982: A field study of nocturnal stratocumulus II Turbulence structure and entrainment, *Quart. J. Roy. Meteor. Soc.*, *108*, 125-144.
- Chen, Chaing, 1985: The physics of the marine stratocumulus-capped mixed layer, research supported by Office of Naval Research, Contract #N00014-83-K-0032, Research Institute of Colorado.
- Deardorff, J. W., 1980: Cloud top entrainment instability, *J. Atmos. Sci.*, *37*, 131-147.
- Hanson, Howard P., 1984: Stratocumulus instability reconsidered: a search for physical mechanisms, *Tellus*, *36A*, 355-368.
- Kawa, S. R., 1986: Personal communication.
- Kuo, Hung-chi, 1987: Dynamical modeling of marine boundary layer convection. Ph.D. Dissertation, Atmospheric Science Paper No. 412, Colorado State University, Fort Collins, Colorado, 1987.
- Matthews, R. D., R. F. Sawyer, R. W. Shefer, 1977: Interference in chemiluminescent measurements of NO and NO₂ emissions from combustion systems, *Environ. Sci. Tech.*, *11*, 1092-1096.
- Nicholls, S. and J. D. Turton, 1986: An observational study of the structure of stratiform cloud sheets: Part II. Entrainment, *Quart. J. Roy. Meteor. Soc.*, *112*, 462-480.
- Pearson, R. Jr., 1987: Measuring ambient ozone with high sensitivity and bandwidth, submitted to *Rev. Sci. Instrum.*

- Pearson, R. Jr., and D. H. Stedman, 1980: Instrumentation for fast response ozone measurements from aircraft, *Atmos. Tech.*, 12, 51-55.
- Peterson, Craig, 1986: Personal communication, National Weather Service, Los Angeles California.
- Randall, D. A., 1980: Conditional instability of the first kind upside down, *J. Atmos. Sci.*, 37, 125-130.
- Randall, David A., 1984: Stratocumulus cloud deepening through entrainment, *Tellus*, 36A, 446-457.
- Roach, W. T., R. Brown, S. J. Caughey, B. A. Crease and A. Slingo, 1982: A field study of nocturnal stratocumulus: I. Mean structure and budgets, *Quart. J. Roy. Meteor. Soc.*, 108, 103-123.
- Shih, Chi-Fan: Personal communication, Dept. Atmospheric Science, Colorado State University.
- Stage, S. A., J. A. Businger, 1981: A Model for Entrainment into a Cloud- Topped Marine Boundary Layer. Part I: Model Description and Application to a Cold-Air Outbreak Episode, *J. Atmos. Sci.*, 38, 2213-2229.

APPENDIX INSTRUMENTATION

Temperature

There were two temperature probes for this project: the NCAR developed K-Probe and the Rosemount temperature probe. Both are platinum resistance instruments with a bandwidth of about 10 Hz. The K-Probe has slightly faster response but suffers from probe wetting resulting in a lower than correct temperature in cloud. Thus unless otherwise indicated the Rosemount probe will be used in this analysis.

Temperature measurements in cloud are suspect even when using the Rosemount. It is also susceptible to wetting though not as much as the K-Probe. Another method of in-cloud measurement is to use the temperature from the dew-point hygrometer. This assumes that the energy of the heater on the mirror of the hygrometer goes to evaporating any settled cloud droplets rather than heating up the mirror. This has some merit since in-cloud comparison with the Rosemount sensor shows a difference of less than 0.5°C.

Moisture

Two probes are used for moisture measurement in cloud-free conditions. The thermoelectric hygrometer (EG&G type 137) yields a the temperature of a mirror cooled just enough so that a thin film of dew always is present. While the absolute value of the derived moisture is normally accurate, the response is very slow (0.5 Hz bandwidth) and tens of seconds are required for the instrument to equilibrate with the environment once a large step in moisture is encountered such as at the top to the boundary layer.

The Lyman- α instrument developed at NCAR outputs a voltage related to the attenuation of electromagnetic radiation at a unique frequency by water vapor. The response is fast (10 Hz bandwidth); however, the voltage calibration is very tedious. The approach was to find a cloud-free location of high and low moisture (usually one in the boundary layer and one above) where the dew point hygrometer has adjusted to the environment and calibrate the output using a simple linear regression with q derived from the dew point hygrometer. This was done for each sounding and horizontal leg.

For vapor measurements in-cloud, saturation was assumed and the Rosemount temperature used to calculate a saturation mixing ratio.

Liquid Water

The absolute value for liquid water is from the King Probe from Particle Measuring Systems Inc. Values are accurate with a bandwidth of about 1 Hz although tedious baselining preprocessing is sometimes needed.

Crucial to the evaluation of moisture and hence to many thermodynamic quantities is the determination of in-cloud (saturated) conditions. The presence of liquid water as indicated by the integrated liquid water from the FSSP laser spectrometer (Particle Measuring Systems) for the cloud droplet range is used. The threshold value for saturated conditions is 0.01 gm^{-3} . Although, this instrument is not as accurate as the King Probe and hard to interpret, tedious baselining is not needed.

Ozone

The ozone analyzer employed in Part 2 of this thesis is a totally new instrument built by Pearson (1987) which achieves significantly higher bandwidth, higher sensitivity, and improved stability than the original Mark I unit described by Pearson and Stedman (1980) and used for the work described in Part 1 of this thesis. Two 330 L min^{-1} vacuum pumps draw sample air through a stainless

steel frit located in the airstream outside the aircraft. Sample air is mixed with 5 to 10% nitric oxide (99% CP grade) at a pressure of 8 to 10 mb and the resulting chemiluminescence is detected by a 51 mm dia. red-sensitive photomultiplier tube (PMT). Due to the relatively large signal levels measured, analog signal processing is used throughout the instrument.

The higher pumping capacity of the instrument compared to the Mark I unit enables it to achieve an unfiltered bandwidth of at least 20 Hz. As employed here, the O_3 signal was filtered to 10.0 Hz bandwidth with a 4th order Butterworth low pass filter identical to those employed with the fast-response air motion, temperature, and moisture sensors. Sensitivity to O_3 is better than 0.05 ppbv at 10 Hz bandwidth. Long term stability has been improved over the Mark I unit through better temperature control over the PMT and its high voltage supply. These improvements permit differences in O_3 of 0.1 ppbv to be measured reliably for mean mixing ratios in the 10 to 100 ppbv range. This capability is needed to measure the jumps in O_3 at the top of the mixed layer for the work described here.